

MICROWAVE AND MILLIMETERWAVE MINIATURIZATION TECHNIQUES AND
THEIR APPLICATIONS

A Dissertation

by

ALI POURGHORBAN SAGHATI

Submitted to the Office of Graduate and Professional Studies of
Texas A&M University
in partial fulfillment of the requirements for the degree of

DOCTOR OF PHILOSOPHY

Chair of Committee,	Kamran Entesari
Committee Members,	Robert D. Nevels
	Behbood B. Zoghi
	Jun Kameoka
Head of Department,	Miroslav M. Begovic

December 2017

Major Subject: Electrical Engineering

Copyright 2017 Ali Pourghorban Saghati

ABSTRACT

Miniaturization is an inevitable requirement for modern microwave and mm-wave circuits and systems. With the emerging of high frequency monolithic integrated circuits, it is the passive components' section that usually occupies the most of the area. As a result, developing creative miniaturization techniques in order to reduce the physical sizes of passive components while keep their high performance characteristics is demanding. On the other hand, it is the application that defines the importance and effectiveness of the miniaturization method. For example, in commercial handset wireless communication systems, it is the portability that primarily dictates miniaturization. However, in case of liquid sensing applications, the required volume of the sample, cost, or other parameters might impose size limitations. In this thesis, various microwave and mm-wave miniaturization methods are introduced. The methods are applied to various passive components and blocks in different applications to better study their effectiveness. Both component-level designs and system-level hybrid integration are benefited from the miniaturization methods introduced in this thesis. The proposed methods are also experimentally tested, and the results show promising potential for the proposed methods.

ACKNOWLEDGMENTS

“This characteristic of modern experiments - that they consist principally of measurements - is so prominent, that the opinion seems to have got abroad, that in a few years all the great physical constants will have been approximately estimated, and that the only occupation which will then be left to men of science will be to carry on these measurements to another place of decimals.”— James Clerk Maxwell

I would like to express my appreciation to my adviser, Professor Kamran Entesari, who continually conveyed a spirit of adventure in regard to research, and an excitement in regard to exploring and learning new subjects. Without his trust and support, I would not be able to come to the Texas A&M University. Working under his supervision over the past three years, I believe I have learned lessons in this chapter of my life, which their values are far beyond any measure. I would also like to thank Professor Robert Nevels for his kindness, encouragement, and support that have always motivated me through this path. I would like to acknowledge Professor Jun Kameoka for his contribution, and continuous help. I must also thank Professor Behbood Zoghi for his feedback, and kind support.

I want to appreciate Professor Kamal Sarabandi of University of Michigan. I had the privilege to use his wisdom and thoughtful advice over the past few years and during my graduate studies. He has been a true role model, I always admire.

I must appreciate my dear brother, Dr. Alireza Pourghorban Saghati. Not only because of his patience and support as a member of my family, but also due to his contribution and guidance as my senior colleague that has opened gates to me, I would not have been able to open alone. He has always showed me paths I did not know they even exist. I am immeasurably thankful for his sincere helps.

I would also like to thank my officemates and friends, Jaskirat Batra, Sina Baghbani,

Alfredo Costilla, Dr. Vahid Dabbagh Rezaie, Dr. Masoud Moslehi, Dr. Paria Sepidband, Dr. Ehsan Zhian Tabasy, and Shokoufeh Arbabi.

Finally, I would like to express my deep appreciation to my dear parents, Mahkameh, and Javad, whose I wonder, if there is anyway I could express their sacrifices, unconditional love, and trust accurately. It was because of their true support that I was able to build a goal to chase after. They always believed in what I have been doing, and helped me find capabilities in me I was not aware of. With all my heart and to commemorate their love, I dedicate this dissertation to my parents, and my brother.

Ali Pourghorban Saghati

College Station, Texas

September 2017

CONTRIBUTORS AND FUNDING SOURCES

Contributors

All the work discussed in this dissertation is supported by the dissertation advisor, Professor Kamran Entesari.

The work described in chapters two, three, and four is with collaborations of Dr. Alireza Pourghorban Saghati.

The work discussed in chapter five is with collaborations of Professor Jun Kameko of Department of Electrical and Computer Engineering, and Mr. Jaskirat Batra.

All the other work conducted for the dissertation is completed by the student independently.

Funding Sources

There are no funding sources for the works conducted in this dissertation to report.

TABLE OF CONTENTS

	Page
ABSTRACT	ii
ACKNOWLEDGMENTS	iii
CONTRIBUTORS AND FUNDING SOURCES	v
TABLE OF CONTENTS	vi
LIST OF FIGURES	ix
LIST OF TABLES	xvi
1. INTRODUCTION	1
1.1 Miniaturized Substrate Integrated Waveguide Passives	1
1.1.1 Why Substrate Integrated Waveguide and Why Miniaturization?	1
1.1.2 Metamaterial-Inspired Microwave Miniaturization Technique	3
1.1.3 Miniaturized Antenna Array for Millimeter-wave Applications	3
1.2 Miniaturized Dielectric Spectroscopy Sensors, and Systems	4
1.2.1 Why Dielectric Spectroscopy at Microwave Frequencies?	4
1.2.2 Contact-Based Sensing	6
1.2.3 Contact-Less Sensing	7
1.3 Dissertation Overview	7
2. MINIATURIZED SUBSTRATE INTEGRATED WAVEGUIDE RESONATORS, AND FILTERS	10
2.1 Introduction	10
2.2 Resonator Design	12
2.2.1 Full-Mode SIW Resonator	12
2.2.1.1 Miniaturization elements	13
2.2.1.1.1 Capacitive ring gap	13
2.2.1.1.2 Ramp-shaped interdigital capacitor (IDC)	14
2.2.1.1.3 Floating metal patch	16
2.2.1.1.4 Disconnected vias	18
2.2.1.2 Loss	19
2.2.2 Half-Mode SIW Resonator	21
2.2.2.1 Effect of the Center Via Position	21

2.2.2.2	Loss	23
2.2.3	Quarter-Mode SIW Resonator	24
2.2.3.1	Effect of the Corner Via Position	24
2.2.3.2	Loss	25
2.3	Filter Design and Implementation	25
2.3.1	Two-pole bandpass filter	27
2.3.2	Trisection filters	30
2.3.2.1	Filter Synthesis	30
2.3.2.2	Filter Design	33
2.3.2.3	Fabrication and Experimental Results	36
2.4	Discussion	38
3.	MINIATURIZED SUBSTRATE INTEGRATED WAVEGUIDE CAVITY BACKED SLOT ANTENNAS	41
3.1	Introduction	41
3.2	Ultra-Miniature CBSA	42
3.2.1	Miniaturization Procedure	42
3.2.2	Antenna Topology	46
3.3	Fabrication and Experimental Results	49
4.	CIRCULAR ANTENNA ARRAYS FOR MILLIMETER-WAVE APPLICA- TIONS	53
4.1	Introduction	53
4.2	Uniform Circular Array	56
4.3	Single Antenna Element	58
4.4	Circular Power Divider Design	61
4.5	Eight-element Circular Antenna Array	65
4.6	Implementation & Experimental Results	68
5.	COMPACT MICROWAVE DIELECTRIC SPECTROSCOPY SYSTEMS	73
5.1	Introduction	73
5.2	Sensor Design	76
5.2.1	CRLH TLs for Microwave Sensors	76
5.2.2	Sensing Element	80
5.2.2.1	Design Procedure	80
5.2.2.2	Full-wave Simulations	82
5.3	Interferometry System Design	87
5.3.1	System I	87
5.3.2	System II	88
5.3.2.1	Design Procedure	89
5.3.2.2	Non-idealities	92

5.3.2.2.1	Leakage	92
5.3.2.2.2	Temperature Variation	93
5.3.2.2.3	Impedance Mismatch	94
5.3.2.2.4	Fabrication Tolerances	95
5.4	Implementation and Experimental Results	96
5.4.1	Fabrication	96
5.4.2	Calibration, Measurement, and Post-Processing	99
5.4.3	Binary Mixture Characterization	105
5.4.4	Discussion	107
6.	COMPACT CONTACT-LESS ULTRA WIDE BAND DIELECTRIC SPEC- TROSCOPY SENSOR	109
6.1	Introduction	109
6.2	Contact-less Sensor	110
6.3	Implemented Setup and Experimental Results	118
7.	SUMMARY & CONCLUSIONS	120
7.1	Conclusions	120
7.2	Future Works	121
7.2.1	Miniaturized SIW Cavity-based Passive Components	121
7.2.2	Contact-less Dielectric Spectroscopy Systems	122
	REFERENCES	124

LIST OF FIGURES

FIGURE	Page
2.1 (a) Res. I: Normal cylindrical SIW cavity resonator, (b) Res. II: Ring gap-loaded SIW cavity resonator (37% miniaturization). (c) Res. III: Ramp-shaped IDC loaded SIW cavity resonator (57% miniaturization), (d) Res. IV: IDC-loaded SIW cavity resonator employing a rectangular patch in an additional middle metal layer (66% miniaturization), (e) 3D cross-section view of Res. IV (and the simplified LC resonator model), (f) Res. V: IDC-loaded SIW cavity resonator loaded with floating patch and disconnected vias (73% miniaturization), (g) A-A' cross-section view of Res. V.	12
2.2 Miniaturization factor of Res. II for different ring slot dimensions.	15
2.3 (a) Resonance peaks on $ S_{21} $ of Res. III, IV, and V shown in Fig. 1, (b) miniaturization factor and Q_u of Res. III for various number of fingers for the IDC (solid lines are miniaturization factor, and dashed lines are Q_u).	15
2.4 (a) Miniaturization factor of Res. IV for various widths and heights of the patch, (b) The effect of the patch openings and disconnected vias on the miniaturization factor for different heights of the patch.	17
2.5 Magnitude of electric field distribution inside the resonators shown in Fig. 1 at the corresponding resonance frequency.	20
2.6 (a) Original HMSIW resonator, (b) Modified HMSIW resonator, (c), and (d) Magnitude of magnetic field distribution inside the original and modified HMSIW resonators, respectively	22
2.7 (a) Ultra miniature QMSIW resonator, (b) Magnitude of magnetic field distribution inside the original and modified QMSIW resonators.	23
2.8 Top and bottom views of the miniaturized two-pole QMSIW filter. The parameter values are: $W_{CO1} = 4$ mm, $W_{CO2} = 4.4$ mm, $L_{IO1} = 8.9$ mm, $L_{IO2} = 10.9$ mm, and $R_C = 18$ mm.	26
2.9 (a) The coupling factor of the two-pole filter as a function of the spacing between the resonators, (b) the Q_e values as a function of the L-shaped slot length.	27
2.10 Top (left), and bottom (right) views of the two-pole filter prototype.	28

2.11	(a) Ideal, simulated, and measured narrow-band responses of the two-pole filter, (b) measured and simulated wide-band filter responses.	29
2.12	Two possible single-unit trisection topologies.	31
2.13	Synthesized responses of the two trisection filters.	32
2.14	Top and bottom views of the designed Trisection I filter with a controllable transmission zero on lower side of the passband ($R1 = 19$ mm, $R2 = 17.4$ mm, $W_{CO1} = 4.35$ mm, $W_{CO2} = 3$ mm, $L_{IO1} = 7$ mm, $L_{IO2} = 9.5$ mm, $W_m = 1.36$ mm, and $W_f = 25.07$ mm).	33
2.15	Top and bottom views of the designed Trisection II filter with a controllable transmission zero on higher side of the passband ($R1 = 17.4$ mm, $R2 = 20$ mm, $W_{CO1} = 3.3$ mm, $W_{CO2} = 3.6$ mm, $L_{IO1} = 9$ mm, $L_{IO2} = 7.5$ mm, $W_m = 1.36$ mm, and $W_f = 25.07$ mm).	34
2.16	The inter-resonator coupling factors of the two trisection filters as a function of the spacing between the resonators.	36
2.17	Top (left) and bottom (right) views of fabricated, (a) Trisection I, and (b) Trisection II prototypes.	37
2.18	Measured and simulated narrow-band filter responses of, (a) Trisection I prototype, and (b) Trisection II prototype.	38
2.19	Measured and simulated wide-band filter responses of, (a) Trisection I prototype, and (b) Trisection II prototype.	39
3.1	(a) Conventional SIW CBSA, (b) reduced-size CBSA using meandered non-radiating metallic strips, (c) CRLH-based CBSA operating at the -1 resonance frequency, and (d) final ultra-miniature SIW CBSA using a floating metal patch in an additional middle metal-layer.	43
3.2	Simulated S_{11} results of CBSA III, and CBSA IV.	44
3.3	The Effect of h_1 on the miniaturization factor and radiation efficiency of CBSA IV, and the side view of the CBSA IV.	45
3.4	Simulated surface current distribution of CBSA IV at $t = 0, \tau/2$	47
3.5	Antenna configuration, (a) top metal layer view. (b) middle metal layer view. (c) A-A' cross-section view, and (d) bottom metal layer view.	47
3.6	Top (left), and bottom (right) views of the fabricated ultra-miniature CBSA.	49

3.7	Simulated (dashed), and measured (solid) reflection coefficient of the proposed ultra miniature CBSA.	50
3.8	Normalized simulated and measured radiation patterns of the proposed CBSA, (a) E-plane co-Pol., and X-Pol., (b) H-plane Co-Pol. , and X-Pol..	50
4.1	(a) uniform rectangular array, pattern variation in different azimuthal angles are highlighted, (b) circular array with excitation phases rotating 360° provides no variation due to its symmetry.	54
4.2	Geometry of a uniform circular array with a single ring with a radius of R, and element spacing of d.	55
4.3	Azimuthal total radiation pattern of uniform circular ideal half-wavelength dipole antennas with (a) $n = 8$, $R = 0.5\lambda$, (b) $n = 16$, $R = 0.5\lambda$, (c) $n = 8$, $R = 0.75\lambda$, (d) $n = 16$, $R = 0.75\lambda$, (e) $n = 8$, $R = 1.5\lambda$, and (f) $n = 16$, $R = 1.5\lambda$.	57
4.4	Single antenna element configuration: (a) top metal layer view, (b) middle metal layer view, and (c) A-A' cross-sectional view. The dimension values are: $a=2.67$ mm, $D_v=0.4$ mm, $L_s=3.85$ mm, $W_s=0.8$ mm, and $W_f=0.55$ mm.	58
4.5	(a) Simulated reflection coefficient of the circular CBSA, and (b) simulated surface current distribution on the top metal layer of the antenna at $t = 0, \tau/2$.	60
4.6	Normalized simulated E- and H-planes co- and x-pol. radiation patterns of the single CBSA array element at 29 GHz.	60
4.7	(a) Bottom metal layer (power divider bottom view), (b) middle metal layer (power divider top view), and (c) A-A' cross-section views of the designed one-to-eight SIW cavity-based power divider. The dimension values are: $D_1=1$ mm, $D_2=0.6$ mm, $D_{v2}=0.6$ mm, $L_f=1.18$ mm, $L_a=3$ mm, $g=0.1$ mm, $R_p=2.2$ mm, $W_1=0.3$ mm.	62
4.8	(a) E-field, and (b) H-field vector magnitude plots for the power divider. (c) The E-field magnitude distribution on the bottom metal layer of the power divider.	62
4.9	The S_{11} of the radial power divider for various L_f values.	63
4.10	Simulated reflection coefficient of the designed one-to-eight power divider.	64
4.11	(a) Phase response between the input port and each of the output ports, and (b) the isolation between the power divider's output ports.	65

4.12	(a) Multi-layer and cross-sectional A-A' views of the complete eight-element circular CBSA array, and (b) 3D extended view of the complete eight-element antenna array.	66
4.13	(a) Blind via implementation conceptual photos, and (b) top and bottom views of the fabricated eight-element circular antenna array prototype (This picture will be replaced with the actual fabricated prototype photo).	68
4.14	Measured (solid), and simulated (dashed) reflection coefficient of the eight-element circular antenna array.	70
4.15	(a) Measured (solid), and (b) simulated (dashed) normalized co- and cross-polarized radiation patterns of the eight-element circular antenna array in various axial plane cuts.	71
4.16	Measured normalized total 3D radiation pattern of the eight-element circular antenna array with 10° resolution.	71
4.17	Measured gain and radiation efficiency of the proposed eight-element circular antenna array.	72
5.1	(a) CRLH TL unit-cell using microstrip line as the host RH medium, (b) Simplified equivalent LC model of one unit-cell.	77
5.2	Dispersion relation with respect to the series capacitor ($C'_{v,MUT}$) at various frequencies (the parameter values are: $L_{RH} = 2.5$ nH, $C_{RH} = 1$ pF, $L_{CSRR} = 1.85$ nH, $C_{CSRR} = 1$ pF).	79
5.3	(a) Top, (b) bottom, and (c) A-A' cross-section views of the proposed CRLH TL-based fluidic sensor. The parameter values are: $W_m = 2.35$ mm, $W_{ch} = 2.5$ mm, $L_{ch} = 13.4$ mm, $h_{ch} = 3.5$ mm, $L_{IDC} = 5.5$ mm, $R_c = 3.5$ mm, $W_c = 0.25$ mm, $W_g = 2$ mm, $P = 7.35$ mm.	80
5.4	Sensitivity, and bandwidth of the proposed sensor with respect to the number of unit-cells at $f = 4$ GHz.	81
5.5	(a) Simulated E-field distribution of the proposed sensor when the channel is filled with air,(b) simulated e-field penetration into the channel (B-B' side-view) at 4 GHz when the channel is filled with air, and ethanol, (c) E-field strength along the x-direction (the B-B' line), extracting from full-wave simulations in HFSS at $\tau = 0$, where τ is the period of the E-field.	84

5.6	(a) Simulated dispersion curve of the proposed CRLH TL-based sensor for various MUTs, compared to Microstrip line sensor, (b) sensitivity comparison between the proposed CRLH-TL sensor, and the conventional microstrip line sensor using piecewise linear approximation, at $f = 5$ GHz.	85
5.7	Simulated insertion loss of the proposed sensor for various MUTs.	86
5.8	Block diagram of the interferometry-based system I design.	86
5.9	Block diagram of the interferometry-based system II design.	89
5.10	Top view of the Wilkinson power divider, and the two reference, and sensing paths.	91
5.11	Simulated S-parameters of the power divider, and the two reference, and sensing paths, when both the channels are filled with air.	91
5.12	Simulated S_{32} of the structure shown in Fig. 5.10, when both the channels are filled with air.	93
5.13	Ethanol's dielectric properties at various temperatures (ϵ' , and ϵ'' are plotted using Debye- Γ relaxation model [83]).	94
5.14	The return loss (S_{33}) of the sensing CRLH TL shown in Fig. 5.10.	95
5.15	(a) Top view of the fabricated interferometry-based sensor, (b) the complete experimental setup including the instrumentations.	96
5.16	Step-by-step process showing side view for fabrication of the interferometry-based sensor using 3D printed mold and soft lithography.	98
5.17	(a) Simulated (lines), and measured (symbols) $\Delta\phi$ values for xylene (first from bottom), butan-1-ol, propan-1-ol, ethanol, ethyl acetate, ethanediol, methanol, and dmsol (first from top), (b), (c), (d) zoomed measured $\Delta\phi$ values including the error bars resulting from four rounds of measurements, (e) Simulated (lines), and measured (symbols) V_{IF2}/V_{IF3} values for xylene (first from bottom), ethyl acetate, butan-1-ol, propan-1-ol, ethanol, ethanediol, methanol, and dmsol (first from top). (f), (g), (h) zoomed measured V_{IF2}/V_{IF3} values including the error bars resulting from four rounds of measurements.	100
5.18	Measured steady-state temperature of the proposed sensor (at 4.5 GHz) during four rounds of measurements, while the sensing channel is filled with ethanol. The excitation port of the sensor is placed on the bottom side of these pictures.	101

5.19	Measured (a) $\Delta\phi$ and (b) amplitude fraction for the calibration materials as functions of ϵ' , and ϵ'' , respectively, with the power fitted curves (dashed lines).	102
5.20	3D plots of the fitted curves, (a) $\Delta\phi$ and (b) amplitude fraction versus the frequency and ϵ' , and ϵ'' , respectively.	104
5.21	Measured permittivities versus frequency for methanol. The results are compared to theoretical values, and also measured data points from [20]. .	104
5.22	Measured and theoretical permittivities versus the mixing ratio (k) for binary mixtures of (a) ethanol/methanol, and (b) butan-1-ol/propan-1-ol at 5 and 7 GHz with zoomed views for $0 \leq k \leq 0.05$ at 5 GHz and $0.95 \leq k \leq 1$ at 7 GHz.	106
6.1	(a) The proposed conceptual contact-less sensor setup, (b) field regions of the antenna.	111
6.2	(a) Printed UWB antenna used for contact-less sensing, and (b) the top view of the fabricated antenna prototype. The parameter values are: $W = 41$ mm, $W_1 = 32.5$ mm, $W_2 = 42.7$ mm, $L_1 = 17.1$ mm, $L_2 = 8$ mm, $R_1 = 3.5$ mm, $R_2 = 2.85$ mm.	112
6.3	(a) Simulated and measured return loss characteristics of the utilized UWB Vivaldi antenna, and (b) simulated and measured group delay of the setup when the distance between the two antennas is $2d = 60$ mm.	113
6.4	Simulated S11 of the setup when different MUTs are placed in between, and the distance between the two antennas is $2d = 60$ mm.	114
6.5	(a) The two near-field coupled antennas faced each other, and the E-field distribution is shown in middle and at the position of MUT at $f = 3$ GHz, and (b) the E-field distribution in a plane in between the two antennas where the MUT is located at different frequencies. The design values are: $W_{MUT} = h_{MUT} = 51$ mm, and $d = 30$ mm.	115
6.6	The cuvette used to place the liquid MUT in between the two antennas is made of Quartz glass with a volume of ~ 5 ml.	116
6.7	The E-field distribution on the edges of the MUT cuvette at 3 GHz, when (a) $L'_{MUT} = 8.5$ mm $> \lambda/10$ at 10 GHz, and (b) $L_{MUT} = 2$ mm $< \lambda/10$ at 10 GHz.	116

6.8	(a) The proposed contactless setup for liquid chemical sensing, and (b) simulated and measured unwrapped phase difference of the system for various liquid MUTs compared to air as the reference material.	117
6.9	(a) The proposed contactless setup for thickness sensing of solid dielectric slabs , and (b) measured unwrapped phase difference of the system for solid dielectric materials with different thicknesses.	118
7.1	The conceptual system-level block diagram of the compact contact-less BDS system.	122

LIST OF TABLES

TABLE		Page
2.1	Simulated Q_U Factor of The Resonators Shown in Fig. 1	19
2.2	Final Dimensions (mm) of the Ultra-miniature QMSIW Filter	24
2.3	Trisection Filters Specifications and Required Design Values	31
2.4	Comparison of Related Works in Literature	40
3.1	Comparison of Different Miniaturized CBS Antennas	46
3.2	Final Dimensions (mm) of the Ultra-miniature CBSA	49
3.3	Comparison of Related Works in Literature	52
5.1	Comparison of Related Works in Literature	108

1. INTRODUCTION

With the aggressive growing of today's microwave and mm-wave circuits and systems, miniaturization can be considered as an inevitable requirement. This essence shows itself in various forms for different applications. For instance, a wireless handset device at the present time provides various services such as Bluetooth, WiFi, GPS, 4G LTE, etc., which without miniaturization having all these services together could result in an impractically huge device that no one wants to carry. On the other hand, in case of liquid sensing applications, a smaller sensor component might result in a required lower volume of the liquid sample. This can be a crucial factor, for instance in biomedical applications, where the liquid sample might be blood plasma. Therefore, while miniaturization seems necessary, it is the application that defines the importance and effectiveness of miniaturization in that specific area. One primary challenge, however, is the intrinsic trade-off between miniaturization and performance limitations. As a result, various creative miniaturization techniques need to be utilized for different applications in order to make the physical sizes smaller and at the same time keep the high performance characteristics. In this thesis, various miniaturization methods are introduced and utilized for two main category of applications; 1) Substrate Integrated Waveguide cavity passive components, such as filters, and antennas at both microwave and millimeter-wave ranges, and 2) dielectric spectroscopy sensors, and systems with two main subcategory of contact-based and contact-less sensing.

1.1 Miniaturized Substrate Integrated Waveguide Passives

1.1.1 Why Substrate Integrated Waveguide and Why Miniaturization?

Antennas and passive filters, as essential blocks of any wireless communication system, generally occupy the most area of modern front end transceivers. Therefore, miniaturization of such components while maintaining the high performance characteristics can

be considered as one of the most prominent challenges. In this area, passive resonators are essential blocks of many microwave and mm-wave filters and antennas. High quality factor, high isolation, low loss, low cost, and integrability of the resonators are some of the considerations that need to be taken into account. For decades, the classical waveguide and cavity technologies were utilized to design and implement resonators with high performance characteristics. More complex passive devices were then introduced such as highly selective filters, couplers, diplexers, and antennas, based on using the same technology [1, 2]. However, with the ever-increasing highly integrated circuits and systems, such bulky, and heavy structures became impractical for many of the today's miniature wireless systems and applications.

It was in 1998 when via posts were utilized in a single layer substrate in order to achieve planar parallel plate waveguide with transverse electromagnetic (TEM) mode excitation for the first time [3]. Later in the same year, "laminated waveguide" was introduced for mm-wave applications, which was based on a very similar method of using via posts between the metal walls on the top and bottom sides of the substrate in a planar fashion [4]. In 2003, substrate integrated waveguide (SIW) was introduced for the first time, which then opened a gate to complete integration of planar circuits and waveguide-based components on a same substrate and in a planar fashion [5]. Over the past decade, tremendous efforts have been resulted in various microwave and mm-wave passive circuits and components such as filters, and antennas based on the SIW technology [6, 7].

Even though, integration of passive components and active circuitry in a planar fashion became feasible based on the SIW technology, the planar size of SIW-based components are relatively large compared with modern monolithic integrated circuits as it depends on the desired wavelength of operation. As a result, the use of SIW-based passive filters and antennas in today's compact wireless devices is highly contingent upon their miniaturization. Loading the SIW cavity with defected ground structures [8], utilizing metamaterial-

inspired structures to push the SIW cavity to operate below its cut off frequency [9], or cutting the SIW cavity on its fictitious magnetic wall [10] are some of the utilized approaches. However, the maximum achievable miniaturization factor using such methods is highly limited.

1.1.2 Metamaterial-Inspired Microwave Miniaturization Technique

Due to the need for ultra-compact passive filters and antenna with high performance specifications, a miniaturization method is proposed by which the size can be reduced by around 90%. This method is applied to both cavity-based passive filters and antennas [11–13]. Ramp-shaped slots as interdigital capacitors are introduced in various SIW cavity resonators to push the structure to operate in the first negative order resonance mode. Such a mode cannot be excited in conventional SIW structures. Also, a floating metal patch in the middle metal layer along with disconnected vias is used to further load the structure, and accordingly increase the miniaturization factor. Due to the adaptation capabilities, the proposed miniaturization method can also be applied to other passive components, such as SIW couplers, diplexers, etc., and also can be adjusted for any desired frequency bands in the microwave and mm-wave range. The proposed technique and the implementations are thoroughly discussed in chapters 2, and 3.

1.1.3 Miniaturized Antenna Array for Millimeter-wave Applications

While miniaturization based on exciting the negative-order resonances is proven to be useful for SIW cavity-based antenna design at the microwave range [13], this method is not easily applicable at mm-wave range since the size of the cavity resonators are relatively small, and there is not enough space for capacitive loading elements, such as ramp-shaped interdigital slots. More importantly, imposing such miniaturization elements could cause the gain of the antenna to drop significantly at mm-wave range. On the other hand, it is noteworthy that antenna arrays are most commonly utilized for mm-

wave applications rather than a single antenna element. This is primarily due to the severe path loss/attenuation at mm-wave band. Various linear and rectangular antenna arrays have been implemented for mm-wave applications, i.e. 5th generation (5G) wireless systems [14,15]. However, it has been theoretically discussed and proven that circular antenna arrays have various advantages due to the intrinsic axial symmetry in their configuration compared with linear or rectangular arrays [16]. Even though, the application of circular arrays at mm-wave range seems promising, their implementation for 5G applications seems less-discussed in the literature. In this thesis, an eight-element compact circular antenna array is proposed in chapter 3, and implemented based on SIW cavity technology. A multi-layer 3D configuration is utilized for the integration of the power divider and the antennas to achieve a more compact physical size. The proposed method is based on operating at the cut-off resonance frequency of the cavities, and therefore, a relatively high radiation efficiency is achieved for 5G applications.

1.2 Miniaturized Dielectric Spectroscopy Sensors, and Systems

1.2.1 Why Dielectric Spectroscopy at Microwave Frequencies?

The dielectric characteristic of materials is a unique property similar to fingerprints. It is this property that relates physical and chemical structure of the material to its electrical properties such as conductivity or loss. The detection, and characterization of the dielectric properties of materials is called dielectric spectroscopy [17]. The dielectric property of materials is dependent on various factors, which frequency is one of the most prominent ones. Therefore, the operating frequency of the dielectric spectroscopy system plays a major role in its functionality to detect different materials. In this case, microwave dielectric spectroscopy becomes specifically important for various reasons, some of which are as below [18]:

- Many medical and biomedical sensing applications can be benefited from microwave

dielectric spectroscopy since biomolecules or biocells in blood or semen, are responsive at radio frequency and microwave range. As a result, biochemical and biological sensing for disease diagnosis is one major application of such systems.

- With the fast growing of wireless communication systems over the past decade, the effect of such electromagnetic signals at microwave range on living species needs to be studied for health care and safety matters.
- The effectiveness of microwave dielectric spectroscopy is not bounded to medical or biomedical applications. It is a powerful technique with a broad range of other applications such as food and drug safety, ground or soil characterization , and oil exploration industry [19].

Any microwave dielectric spectroscopy system requires a sensing element, which can be contact-based, or contact-less upon the application. The contact-based sensor is when the sensing element is in direct contact with the material-under-test (MUT), while contact-less sensing is when the material is detected, and characterized remotely, and therefore, the sensing elements have no contact with the MUT. One of the most established methods of contact-based sensing is based on utilizing an open-ended coaxial waveguide, which is exposed to the MUT from its open end [20]. In this case, the material can be characterized based on measuring the reflection coefficient from the other end of the waveguide using a vector network analyzer (VNA). This bulky sensing setup occupies a large area, and not suitable for lab-on-a-board applications. On the other hand, contact-less microwave sensing is primarily implemented based on free space techniques [21,22]. In this case, the detection is based on either having two antennas faced to each other in the far-field with the MUT in middle, and the transmission coefficient is measured and utilized for material characterization, or single antenna is employed and the dielectric spectroscopy is achieved by measuring the reflection coefficient. In either case, the measurement setup is bulky,

and not very practical for low-volume material characterization as it is implemented in the far-field of antennas operating at microwave range. As a result, even though both contact-based, and contact-less sensors have been proven to be useful for many applications, still their miniaturization requires attention to achieve more compact robust passive sensor devices.

1.2.2 Contact-Based Sensing

Two important factors of microwave DS systems are their operational bandwidth, and sensitivity. Since the materials' dielectric properties are frequency dependent, a wide-band system is desirable since it reveals more information about the material-under-test rather than a system that operates at a single frequency. Moreover, the system need to have enough resolution (sensitivity) to be able to successfully characterize different materials with very close dielectric properties. However, there is a tradeoff between these two factors, and therefore, the previously-reported approaches suggest either high sensitivity with single- or narrow-band operation [23], or wide operational bandwidth but with highly limited sensitivity [24]. On the other hand, in many applications, such as protein, DNA sensing, or glucose-level measurement, the material-under-test is in a liquid solution. Liquid material sensing requires a platform to provide the necessary interaction between the sensor circuitry and the liquid material.

Due to the demand for highly sensitive and wideband liquid chemical sensing, with a compact platform suitable for practical lab-on-a-board applications, a new technique based on utilizing metamaterial-inspired transmission line as the sensing element in a direct down-conversion interferometry configuration is presented [25, 26]. In this case, the output is a DC voltage, which can be read with a simple multimeter. The unique nonlinear dispersive properties of the utilized artificial transmission line, and the wideband nature of the proposed system result in complete DS over a broad frequency range, while the sen-

sitivity (resolution) is considerably improved compared with a conventional sensor in this area. Moreover, a hybrid integration method is introduced for the first time, which all the passive components, active circuits, and the fluids are integrated on a single board. The proposed platform suggests liquid material characterization with volumes in the range of few milliliters.

1.2.3 Contact-Less Sensing

Liquid material characterization has different aspects. Another challenge in this area is when the liquid under test is hazardous. Also the material can be acidic which in case of contact with the sensing circuitry, it can cause damage to the sensor. Therefore, the sensor needs to be replaced after each measurement which is neither practical nor cost effective. In such cases, contactless sensing becomes important. However, there are very few approaches reported for microwave contactless material characterization, each of which requires a bulky measurement setup at microwave frequency range, and therefore not suitable for low-volume liquid material sensing [27, 28]. Based on the demand for compact contactless liquid material characterization, a near-field contactless sensor which covers the whole standard ultra-wide band (UWB) frequency range is designed, implemented, and experimentally tested [29]. Two antennas are coupled to each other and the liquid material is placed in middle. This method is useful since it provides contactless microwave sensing in a compact fashion covering the ultra-wide bandwidth. It is also experimentally shown that the setup is suitable for solid material thickness sensing.

1.3 Dissertation Overview

This dissertation targets to introduce miniaturization techniques suitable for two main category of applications. First, it is aimed to discuss compact SIW cavity-based passive resonators, filters, and antennas at both microwave and millimeter-wave ranges through chapters II-IV. Second, compact contact-based and contact-less microwave dielectric spec-

troscopy sensors are targeted, and the miniaturization of such systems is discussed through chapters V-VI.

Chapter II focuses on the SIW-based cavity resonators, and filters. Various miniaturization elements are introduced and utilized, while each one's limitations are also discussed. A combination of ramp-shaped interdigital slots, the floating metal patch in a middle metal plane, and disconnected via posts are utilized to achieve $\sim 90\%$ of miniaturization. A two-pole, and two trisection bandpass filter prototypes are designed and fabricated. The theoretical, simulated, and measured results are also compared to better demonstrate the effectiveness of the presented miniaturization methods.

In chapter III, the applicability of the miniaturization elements, the interdigital ramp-shaped capacitor, and the floating metal patch in middle metal layer, introduced in Chapter I, to the SIW cavity-backed slot antenna (CBSA) is studied. An ultra miniature SIW CBSA is also fabricated, which good agreement between measurement and simulation results proves the potential of these miniaturization methods in different SIW cavity-based passive components.

Chapter IV discusses the potential of SIW cavity-based antennas for mm-wave applications. The focus is to discuss SIW circular antenna arrays for 5th generation wireless cellular systems. A one-to-eight power divider is designed and presented in this chapter based on utilizing a mm-wave SIW cylindrical cavity resonator, which is capable of feeding eight CBSAs in a circular configuration using a multi-layer 3D structure. Finally, an eight-element SIW cavity-based antenna array is implemented, and simulated, and measured results are compared.

As was mentioned earlier, the focus of the dissertation shifts to compact contact-based, and contact-less dielectric spectroscopy sensors, and systems at microwave range through chapters V-VI. In chapter V, the application of metamaterial-inspired composite right/left-handed (CRLH) transmission lines for liquid sensing is studied. A fluidically-loaded

CRLH transmission line is presented as a contact-based sensor with improved sensitivity for microwave liquid dielectric spectroscopy. The proposed sensor is utilized in an interferometry system design, as was discussed in section 1.2.1. The fabricated prototype is measured for both pure and binary mixtures liquid materials, which shows high accuracy of the proposed method.

Contact-less sensing in a compact fashion at the microwave range is mainly targeted in chapter VI. Near-field sensing is proposed as a compact solution. Vivaldi antennas are utilized as sensing elements, while solid and liquid materials are detected using this contact-less sensor. Electromagnetic field analysis is also provided to better demonstrate the near-field operation of the proposed method.

Finally, chapter VII concludes the dissertation, and provides future potential works. The method disclosed in chapter II can be extended to more complex passive filter configurations, such as SIW cavity-based bandstop filters. Moreover, these methods are potentially applicable to other SIW-based passive components, such as SIW couplers, diplexers, etc. For example, the trisection filters, proposed in chapter II, can be utilized to construct a SIW cavity-based diplexer. On the other hand, the contact-less near-field sensor, disclosed in chapter VI, can be utilized as a part of a complete self-sustained dielectric spectroscopy system, in which vector network analyzers are removed from the testing setup. Moreover, since the sensor provides UWB standard frequency operation, it is compatible with both frequency- and time- domain measurement procedures. As a result, integrated self-sustained contact-less microwave sensing in time-domain can be achieved.

2. MINIATURIZED SUBSTRATE INTEGRATED WAVEGUIDE RESONATORS, AND FILTERS

2.1 Introduction

Low loss bandpass filters, constructed using compact high- Q resonators are one of the essential blocks of modern wireless communication systems. Ease of fabrication, high-power handling, high linearity, and integration compatibility of substrate integrated waveguide (SIW) cavity resonators make them a good candidate for high-performance microwave filters [30]. Despite their advantages, their use in compact microwave devices is hindered due to their large size. As a result, miniaturization techniques need to be employed to reduce the size of SIW filters, while maintaining the high performance characteristics [11].

The existing work in the area of miniature SIW filters includes loading the SIW resonator using defected ground planes (DGS) and ring gaps [8, 31], using complementary split-ring resonators to change the characteristic cutoff frequency of the SIW structure [32], forcing the SIW resonator to operate at lower-order modes (e.g. -1^{st} mode) using metamaterial-inspired components [33], and cutting the SIW resonators on their fictitious magnetic walls to achieve half-mode SIW (HMSIW) or quarter-mode SIW (QMSIW) resonators [10,34,35]. Among these, the largest miniaturization factor belongs to the QMSIW with roughly 75% of size reduction. The miniaturization factor for the other methods such as the CSRR-loaded resonators, and the negative order resonance-mode ones is limited by the geometrical dimensions of the employed loading structures and the area available on

©2015 IEEE. Part of this chapter is reprinted, with permission from the Institute of Electrical and Electronics Engineers (IEEE), "Ultra-miniature SIW Cavity Resonators and Filters," IEEE Transactions on Microwave Theory and Techniques, Dec. 2015.

©2015 IEEE. Part of this chapter is reprinted, with permission from IEEE, "An ultra-miniature quarter-mode SIW bandpass filter operating at first negative order resonance," IEEE International Microwave Symposium (IMS), May. 2015.

the top/bottom walls of the SIW cavity.

Ultra-miniature HMSIW and QMSIW resonators are proposed in this section, which the first negative order resonance is excited to further decrease the size of the resonators. The mentioned issue of size limitations for loading structures becomes more severe for the case of HMSIW/QMSIW resonators. Accordingly, based on the method first proposed in [36], ramp-shaped slots as interdigital capacitors (IDC) on the top metal layer of the cavity structure are employed to efficiently use the available resonator area. Also, by employing an additional middle metal layer, a loading patch is employed to increase the capacitance value of the loading IDCs. Finally, disconnected via posts are inserted in the locations of maximum E-field distribution to increase the miniaturization beyond the limits defined by the size of the IDCs. Using these elements, 90% miniature HMSIW, and 95% miniature QMSIW resonators are achieved.

The miniature QMSIW resonator was first introduced by the authors in [11], and was used toward the design of a two-pole filter operating at a center frequency of 690 MHz with an area of $\sim 0.09\lambda_0 \times 0.05\lambda_0$ and a fractional bandwidth of 5.9%. Here, a more in-depth study on the miniaturization method is conducted. Also, the half-mode SIW version of the resonator is provided. Moreover, a combination of an HMSIW and two QMSIW resonators is uniquely employed to design two different trisection filters with controllable transmission zeros on either side of the passband. In addition to the miniaturization due to area reduction (HMSIW-QMSIW combination instead of 3 SIW resonators), frequency shift due to the loading IDC structure and disconnected vias results in 70% of size reduction in comparison with a normal full-mode SIW resonator. As a result, the entire area of the trisection filter consumes roughly 30% of the area for *only one* full-mode SIW cavity resonator at the operating frequency. The two trisection filters have midband frequencies of 912 MHz, and 754 MHz with total areas of $\sim 0.12\lambda_0 \times 0.12\lambda_0$, and $\sim 0.1\lambda_0 \times 0.1\lambda_0$, respectively. In comparison with the existing SIW-based trisection

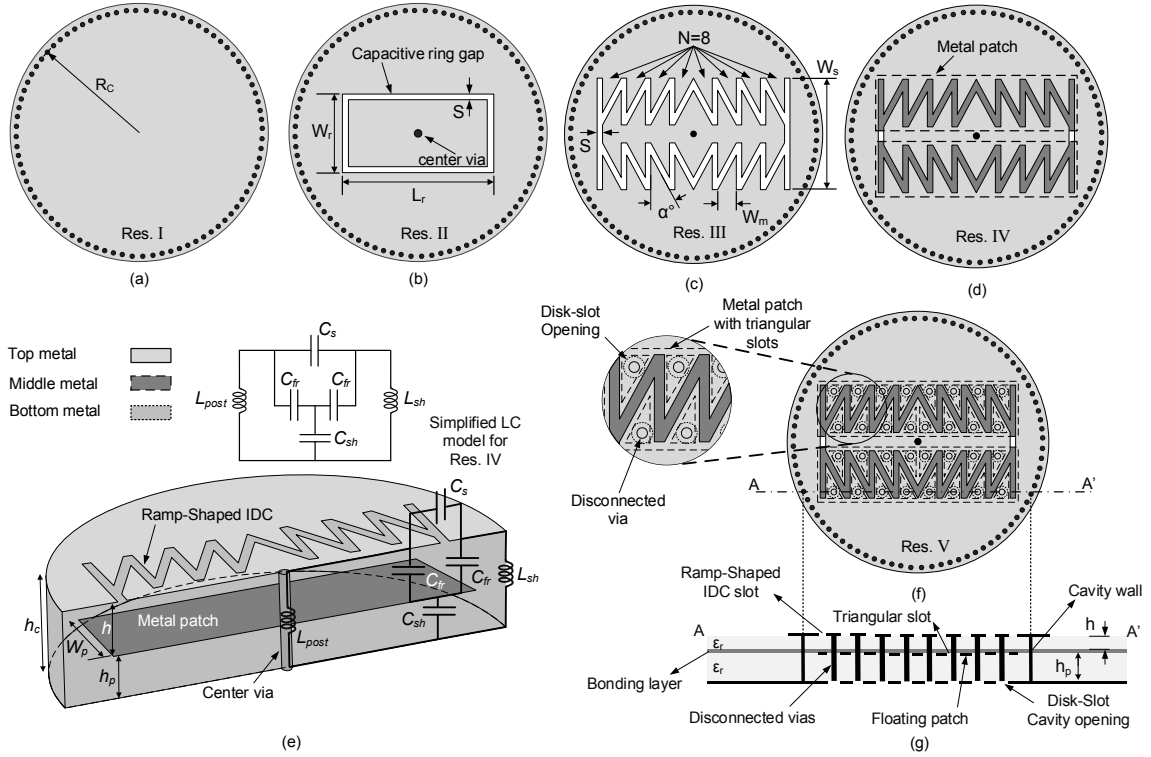


Figure 2.1: (a) Res. I: Normal cylindrical SIW cavity resonator, (b) Res. II: Ring gap-loaded SIW cavity resonator (37% miniaturization). (c) Res. III: Ramp-shaped IDC loaded SIW cavity resonator (57% miniaturization), (d) Res. IV: IDC-loaded SIW cavity resonator employing a rectangular patch in an additional middle metal layer (66% miniaturization), (e) 3D cross-section view of Res. IV (and the simplified LC resonator model), (f) Res. V: IDC-loaded SIW cavity resonator loaded with floating patch and disconnected vias (73% miniaturization), (g) A-A' cross-section view of Res. V.

filters in literature [37–40], the proposed trisection filters are the first ones which are ultra-compact, while having controllable transmission zeros, to the best of author’s knowledge.

2.2 Resonator Design

2.2.1 Full-Mode SIW Resonator

Fig. 2.1 demonstrates the procedure used to achieve the miniaturized SIW cavity resonator. Res. I, shown in Fig. 2.1(a), is a conventional cylindrical SIW cavity resonator which its dimensions are determined based on the fundamental TM₀₁₀ mode [41]. Based

on a Rogers RT/Duroid 6010 ($\epsilon_r = 10.2$, $\tan\delta = 0.0023$)¹ dielectric layer with a thicknesses of $h_c = 3.135$ mm, R_C is calculated to be 17.4 mm. As a result a fundamental TM₀₁₀ mode exists around 2 GHz. For a fixed resonator size, inserting proper elements into the structure will reduce the resonance frequency. The miniaturization factor for a particular miniaturized resonator operating at a lowered frequency of f_0 is computed using

$$\text{Miniaturization factor}\% = \frac{A_{siw,f_0} - A_c}{A_{siw,f_0}} \times 100 \quad (2.1)$$

where A_{siw,f_0} is the area of a conventional cylindrical SIW resonator, which fundamentally operates at f_0 , and A_c is the area of the proposed resonators. This miniaturization factor contribution for each element is mentioned in the caption of Fig. 2.1.

2.2.1.1 Miniaturization elements

2.2.1.1.1 Capacitive ring gap First, the SIW cavity resonator is loaded with a shunt via at the center (Fig. 2.1(b)). Afterwards, a ring slot is etched on the top wall to disconnect this wall from the bottom wall. The ring gap can be modeled as small series capacitance which loads the resonator and results in a lower resonance frequency. The capacitance value, as a function of physical dimensions, can be approximated based on the approach provided in [31]. The frequency down-shift due to this capacitive loading is mainly limited by the size of the annular gap. To better understand this limitation, the structure is simulated using commercial High Frequency Structure Simulator (HFSS)², for various W_r , and L_r values, while S is fixed to 0.75mm, and the results are shown in Fig. 2.2(a). As can be seen, increasing the width and length of the ring gap results in higher miniaturization factors. However, these two dimensions are limited by the size of the cavity which is assumed to be fixed for all the resonators. Fine tuning of the resonance frequency is also feasible

¹Rogers Corp., Brooklyn, CT, USA.

²Ansys HFSS ver. 15, Ansys Inc., Canonsburg, PA, USA, 2013.

by adjusting the spacing value of the ring-gap (S). Considering $W_r = 4mm$, $L_r = 8mm$, and $S = 0.75mm$, $\sim 37\%$ miniaturization is achieved.

2.2.1.1.2 Ramp-shaped interdigital capacitor (IDC) Fig. 2.1(c) shows Res. III in which the ring slot on the top metal layer is replaced by ramp-shaped slot [36]. In this figure, W_s is the total width of the ramp-shaped slot etched on the top metal wall of the cavity, while α is the angle between the adjacent slots. Similar to Res. II, S stands for the spacing value of the slot-gap, and its value remained $0.75mm$ for Res. III, IV, and V. The cavity-wall vias and center via can be modeled as shunt inductors. Therefore, utilizing IDC, as an equivalent series capacitance, forces the SIW resonator to operate at -1^{st} resonance [33]. This is basically different from Res. II, where the fundamental resonance frequency is shifted down due to the capacitive loading effect of the annular gap, and as a result, the operating mode is quasi-TEM [31]. In order to observe the 1^{st} , 0^{th} , and -1^{st} resonances, Res. III is simulated as a two-port resonator, and the resonance peaks on $|s_{21}|$ are plotted and shown in Fig. 2.3(a). In this figure, the frequency is normalized to the fundamental TM010 resonance frequency. For this resonator, the zeroth and first negative order resonances happen at 0.8, and $0.43 \times f_{TM010}$, respectively. In this case, increasing the series capacitive loading results in further shifting down the -1^{st} resonance frequency rather than the fundamental mode.

Similar to traditional IDC structures, for a constant total area of the IDC, higher equivalent series capacitance values are achievable by increasing the number of fingers [42]. For the ramp-shaped configuration, assuming the total size of the IDC is constant, increasing the number of fingers (N) is feasible by decreasing the angle between the adjacent slots (α). The effect of the ramp-shaped slot physical dimensions on the miniaturization factor is studied by simulating the resonator for various W_s , and α values, while the number of fingers are changed accordingly. The results are shown in Fig. 2.3(b). According

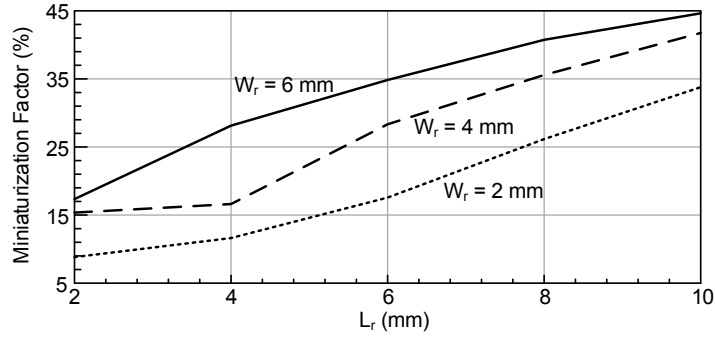


Figure 2.2: Miniaturization factor of Res. II for different ring slot dimensions.

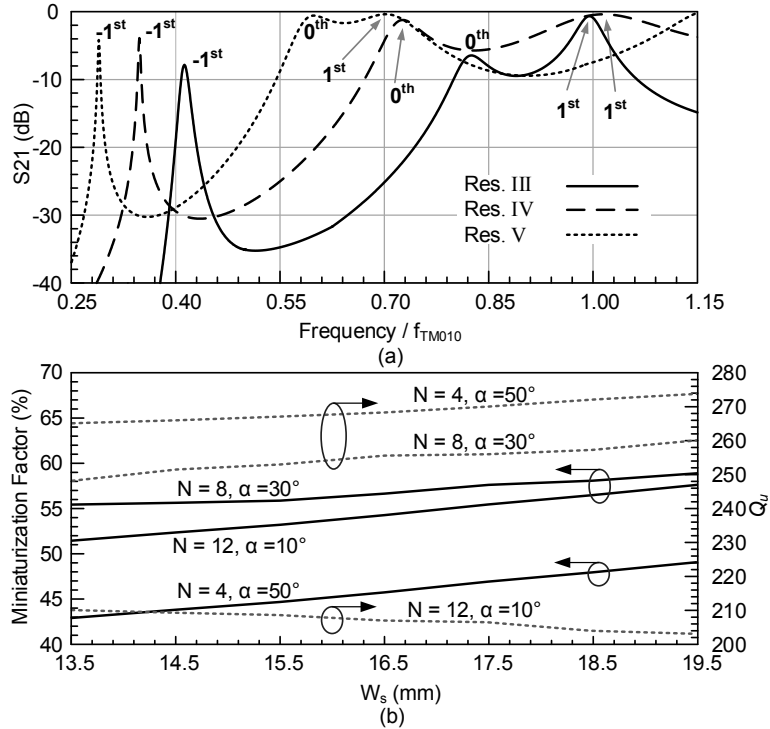


Figure 2.3: (a) Resonance peaks on $|S_{21}|$ of Res. III, IV, and V shown in Fig. 1, (b) miniaturization factor and Q_u of Res. III for various number of fingers for the IDC (solid lines are miniaturization factor, and dashed lines are Q_u).

to the available area on the cavity top-metal wall (for $R_C = 17.4$ mm), by decreasing α from 50° to 30° , the maximum possible number of fingers is increased from 4 to 8, and

consequently, higher miniaturization factors are achieved. However, further decreasing α to lower than 30° means drastic reduction in the fingers' metal width (W_m). As a result, higher capacitance values cannot be achieved for α values less than 30° , and the miniaturization factor drops for $\alpha = 10^\circ$. Moreover, this trade-off between N , and W_m results in another bottleneck. Reduction in the metal width of each finger will reduce the quality factor of the IDC, and the resonator [42]. This is also shown in Fig.2.3(b) where, the unloaded quality factor (Q_U) of Res. III is plotted for each case. Therefore, the optimum values of $\alpha = 30^\circ$, and $N = 8$ are employed for this design. On the other hand, W_s has small effect on the -1^{st} resonance frequency, and can be used for fine tuning.

The spacing value (S) has minor effect on the miniaturization factor of Res. III, while very large values of S can cause the Q_U of the resonator to drop. This is mainly due to increased leakage loss from the top interdigital slot. By increasing S from 0.75mm to 1.75mm, the -1^{st} resonance frequency only reduces by $\sim 3.1\%$, however, the Q_U value drops from 253 to 221. On the other hand, for $S \leq 0.75mm$, the leakage loss from the top IDC slot is roughly constant, and neither the miniaturization factor, nor Q_U value change considerably. Therefore, considering $S = 0.75mm$, and $W_s = 15.5mm$, the miniaturization factor is roughly 57% for Res. III.

2.2.1.1.3 Floating metal patch To further increase the capacitive loading and thus the frequency shift, a floating metal patch is inserted in an additional middle metal layer beneath the ramp-shaped slot (Res. IV shown in Fig. 2.1(d)). As can be seen in Fig. 2.3(a), by employing this metal patch, the -1^{st} resonance frequency is shifted down to a lower value compared to Res. III. To better demonstrate the capacitive loading effect of this floating patch, a 3D cross-section view of Res. IV is shown in Fig. 2.1(e). In this figure, the shunt capacitance to the ground (between the patch and the cavity bottom wall) and the two fringing capacitances (between the ramp-shaped slot edges and the patch) are named as

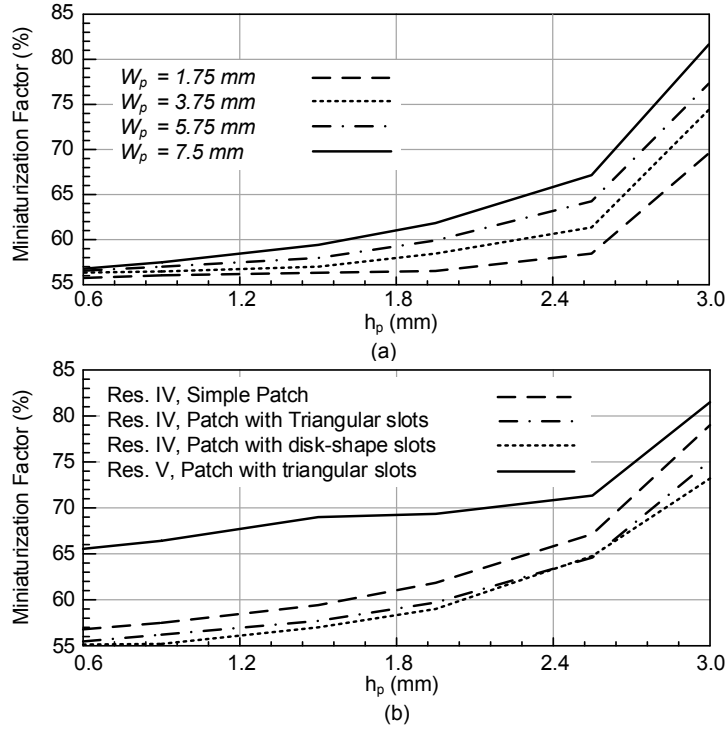


Figure 2.4: (a) Miniaturization factor of Res. IV for various widths and heights of the patch, (b) The effect of the patch openings and disconnected vias on the miniaturization factor for different heights of the patch.

C_{sh} , and C_{fr} , respectively, and C_s stands for the equivalent series capacitance introduced by the ramp-shaped interdigital slot. For simplicity, the metal planes are assumed perfect electric conductors, and parasitics are excluded. As can be seen, the patch increases the effective series capacitance as follows:

$$C_{S,eff} = C_S + \frac{C_{fr}^2}{C_{sh} + 2 \times C_{fr}}. \quad (2.2)$$

While C_{sh} should be minimized, C_{fr} needs to be maximized to increase the overall series capacitance and achieve more miniaturization. The effect of the size and location of the patch on shifting down the -1^{st} resonance frequency is studied by simulating the structure for various widths (W_p) and heights (h_p) for the patch, and the results are shown

in Fig. 2.4(a). While W_p can be used for fine adjustment, h_p needs to be maximized to reduce C_{sh} , increase two C_{fr} values, and to achieve the highest miniaturization factor. However, this dimension is limited by the height of the standard substrate thickness used for the floating patch. Therefore, considering $W_p = 7.5$ mm for highest miniaturization, h_p is chosen to be 2.5 mm, while h is 0.635 mm, based on the availability of standard Rogers RT/Duroid 6010 substrate thicknesses and fabrication constraints. By using this structure, a miniaturization factor of 66% is achieved.

2.2.1.1.4 Disconnected vias Disconnected vias are the last loading elements (Fig. 2.1(f)) to increase the miniaturization factor. These capacitive disconnected via posts will further load the cavity and push the -1^{st} resonance frequency to even lower values (Fig. 2.3 (a)). The loading effect of disconnected vias and their design considerations are well-studied in [43]. They need to be placed where the E-field distribution is maximum inside the cavity to have the highest loading effect. Fig. 2.1(f), and Fig. 2.1(g) show the top and 2D cross-section views of the final resonator (Res. V), respectively, in which the patch and the disconnected vias are both inserted. The loading via posts are disconnected from the bottom wall of the cavity by using disk-slot openings. These openings are relatively small compared to wavelength at operating frequencies, and the leakage is negligible [43]. Also, capacitive via posts need to be disconnected from the floating metal patch to avoid shortening it to the top metal wall. This can be done by etching either circular disk- or triangular-shaped slots on the floating patch and around the vias. The opening slots on the floating patch should have minimum effect on the equivalent fringing capacitances between the patch and the ramp-shaped slot edges (C_{fr}). In order to better study the effect of the opening slots on the miniaturization factor, the simple patch in Res. IV is replaced with a patch with triangular-shaped slots, and a patch with disk-shaped slots, respectively. Then, the two modified resonators are simulated for different heights of the patch and the

Table 2.1: Simulated Q_U Factor of The Resonators Shown in Fig. 1

Resonators	Eigen mode	Q_U
Res. I	Fundamental mode (@2.07 GHz)	312
Res. II	Fundamental mode (@1.65 GHz)	234
Res. III	-1^{st} -order mode (@0.94 GHz)	253
Res. IV	-1^{st} -order mode (@0.70 GHz)	263
Res. V	-1^{st} -order mode (@0.57 GHz)	246

results are compared to the original Res. IV in Fig. 2.4(b). As can be seen, etching the slots on the patch will slightly reduce the miniaturization factor of Res. IV, however, there is no significant difference between utilizing patch with disk- or triangular-shaped slots. In this design, triangular slots are etched on the metal patch to disconnect it from the loading vias, and avoid shortening it to the top metal wall (Fig. 2.1(f)-(g)). Afterwards, disconnected vias are inserted, and the final resonator is also simulated for different heights of the patch. Inserting disconnected vias results in higher miniaturization factors compared to Res. IV for any height of the patch with triangular slots. By employing all the miniaturization elements, $\sim 73\%$ of miniaturization is achieved. Ramp-shaped IDC has the most effect on miniaturization as it forces the resonator to operate at -1^{st} resonance mode.

2.2.1.2 Loss

To study the loss mechanism of the presented resonators, the unloaded quality factor is extracted from two-port s-parameters simulation, based on the approach in [1]. The top, middle, and bottom metal layers are all considered as copper (1 Oz.), and as mentioned before, both substrate layers are Rogers RT/Duroid 6010 ($\epsilon_r = 10.2$, $\tan\delta = 0.0023$) with different thicknesses of $h_p = 2.5$ mm, and $h = 0.635$ mm. For Res. III to V, the two dielectric layers are bonded together using Rogers RO4450B pre-preg material ($\epsilon_r = 3.3$, $\tan\delta = 0.004$, $h_{bond} = 0.09$ mm). Each single resonator is weakly coupled at the input/output ports, and simulated. The resulting unloaded quality factors are shown in Table 2.1.

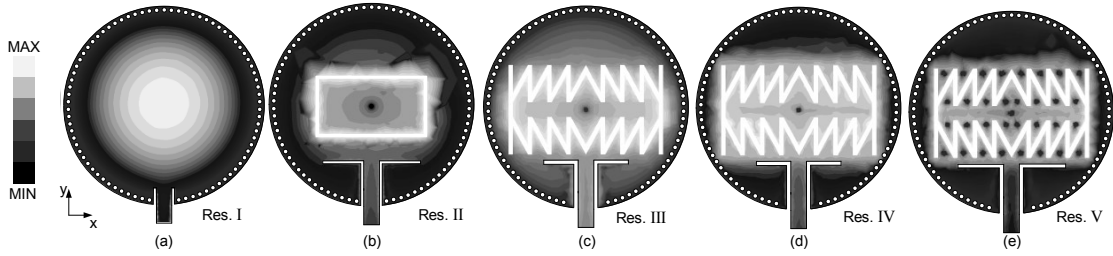


Figure 2.5: Magnitude of electric field distribution inside the resonators shown in Fig. 1 at the corresponding resonance frequency.

The loss mechanism of a regular SIW cavity resonator (Res. I) has been investigated in literature [44]. Using a low-loss dielectric layer, the leakage loss from the apertures between the side-wall vias is negligible if the vias are placed close enough to each other [8]. Therefore, for such resonators, conductor loss and dielectric dissipation have the main contribution to Q degradation. The Q -factor of a conventional rectangular SIW cavity resonator is reported ~ 500 at the fundamental resonance frequency [8], while the ϵ_r and the $\tan\delta$ of the employed dielectric material are 3, and ≤ 0.001 , respectively. However, using high-permittivity dielectric materials such as Rogers 6010, with higher loss tangent of 0.0023, Q -factor drops to 312 for Res. I in this design. Moreover, other loss factors need to be considered carefully as different miniaturization elements are added to the resonator. As can be seen in Table 2.1, Res. II has a lower Q_U value compared to Res. I. This is mainly because of leakage loss from the annular ring gap on the top metal wall. The leakage loss can be minimized by increasing the equivalent capacitance introduced by the ring-gap. This means that by increasing the miniaturization factor, the leakage loss decreases. To better discern this relation, the magnitude of E-field distribution is plotted for all resonators in Fig. 2.5. The center via post and the capacitive elements around it force the maximum E-field distribution to be around the capacitive elements. As this capacitive loading effect increases by inserting IDC, metal patch, and the disconnected vias,

the operating frequency of the resonator is pushed down to lower values, and hence, the wavelength becomes larger. This means that the size of the resonator relative to its operating wavelength becomes smaller as miniaturization increases. As a result, the leakage loss decreases for resonators with higher miniaturization factors, and Res. III, IV, and V have larger Q_U values compared to Res. II. Based on this argument, Res. V is expected to have less radiation loss and better Q_U compared to Res. III, or IV. However, this resonator has another source of leakage which is the disk-slot openings on the bottom wall of the cavity. As a result, the Q is degraded compared to Res. III, and IV.

2.2.2 Half-Mode SIW Resonator

The miniaturization method introduced in the previous subsection was based on exciting the -1^{st} resonance of a regular SIW cavity, and shift that resonance down to the lowest possible value by loading the cavity. In order to design a more compact resonator, the proposed method is applied to a HMSIW cavity resonator (Fig. 2.6). First, the regular SIW resonator (Res. I) is bisected on its fictitious magnetic wall. For a large diameter to height ratio of the cavity, the leakage from the open wall would be negligible, and the resonator will operate at roughly a same resonance frequency [10]. Then, all the above miniaturization elements are inserted to achieve a HMSIW resonator which operates at -1^{st} resonance. While, the frequency of operation remains approximately the same compared to Res. V (Fig. 2.1(e)), the size is reduced by half.

2.2.2.1 Effect of the Center Via Position

Fig. 2.6(a), (b) show the top view of two possible configurations for the miniaturized HMSIW cavity resonator. The difference between these two resonators is the place of the center via. As Res. V (Fig. 2.1(f)) is bisected to achieve the HMSIW resonator, the center via can be either kept at the same position, or replaced by two other shunt vias at the two ends of the ramp-shaped slot (Fig. 2.6(b)). While the original HMSIW resonator is useful

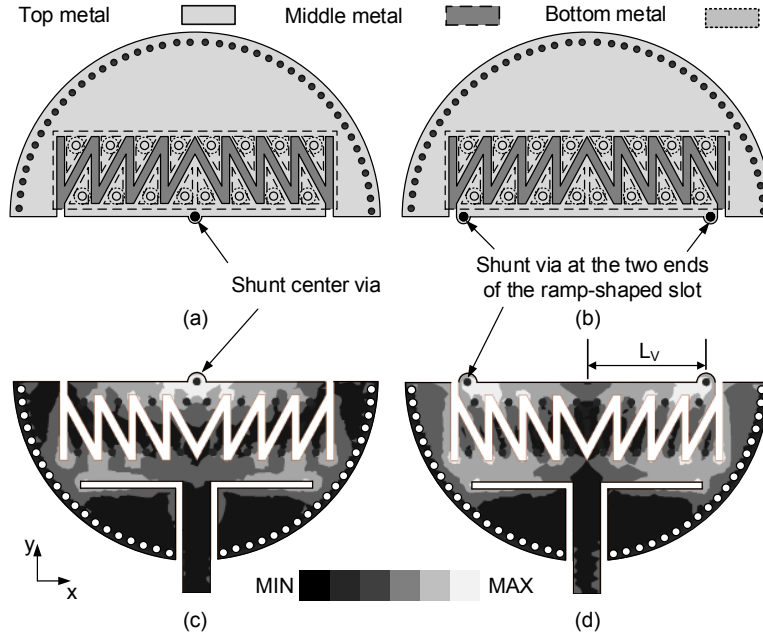


Figure 2.6: (a) Original HMSIW resonator, (b) Modified HMSIW resonator, (c), and (d) Magnitude of magnetic field distribution inside the original and modified HMSIW resonators, respectively .

to achieve positive coupling, the modified HMSIW resonator enables negative coupling. This is very useful in filter design process, where cross-coupling between the resonators is needed.

The magnitude of H-field distribution is plotted for the two resonators in Fig. 2.6(c), (d). For the original HMSIW resonator, the magnetic field is maximum at the center and around the shunt via, while the E-field is maximum around the capacitive elements (Fig. 2.6(c)). As a result, by changing the shunt via position, the maximum of the magnetic field happens at the two ends of the ramp-shaped slot instead of the center of the cavity (Fig. 2.6(d)). By controlling the position of the magnetic field concentration, it is possible to couple the resonators either positively or negatively (Section III). However, changing the center via position slightly lowers miniaturization factor for the modified HMSIW res-

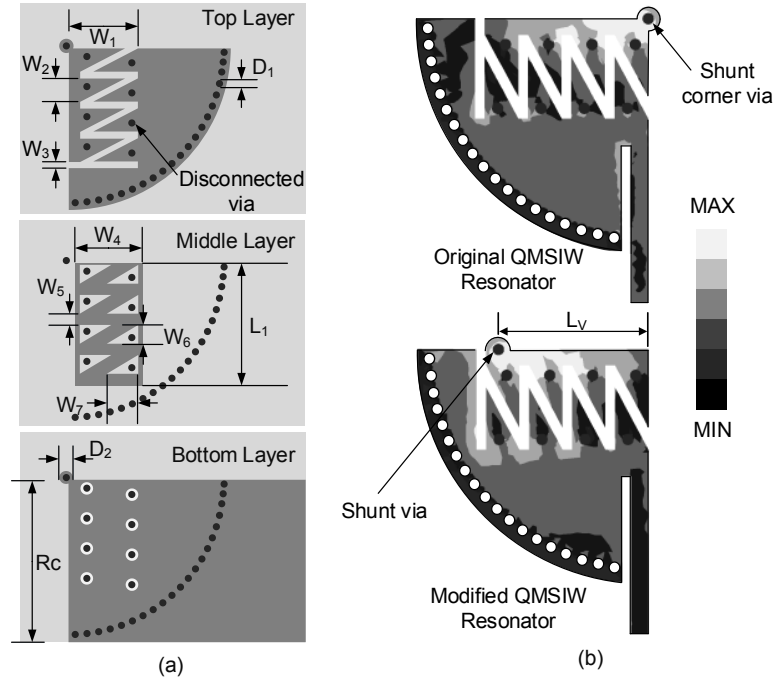


Figure 2.7: (a) Ultra miniature QMSIW resonator, (b) Magnitude of magnetic field distribution inside the original and modified QMSIW resonators.

onator. Considering $L_v = 11.75mm$, the miniaturization factor for the modified HMSIW resonator is $\sim 90\%$, while for the original HMSIW resonator, it is $\sim 92\%$.

2.2.2.2 Loss

The loss mechanism of the two HMSIW resonators is investigated by calculating the Q_U value based on the same approach described in the previous subsection. Using same substrate layers as before, Q_U values of 216, and 221 are achieved for the original and modified HMSIW resonators, respectively. The Q degradation is mainly contributed to the leakage loss from the open wall of the cavity, even though, the conductor loss would be less for HMSIW resonators compared to their SIW counterparts.

Table 2.2: Final Dimensions (mm) of the Ultra-miniature QMSIW Filter

W_1	6.25	W_2	2.6	W_3	0.75
W_4	7.5	W_5	1.5	W_6	2.1
W_7	3.5	D_1	0.9	D_2	1.7
L_V	11.75	L_1	13.7	R_c	18

2.2.3 Quarter-Mode SIW Resonator

QMSIW resonator can be obtained by bisecting the HMSIW resonator on its fictitious magnetic wall [34]. The overall size of the QMSIW resonator is roughly 25% of its SIW counterpart [35]. Again, inserting all the above miniaturization elements inside the QMSIW resonator forces the structure to resonate at -1^{st} resonance mode. Therefore, an ultra miniature resonator can be achieved which has approximately the same resonance frequency as Res. V (Fig. 2.1(e)), while its size is reduced by 75% [11].

Fig. 2.7(a) shows the top, middle, and bottom metal layers of the final ultra miniature QMSIW resonator. The shunt center via used in the SIW resonators is now placed on the corner of the resonator, and the ramp-shaped interdigital slot, and the floating patch are precisely quarter of their SIW version counterparts.

2.2.3.1 Effect of the Corner Via Position

Similar to the HMSIW resonator presented in the previous subsection, it is possible to control the magnetic field concentration inside the cavity to some degree by modifying the location of the shunt corner via. The magnitude of H-field distribution is shown in Fig. 2.7(b) for two QMSIW resonators. As can be seen, the magnetic field is concentrated around the corner via. By placing the shunt via on the other end of the ramp-shaped slot, the concentration of the H-field is modified. Again, altering the shunt via position results in slightly lower miniaturization factors. The dimensions of the final resonator are tabulated in Table 2.2. Based on these dimensions, and using same dielectric layers, the

–1st resonance happens at 731 MHz. Compared to a full mode SIW resonator with a fundamental mode at 731 MHz, roughly 95% miniaturization is achieved for the original QMSIW resonator in Fig. 2.7(a) [11]. However, considering $L_v = 11.75mm$, the miniaturization factor for the modified QMSIW resonator is $\sim 93\%$.

2.2.3.2 Loss

The loss mechanism of this resonator is studied based on the same approach used for the SIW, and HMSIW resonators. The Q_U values are 186, and 189 at 731 MHz for the original and modified QMSIW resonators, respectively. Although the conductor loss would be less than the SIW, and HMSIW versions of the resonator, because of two open walls of the cavity the Q_U values are degraded. Ultra compact size, relatively high Q, and capability of cross coupling of this resonator make it a suitable candidate for ultra miniature filter design.

2.3 Filter Design and Implementation

The ultra miniature HMSIW, and QMSIW resonators, introduced in the previous section, are used to design and fabricate a two-pole bandpass filter, and two trisection filters with transmission zeros on either side of the passband. First, the design values of the low-pass prototype response is determined for each filter based on the target specifications. Afterwards, the required coupling coefficient matrices and external quality factors (Q_e) are calculated for each filter based on the design values achieved in the first step. Since the method is based on the coupled-resonators filter design, the next step is to establish the relationship between the coupling coefficient matrix and the physical dimensions of the coupled resonators. The coupling factor for synchronously tuned coupled resonators can be approximated using, [45]

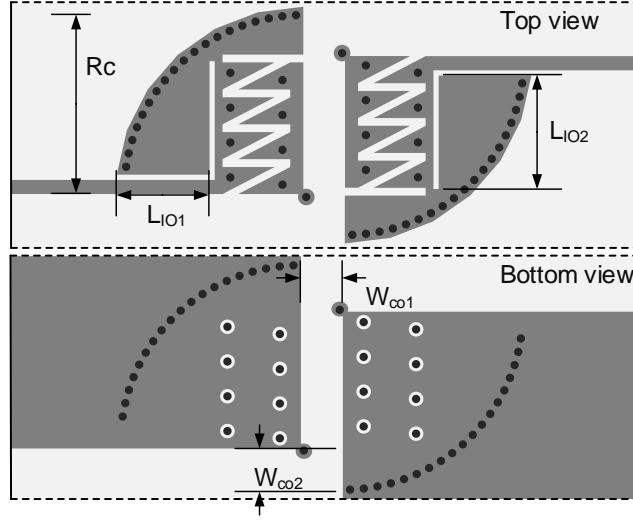


Figure 2.8: Top and bottom views of the miniaturized two-pole QMSIW filter. The parameter values are: $W_{CO1} = 4$ mm, $W_{CO2} = 4.4$ mm, $L_{IO1} = 8.9$ mm, $L_{IO2} = 10.9$ mm, and $R_C = 18$ mm.

$$k = \pm \frac{f_{p2}^2 - f_{p1}^2}{f_{p2}^2 + f_{p1}^2}, \quad (2.3)$$

where, f_{p2} , and f_{p1} are the two split resonance frequencies extracted from full-wave simulation of the coupled resonators with weakly-coupled input/output ports. The positive or negative sign of the coupling factor determines whether the resonators are positively or negatively coupled, respectively. The Q_e value is extracted from full-wave simulation of the singly loaded resonator using, [45]

$$Q_e = \frac{f_0}{\Delta f_{\pm 90^\circ}}, \quad (2.4)$$

where, f_0 is the simulated resonance frequency and the $\Delta f_{\pm 90^\circ}$ is the difference of the frequencies at which a phase shift of $\pm 90^\circ$ occurs in the S_{11} phase response of the resonator.

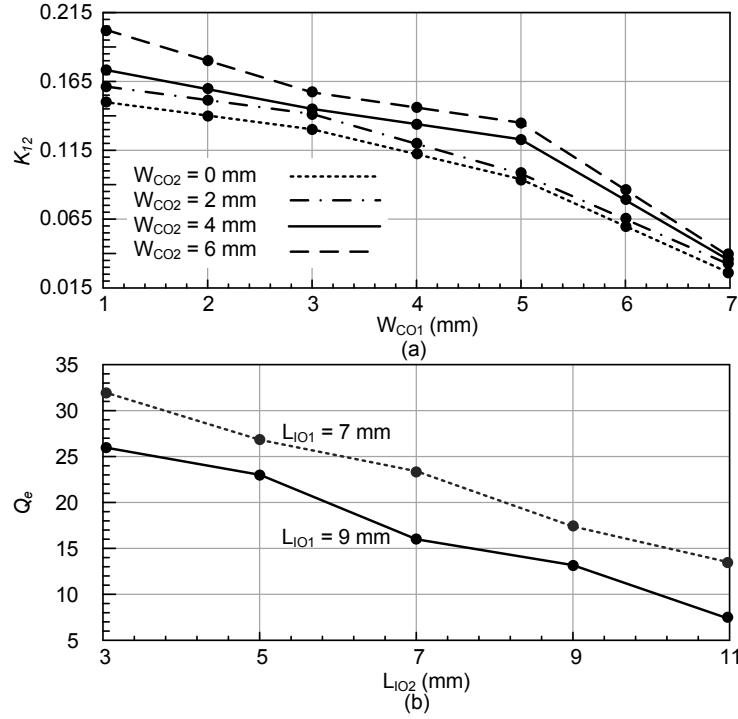


Figure 2.9: (a) The coupling factor of the two-pole filter as a function of the spacing between the resonators, (b) the Q_e values as a function of the L-shaped slot length.

2.3.1 Two-pole bandpass filter

Fig. 2.8 shows the top, and bottom views of the two-pole bandpass filter using the proposed QMSIW resonator implemented with two Rogers RT/Duroid 6010LM substrates that are bonded together with Rogers RO4450B pre-preg material as described before [11]. The two-pole coupled-resonator filter is designed to operate at center frequency of 700 MHz. For an in-band return loss better than 20 dB with pass-band ripple of 0.01 dB, and 3-dB bandwidth (FBW) of 6%, using the designed values of the low-pass Chebyshev prototype response, the required coupling factor is $k_{12} = 0.14$, and the external quality factor is $Q_e = 7.4$.

While the spacing between the two resonators (W_{CO1} , and W_{CO2}) is used to obtain the proper coupling, the L-shaped slot (L_{IO1} , and L_{IO2}) is used at the input/output to adjust

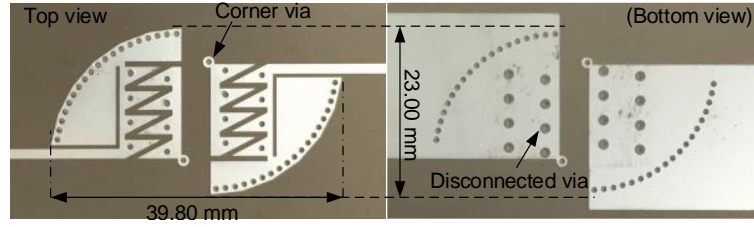


Figure 2.10: Top (left), and bottom (right) views of the two-pole filter prototype.

the required external quality factor. To better show the relationship between the physical dimensions and the required theoretical design values, the coupling factor as a function of the spacing between the resonators, and the Q_e value as a function of the L-shaped slot length is plotted in Fig. 2.9(a), and (b), respectively. The horizontal distance between the two resonators, W_{CO1} , can be used for coarse adjustment of the coupling factor. However, the vertical distance, W_{CO2} , can be utilized for fine tuning. As shown in Fig. 2.7(b), the H-field distribution inside the original QMSIW cavities are maximized around the shunt corner via. As W_{CO1} decreases, and W_{CO2} increases, the two shunt corner vias will become closer to each other, and as a result, higher coupling factors are achievable ($W_{CO1} = 4$ mm, and $W_{CO2} = 4.4$ mm for $k_{12} = 0.14$). For the external quality factor, the total length of the L-shaped slot needs to be adjusted accurately. In this design, Q_e value becomes close to 7.4 when L_{IO1} is 9 mm, and L_{IO2} is 11 mm.

Fig. 2.10 shows the top and bottom views of the fabricated prototype. First, the top and bottom metal walls are etched on the upper metalization side of the top substrate, and lower metalization side of the bottom substrate, respectively. Afterwards, the bottom-side metalization of the top substrate is completely removed, while the top-side metalization of the bottom substrate is etched to create the floating patch. The two substrate layers are then bonded to each other using Rogers pre-preg material, and finally, the plated via holes are drilled through both substrates [11]. The overall size of the presented QMSIW two-pole

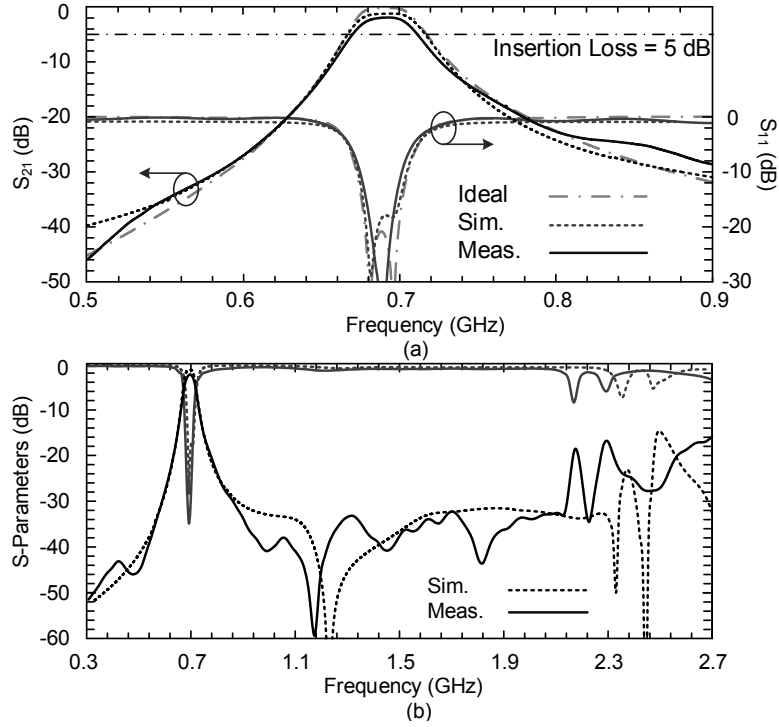


Figure 2.11: (a) Ideal, simulated, and measured narrow-band responses of the two-pole filter, (b) measured and simulated wide-band filter responses.

filter, excluding the microstrip feed lines, is $0.05\lambda_0 \times 0.09\lambda_0$, where λ_0 is the wavelength in free space at the frequency of operation.

Fig. 2.11(a) shows the measured and simulated narrow-band s-parameters responses of the proposed filter [11]. Also, the ideal synthesized response of the standard two-pole Chebyshev prototype is plotted for $k_{12} = 0.14$, and $Q_e = 7.4$ [45]. As can be seen, good agreement between the theory, simulation, and measurement results is achieved. The return loss is better than 30 dB, while the measured in-band insertion loss is ~ 2.1 dB. The measured 3-dB fractional bandwidth is 5.9%, which is almost the same as the designed value. The measured and simulated wide-band s-parameters response of the filter are shown in Fig. 2.11(b). Since the -1^{st} resonance mode of the QMSIW resonators is used to design the two-pole filter, there is a transmission zero occurred around the 0^{th}

order resonance mode. Therefore, the first spurious harmonic does not appear up to the 1st resonance mode of the QMSIW resonators. This provides an out-of-band rejection better than 30 dB up to 2.1 GHz, which is almost three times the center frequency of the operating band. To the best of author's knowledge, this is the most compact two-pole SIW-based bandpass filter, which also has improved upper stopband rejection.

2.3.2 Trisection filters

In some applications high selectivity is required on solely one side of the passband [45]. Hence, for asymmetric bandpass filter response with minimum possible insertion loss, trisection filters can be used, which are capable of having transmission zero on either side of the passband that high selectivity is required [46]. The transfer function of a trisection filter can be expressed as [45],

$$|S_{21}| = \frac{1}{\sqrt{1 + \epsilon^2 \cdot F_n^2(\Omega)}}, \quad (2.5)$$

$$F_n = \cosh\left(\sum_{i=1}^{i=n=3} \cosh^{-1}\left(\frac{\Omega - \frac{1}{\Omega_{TZ,i}}}{1 - \frac{\Omega}{\Omega_{TZ,i}}}\right)\right), \quad (2.6)$$

where ϵ is the ripple constant, Ω is the frequency variable of the lowpass prototype filter, $\Omega_{TZ,i}$ is the i^{th} transmission zero, and $n = 3$ is the degree of the filter. It is noteworthy that since there is only one finite transmission zero in one-unit trisection filter, the other two will be placed at infinity in the Ω domain.

2.3.2.1 Filter Synthesis

Fig. 2.12 shows two general topologies for one-unit trisection filter. Both are three-pole arrangements with cross-coupling between the first and the third resonators. Positive (dashed line) and negative (solid line) cross couplings are used in Trisection I, and II topologies, respectively. As a result, Trisection I topology has its transmission zero on

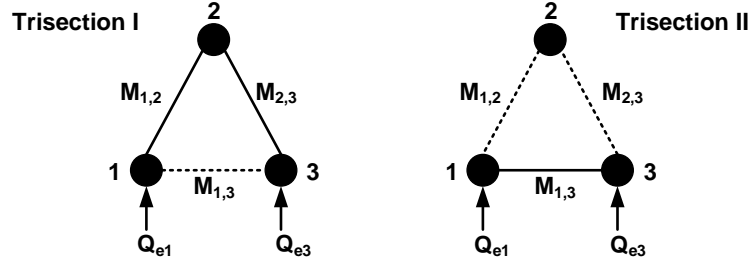


Figure 2.12: Two possible single-unit trisection topologies.

Table 2.3: Trisection Filters Specifications and Required Design Values

	Trisection I	Trisection II
Midband Frequency (MHz)	920	760
FBW (%)	4.4	4.4
In-band Return Loss (dB)	>20	>20
Out-of-Band Rejection >20 dB	$f \leq 890$ MHz	$f \geq 790$ MHz
$f_{01} = f_{03}$	925.4 MHz	755.04 MHz
f_{02}	910.05 MHz	768.3 MHz
$Q_{e1} = Q_{e3}$	15.7	15.8
$M_{12} = M_{23}$	-0.0426	0.0423
M_{13}	0.036	-0.034

the lower side of the passband, while for Trisection II, the transmission zero appears on the upper side of the passband. Although, the response of the trisection filter is basically asymmetrical, it is possible to keep the physical configuration of the filter symmetrical [45]. Therefore, for each topology in this design, the two coupling factors $M_{1,2}$, and $M_{2,3}$, and also, the two external quality factors Q_{e1} , and Q_{e3} are equal, respectively.

Trisection I, and II filters are designed to operate at midband frequencies of 920 MHz, and 760 MHz, with out-of-band rejection > 20 dB for frequencies ≤ 890 MHz, and ≥ 790 MHz, respectively. For both filters, the 3-dB fractional bandwidth is considered 4.4%, while the in-band return loss is better than 20 dB. Based on these specifications, the element values of the low pass prototype filters are first calculated based on the approach discussed in [45]. Afterwards, the required resonance frequency of each resonator (f_{01} ,

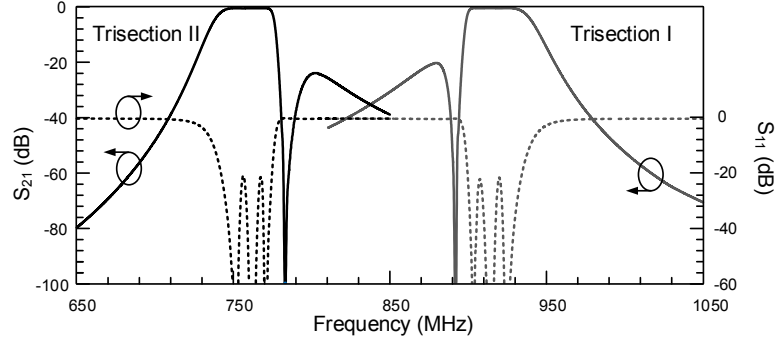


Figure 2.13: Synthesized responses of the two trisection filters.

f_{02} , f_{03}), the external quality factors, and the coupling matrix elements are extracted for both filters. The specifications and the required theoretical design values of both filters are summarized in Table 2.3. For the Trisection I case, $f_{01} = f_{03}$ is higher, and f_{02} is lower than the filter's midband frequency (f_m). For the Trisection II filter, however, $f_{01} = f_{03}$ is lower than its f_m , while f_{02} is higher. The general coupling matrix for both Trisection filters, m_I , and m_{II} , are calculated based on the required specifications summarized in Table 2.3,

$$m_I = \begin{bmatrix} 0.25 & -0.96 & 0.81 \\ -0.96 & -0.65 & -0.96 \\ 0.81 & -0.96 & 0.25 \end{bmatrix}, \quad m_{II} = \begin{bmatrix} -0.17 & 0.95 & -0.79 \\ 0.95 & 0.68 & 0.95 \\ -0.79 & 0.95 & -0.17 \end{bmatrix}.$$

The two matrixes have close values, while the signs are reverse. This will guarantee mirrored frequency responses for the two filters compared to each other [46]. Using m_I , and m_{II} , the synthesized responses of two ideal trisection filters are shown in Fig. 2.13. The lumped-element equivalent circuits of the trisection filters are comprehensively discussed in [45], and the precise value of each lumped element can be extracted using m_I , and m_{II} . Based on the presented ultra-compact QMSIW, and HMSIW resonators, two trisection filters are designed and implemented.

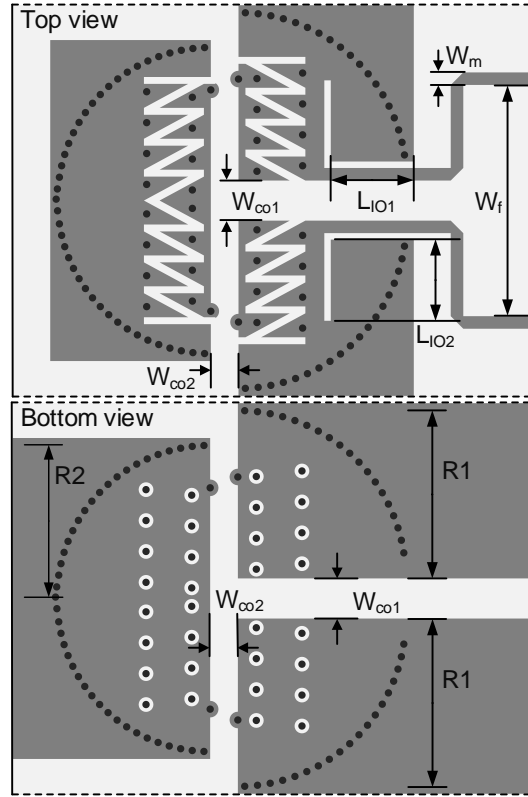


Figure 2.14: Top and bottom views of the designed Trisection I filter with a controllable transmission zero on lower side of the passband ($R1 = 19$ mm, $R2 = 17.4$ mm, $W_{CO1} = 4.35$ mm, $W_{CO2} = 3$ mm, $L_{IO1} = 7$ mm, $L_{IO2} = 9.5$ mm, $W_m = 1.36$ mm, and $W_f = 25.07$ mm).

2.3.2.2 Filter Design

Fig. 2.14, and 2.15 show the top and bottom views of the two designed trisection filters. The two QMSIW resonators are the first and the third resonators of the topologies shown in Fig. 2.12, while the HMSIW resonator acts as the second resonator. For simplicity, the required resonance frequencies, f_{01} , f_{02} , and f_{03} , are adjusted by finely tuning the radius of the cavities ($R1$, and $R2$), while miniaturization parameters are kept the same as tabulated in Table 2.2. The two structures are excited using microstrip feed lines. However, to make enough room for SMA connectors, the distance between the input/output ports is increased

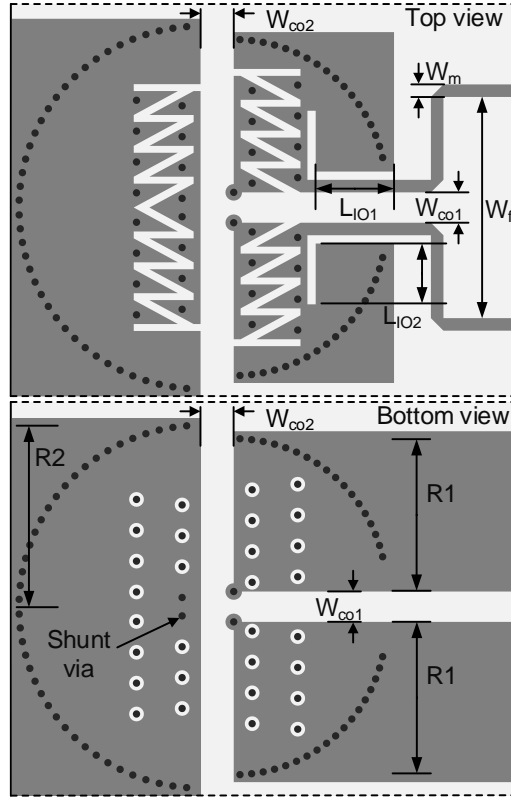


Figure 2.15: Top and bottom views of the designed Trisection II filter with a controllable transmission zero on higher side of the passband ($R1 = 17.4$ mm, $R2 = 20$ mm, $W_{CO1} = 3.3$ mm, $W_{CO2} = 3.6$ mm, $L_{IO1} = 9$ mm, $L_{IO2} = 7.5$ mm, $W_m = 1.36$ mm, and $W_f = 25.07$ mm).

to W_f value by using additional microstrip lines. Similar to the two-pole filter and based on Fig. 2.9(b), the length of the L-shaped slots (L_{IO1} , L_{IO2}) at the input/output ports are adjusted to achieve the required Q_e value.

As was shown in Fig. 2.6, and 2.7, it is possible to control the location of the maximum H-field distribution inside the cavities by changing the shunt corner via position. As a result, either positive or negative couplings can be achieved based on adjusting the location of the shunt via. When the two shunt vias of the two QMSIW resonators are close enough to each other, the concentration of the maximum of H-field distribution of the two resonators

are in close proximity, and as a result, negative coupling can be achieved between the two resonators. However, by placing the shunt vias far from each other ($L_V = 11.75mm$), the concentration of maximum H-field distribution of the two cavities are far enough to make positive coupling between the two QMSIW resonators possible. In Trisection I configuration (Fig. 2.14), the two QMSIW resonators are coupled to the HMSIW resonator negatively from the open-wall of the cavities where the shunt vias are placed. However, they are coupled to each other positively from their other open-wall where there are no shunt vias. On the other hand, for Trisection II configuration shown in Fig. 2.15, the two QMSIW resonators are coupled to each other negatively as their shunt vias are placed in the corner, and in close proximity to each other. However, the shunt vias of the HMSIW resonator are removed from its open edge, and instead, two of the previously disconnected vias are now connected to act as center shunt vias (Fig. 2.15). This way the undesired negative coupling between the HMSIW and QMSIW resonators is minimized, and the two QMSIW resonators are coupled positively to the HMSIW resonator from its open wall.

The distance between the resonators (W_{co1} , and W_{co2}) is used to adjust the required coupling values. In order to better show the cross-coupling behavior, each two resonators are weakly coupled at the input/output ports and simulated separately. Fig. 2.16 shows the relationship between the physical dimensions (W_{co1} , and W_{co2}), and the coupling matrix elements (M_{12} , M_{23} , and M_{13}) for both trisection filters. For Trisection I topology, by increasing W_{co2} , lower coupling coefficient values are achievable between the QMSIW and the HMSIW resonators. However, increasing W_{co1} results in higher coupling coefficient values between the two QMSIW resonators in this filter. This is an evidence that the two coupling coefficients are out of phase [47]. Inversely, for Trisection II topology, increasing W_{co1} results in lower coupling coefficients, while for larger W_{co2} values, higher coupling factors are achievable. The final dimensions of the proposed filters are summarized in the caption of Fig. 2.14, and 2.15.

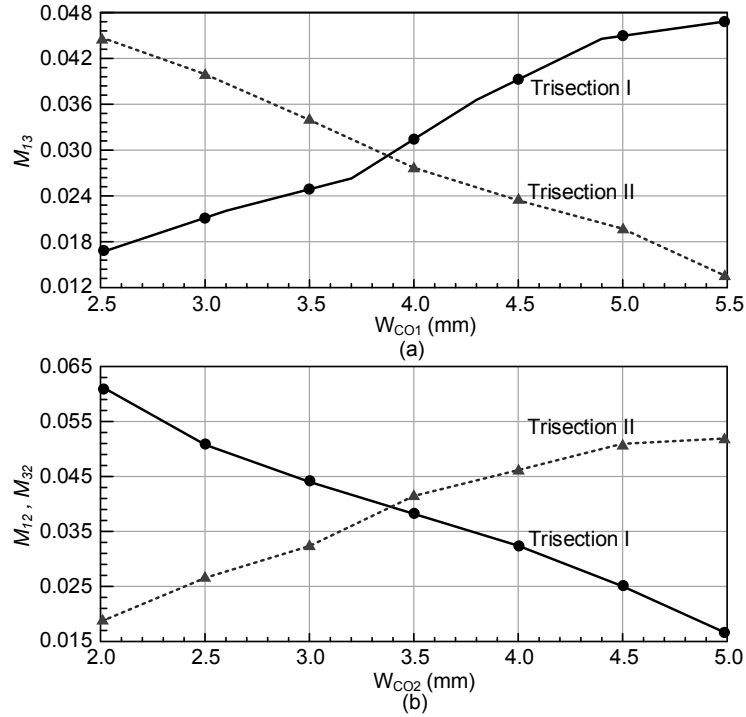


Figure 2.16: The inter-resonator coupling factors of the two trisection filters as a function of the spacing between the resonators.

2.3.2.3 Fabrication and Experimental Results

Fig. 2.17(a), (b) show the top and bottom views of the two fabricated trisection filters, respectively. The fabrication process is same as the two pole filter. The overall size of Trisection I prototype (Fig. 2.17(a)), excluding the microstrip feed lines, is $39.4 \text{ mm} \times 42.3 \text{ mm}$, which is equivalent to $0.101\lambda_0 \times 0.109\lambda_0$. Similarly, the size of Trisection II prototype is $41 \text{ mm} \times 41.5 \text{ mm}$, which is equal to $0.12\lambda_0 \times 0.12\lambda_0$.

The fabricated prototypes are measured using a two-port network analyzer (Agilent N5230A) after short-open-load-thru (SLOT) calibration. Fig. 2.18(a), and (b) show the simulated and measured narrow-band s-parameter responses of the two trisection filters, which are in reasonably good agreement with the ideal responses of the two filters shown in Fig. 2.13. The measured in-band return loss is better than $\sim 17 \text{ dB}$ for both filters, while

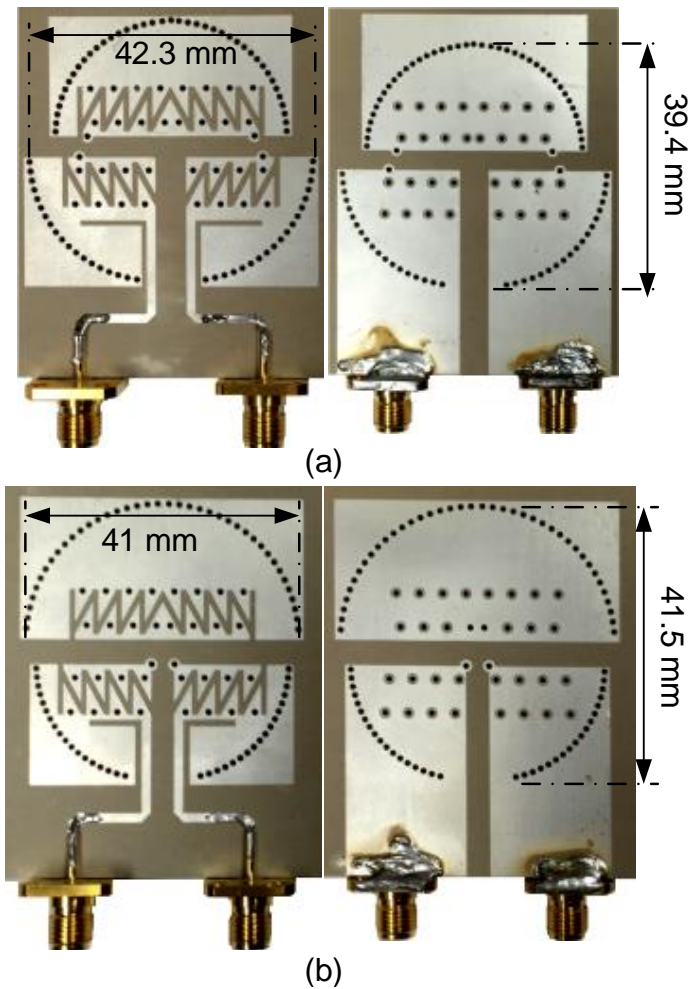


Figure 2.17: Top (left) and bottom (right) views of fabricated, (a) Trisection I, and (b) Trisection II prototypes.

the insertion loss is 2.45 dB, and 2.1 dB for Trisection I, and II filters, respectively. The midband frequencies are 912 MHz for Trisection I, and 754 MHz for Trisection II, while the FBW is $\sim 4.2\%$ for both prototypes, which is very close to the designed value.

Fig. 2.19(a), (b) show the simulated and measured wide-band response of the two filters, respectively. Similar to the two pole filter, and as the -1^{st} resonance frequency is excited to design an ultra compact filter, a transmission zero occurs around the 0^{th} resonance mode for both filters. Hence, a rejection level of > 19 dB is achieved in the frequency

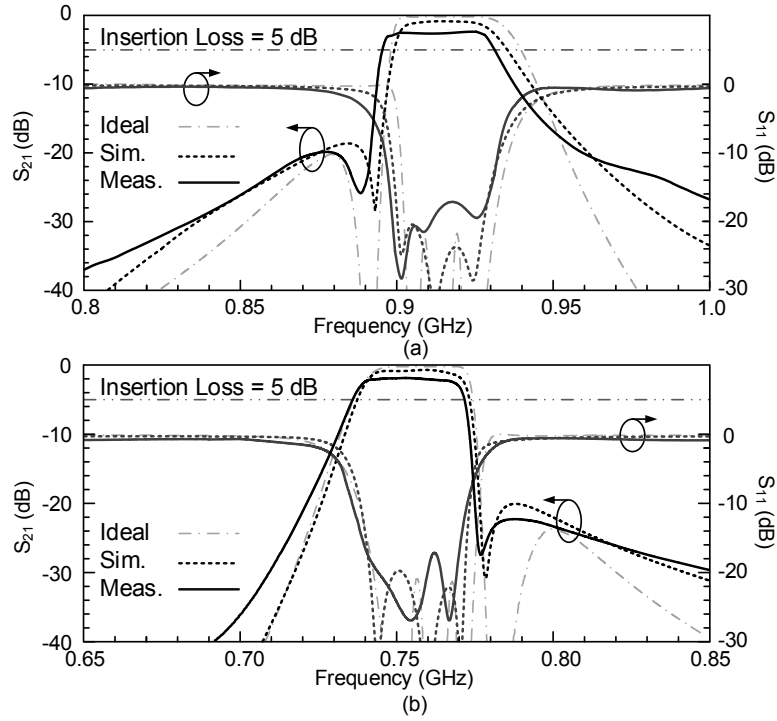


Figure 2.18: Measured and simulated narrow-band filter responses of, (a) Trisection I prototype, and (b) Trisection II prototype.

range of 0.965-2 GHz, and 0.8-1.5 GHz for Trisection I, and II filters, respectively.

2.4 Discussion

As can be seen in Fig. 2.11(a), and 2.18, the measured and simulated results of the proposed prototypes are relatively in good agreement. The frequency-shift error is less than 1.5%, which probably comes mainly from the dielectric constant tolerances. For the Rogers 6010 dielectric material, the reported tolerance of ϵ_r value is $\sim 2.45\%$ over 10.2 from the datasheet³. Moreover, slight discrepancy in insertion loss between the measurement and simulation results corresponds to the effect of practical errors such as variations in via diameter, or soldering and SMA connector's loss, which were not considered in simulations. The quality factor error between the measured and simulated results of the

³RT/duroid 6010LM data sheet. [online]. www.rogerscorp.com

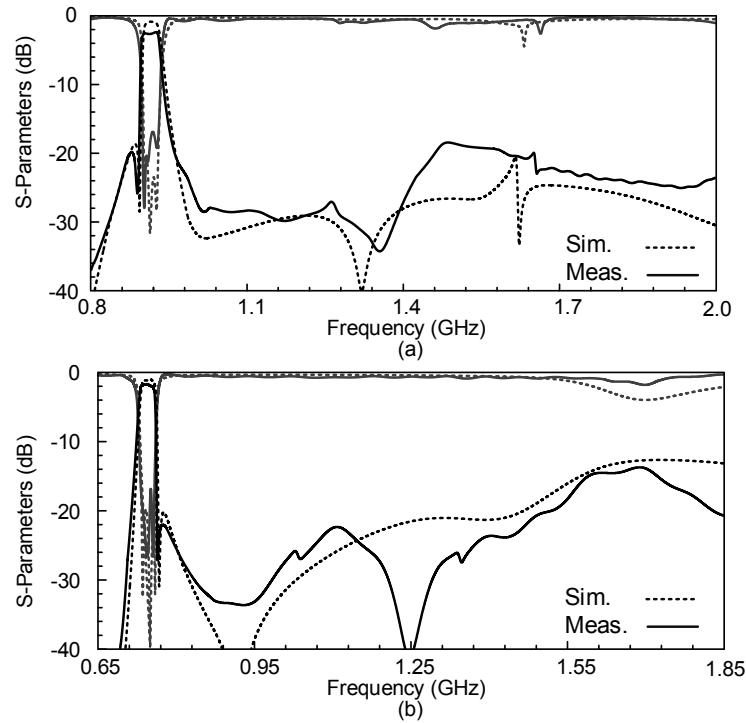


Figure 2.19: Measured and simulated wide-band filter responses of, (a) Trisection I prototype, and (b) Trisection II prototype.

proposed filters is less than $\sim 6\%$.

Table 2.4 compares the measured performance characteristics of the proposed two-pole and trisection filters with the previously presented works in literature. In order to perform a fair size comparison, filter sizes are computed relative to the air-wavelength at the center operating frequency for each filter. As can be seen, the proposed method achieves the highest miniaturization factor, while it meets similar or better performance specifications.

Table 2.4: Comparison of Related Works in Literature

	Filter Type	Operating Center Frequency (GHz)	BW (%)	Insertion Loss (dB)	Return Loss (dB)	Size
[32]	CSRR-loaded SIW three-pole filter	5.05	6.53	2.03	16.6	$\sim 0.2\lambda_0 \times 0.4\lambda_0$
[33]	IDC-loaded SIW cavity two-pole filter	6.11	6.54	1.59	17.2	$\sim 0.23\lambda_0 \times 0.46\lambda_0$
[34]	QMSIW cavity four-pole filter	5.85	14	2	13	$\sim 0.36\lambda_0 \times 0.37\lambda_0$
[37]	SIW cavity trisection filter (upper-side high selectivity)	4.85	~ 4	3	17.8	$\sim 0.73\lambda_0 \times 1.39\lambda_0$
[40]	two ring-gap loaded SIW cavity trisection filters (diplexer design)	9.5 / 10.5	4.2 / 3.8	1.6 / 2.1	10 / 16	$\sim 0.58\lambda_0 \times 0.61\lambda_0 /$ $\sim 0.57\lambda_0 \times 0.6\lambda_0$
This Work I	Ultra-miniature QMSIW cavity two-pole filter	0.690	5.9	2.1	30	$\sim 0.05\lambda_0 \times 0.09\lambda_0$
This Work II	two ultra-miniature HM/QM-SIW trisection filters	0.912 / 0.754	~ 4.2	2.45 / 2.1	17 / 17	$\sim 0.101\lambda_0 \times 0.109\lambda_0 /$ $\sim 0.12\lambda_0 \times 0.12\lambda_0$

3. MINIATURIZED SUBSTRATE INTEGRATED WAVEGUIDE CAVITY BACKED SLOT ANTENNAS

3.1 Introduction

Cavity-backed slot antennas (CBSAs) have been tremendously used in various wireless communication systems due to their relatively high gain, and one-sided radiation patterns. However, large size, and bulky structure of conventional CBSAs prevent the use of such antennas in integrated and miniaturized modern wireless systems. Therefore, specific miniaturization techniques need to be employed to creatively reduce the size, and improve the integrability, while maintaining the high performance characteristics.

One technique to reduce the size of the cavity of a conventional CBSA is presented in [48], where the solid metal around the traditional slot antenna is replaced with meandered metallic strips that can effectively support the required surface current on the ground metal plane. Using this method, the width of the cavity is reduced, however; the length of the radiating slot and the cavity remain the same. Moreover, the integrability of this antenna in a planar system is hindered due to use of a bulky conventional cavity. A remedy to this issue is presented in [43, 49, 50], where the host cavity is implemented based on substrate integrated waveguide (SIW) structure. Low profile, planar structure, and relatively high isolation of SIW cavities make them a good candidate for CBSAs. However, such structures still require miniaturization.

Size reduction of the SIW CBSA is achieved in [51], based on exciting the negative-order resonance of the cavity. By replacing the radiating slot with an inter-digital capacitor (IDC), a composite right/left-handed (CRLH) resonator is formed which is capable of radiation at the -1^{st} resonance frequency. By effectively lowering the operating frequency

©2016 IEEE. Part of this chapter is reprinted, with permission from IEEE, "An Ultra-Miniature SIW Cavity-Backed Slot Antenna," IEEE Antennas and Wireless Propagation Letters, Jun. 2016.

of the antenna, miniaturization is achieved. However, the miniaturization factor based on this method is also limited due to the available area on the top metal plane of the cavity, and the geometrical dimensions of the employed metamaterial-inspired loading structures.

In this section, an ultra-miniature SIW CBSA based on employing negative-order resonance mode in a compact SIW cavity resonator. First, a compact SIW cavity is achieved by using non-radiating ramp-shaped metallic strips that can effectively support the required surface current. Afterwards, radiating ramp-shaped slot is employed to force the structure to operate at its negative first-order resonance. Finally, a floating metal patch is inserted in an additional middle metal layer to increase the capacitive loading effect beyond the limits defined by the size of the planar slots (IDC), and achieve further miniaturization. The measured results of the proposed antenna show a return loss of ~ 20 dB, with a maximum gain of 3.6 dBi, and radiation efficiency of $\sim 80\%$. A miniaturization factor of $\sim 87\%$ is achieved for the first time compared to a conventional SIW CBSA with the same operating frequency.

3.2 Ultra-Miniature CBSA

3.2.1 Miniaturization Procedure

Fig. 3.1 demonstrates the procedure used to achieve the ultra miniature SIW CBSA. First, the dimensions of a conventional SIW cavity is determined based on operating at its fundamental mode (see Fig. 3.1(a)). The length of the cavity needs to be $\lambda_c/2$ at the operational frequency to have an efficient radiation, where λ_c is the wavelength in free space divided by square root of the dielectric constant of the cavity material. Moreover, the length of the radiative slot is roughly $\lambda_g/2$, where λ_g is the guided wavelength along the slot, and is basically different from λ_c .

The electric current flow on the ground metal plane of a conventional CBSA has two components. One is parallel to the slot line, which is creating a resonant condition, while

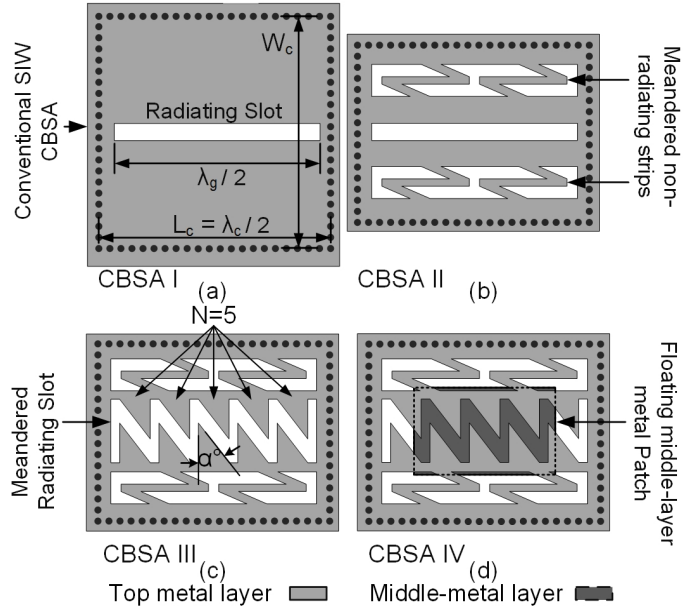


Figure 3.1: (a) Conventional SIW CBSA, (b) reduced-size CBSA using meandered non-radiating metallic strips, (c) CRLH-based CBSA operating at the -1 resonance frequency, and (d) final ultra-miniature SIW CBSA using a floating metal patch in an additional middle metal-layer.

the other is perpendicular to the slot line, and responsible for far-field radiation. It is shown in [48] that the uniform metallic plane around the radiative slot can be replaced by meandered metallic strips that have similar effective length and are capable of supporting the normal component of the electric current (see Fig. 3.1(b)). It is worth-mentioning that the antenna gain, radiation efficiency (η_{rad}), and bandwidth are directly affected by the number of metallic strips, while the front-to-back ratio (FTBR) is not significantly sensitive to this parameter [48]. Two ramp-shaped meandered strips are used at the two sides of the radiative slot to achieve same electrical length in a more compact fashion. This way W_c is reduced, however, L_c remains the same.

In order to achieve further miniaturization, the conventional radiative rectangular slot is replaced with a ramp-shaped interdigital slot (see Fig. 3.1(c)). This meandered slot acts as

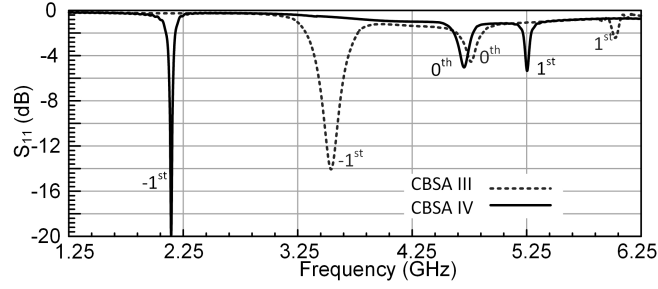


Figure 3.2: Simulated S_{11} results of CBSA III, and CBSA IV.

an equivalent series capacitor, and introduces effective negative permeability. The via wall of the SIW cavity can be considered as equivalent shunt inductors, and introduces effective negative permittivity. As a result, a CRLH resonator is achieved, which is capable of radiation in its -1^{st} resonance [51]. The equivalent series capacitance, added by the ramp-shaped slot, is mainly a function of the number of fingers (N), and the angle between the adjacent slots (α) [12, 36]. In this case, the size of the structure remains the same, but the operating frequency is lowered to the -1^{st} resonance. This is equivalent to miniaturization of the length of the radiative slot, and the cavity.

As the equivalent series capacitance introduced by the ramp-shaped slot increases, the -1^{st} resonance occurs at a lower frequency, and higher miniaturization can be achieved. However, as can be seen in Fig. 3.1(c), the size of the ramp-shaped slot cannot be increased more than a certain value due to lack of enough space on the top metal wall of the cavity. Therefore, to achieve higher miniaturization, a floating metal patch is added in an additional middle metal layer, and beneath the ramp-shaped slot. The patch increases the effective series capacitance of the whole resonator, and results in even a lower -1^{st} resonance frequency. This is shown in Fig. 3.2, where the simulated S_{11} results of CBSA III, and CBSA IV are plotted. As can be seen, both the $\pm 1^{st}$ resonances (odd modes) shift down to lower values, while the 0^{th} resonance mode remains roughly the same. For CBSA

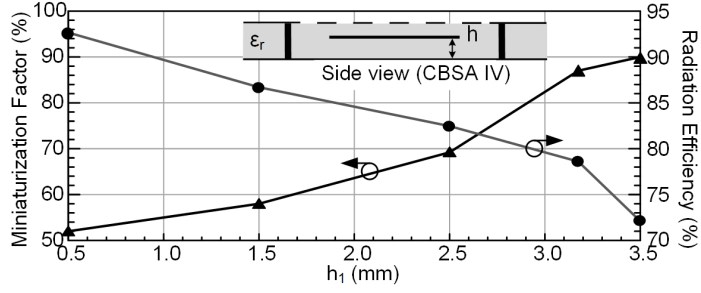


Figure 3.3: The Effect of h_1 on the miniaturization factor and radiation efficiency of CBSA IV, and the side view of the CBSA IV.

IV, the operating frequency is mainly sensitive to the height of the patch. This is shown in Fig. 3.3, where the miniaturization factor (MF) and the radiation efficiency of CBSA IV are plotted for various values of h_1 (height of the floating patch from the bottom metal layer). In this plot, the MF of the miniaturized antenna operating at a lowered frequency of f_0 is computed using

$$MF\% = \frac{A_{CBSA,f_0} - A_m}{A_{CBSA,f_0}} \times 100 \quad (3.1)$$

where A_{CBSA,f_0} is the area of a conventional SIW CBSA, which radiates at f_0 , and A_m is the area of the proposed CBSA IV. As the height increases, and the patch becomes closer to the ramp-shaped slot on the top metal wall, the frequency shifts down to lower values, and higher miniaturization factors are achieved. Moreover, due to this further size reduction, the FTBR drops, and as a result, the radiation efficiency decreases. The choice of h_1 is also limited due to the available standard substrate thicknesses, and fabrication constraints.

The four CBSAs shown in Fig. 3.1 are simulated in High Frequency Structure Simulator (HFSS), and the simulation performance characteristics are compared in Table 3.1. A MF of 87% is achieved for CBSA IV compared to a conventional SIW CBSA (CBSA

Table 3.1: Comparison of Different Miniaturized CBS Antennas

	MF	Gain (dBi)	η_{rad}	FTBR (dB)	BW
CBSA I	0%	5.35	91%	8.3	1.7%
CBSA II	42%	2.1	61%	7.5	1.5%
CBSA III	66%	3.5	83%	6.4	1.2%
CBSA IV	87%	3.66	81%	5.8	0.96%

I). Due to the significant reduction in the size of the antenna, the FTBR is reduced from 8.3 dB to 5.8 dB. The gain and the radiation efficiency of CBSA II is dropped, which is mainly due to low number of non-radiating meandered strips [48]. However, by reducing the length of the antenna based on utilizing the ramp-shaped slot, and the floating metal patch, the two meandered non-radiating strips can effectively support the normal component of the surface current flow, and as a result, both the gain and the radiation efficiency are improved for CBSA III, and IV compared to CBSA II. Moreover, as the four CBSAs are high- Q resonator-based antennas, by increasing the miniaturization factor, the Q of the resonator increases, and the bandwidth (BW) drops from 1.7% for CBSA I to $\sim 1\%$ for CBSA IV. This happens mainly because the electrical size of the antenna decreases and smaller electrical sizes mean lower radiation efficiency and more trapped waves inside the resonator, i.e. higher Q . The simulated surface current distribution on the top layer of CBSA IV is shown in Fig. 3.4 at $t = 0$, and $\tau/2$, where τ is the period of the current. The surface current is roughly zero at $t = \tau/4$, and $3\tau/4$. The dominant surface current direction depicted at $t = 0$, and $\tau/2$ shows 180° phase change in the half period. Therefore, the linear change of current in each period suggests linear polarization in the x - z plane for CBSA IV.

3.2.2 Antenna Topology

Fig. 3.5 shows the top, middle, and bottom layers of the implemented CBSA along with the A-A' cross section view of the structure. The substrates are both Rogers RT/Duroid 5880 ($\epsilon_r = 2.2$, $\tan\delta = 0.0004$) with different thicknesses of $h_1 = 3.2$ mm, and $h_2 = 0.5$

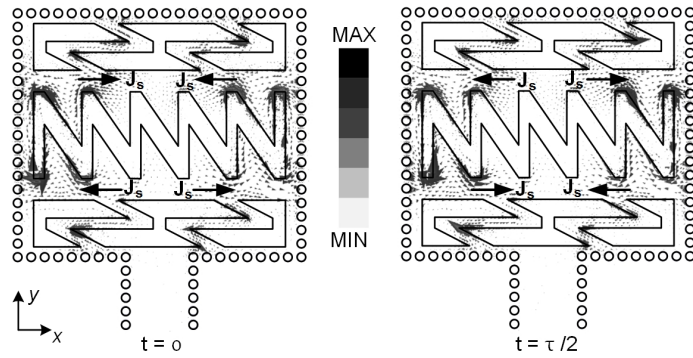


Figure 3.4: Simulated surface current distribution of CBSA IV at $t = 0, \tau/2$.

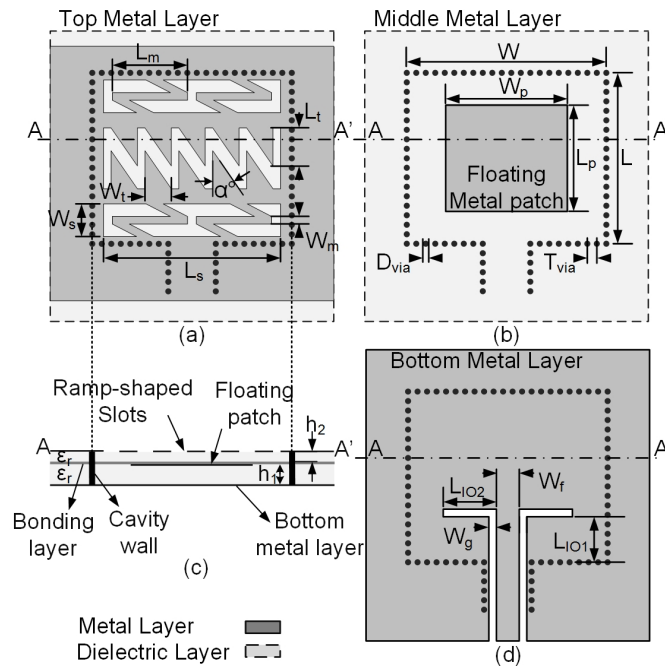


Figure 3.5: Antenna configuration, (a) top metal layer view. (b) middle metal layer view. (c) A-A' cross-section view, and (d) bottom metal layer view.

mm. The two substrate layers are bonded to each other using Rogers RO4450B pre-prep material ($\epsilon_r = 3.3, h = 0.09$ mm). The bonding layer is chosen thin enough to have negligible effect on the antenna performance characteristics, and also is considered in all the

full-wave simulations.

As the -1^{st} resonance frequency is excited, the operating frequency can be coarsely tuned by adjusting the number of fingers of the ramp-shaped interdigital slot. According to the available area on the cavity top metal-wall, $N = 5$, and $\alpha \simeq 35^\circ$ are chosen to achieve the highest possible miniaturization factor [12]. On the other hand, fine tuning of the -1^{st} resonance frequency can be achieved by changing each finger's dimension parameters (W_t , and L_t in Fig. 3.5).

Different techniques have been used in literature to excite a CBSA [43, 48]. One approach is to implement an open-circuited microstrip line in an additional layer on top of the radiating slot, and achieve the required impedance matching by adjusting the length and position of the microstrip line [48]. However, using this method to excite the proposed antenna is not recommended, as it adds another dielectric and metal layer to the structure. On the other hand, another method is to utilize a conductor-backed coplanar waveguide (CB-CPW) line to SIW cavity transition to excite both the cavity and the slot antenna as a single resonance structure [43, 51]. However, as can be seen in Fig. 3.5 (a), the top metal layer is fully utilized for different miniaturization elements, and there is not enough space for CB-CPW line transition to the SIW cavity.

As an alternative to the conventional methods of exciting CBSAs, folded CB-CPW line is implemented on the bottom metal-layer to excite the antenna, and achieve proper matching (see Fig. 3.5 (d)). As a result, the number of dielectric and metal layers remain the same, and there is no need to sacrifice any miniaturization elements on the top metal layer for feeding the structure. However, this approach can affect the FTBR, and dictates another trade-off. The main parameter for achieving the required impedance matching is the overall length of $L_{IO1} + L_{IO2}$, while the gap distance (W_g) should be adjusted for minimum leakage from the bottom wall of the cavity. The final dimensions of the proposed ultra-miniature CBSA are summarized in Table 3.2.

Table 3.2: Final Dimensions (mm) of the Ultra-miniature CBSA

W	22.5	L	26.25	W_m	1
W_p	16	L_p	14	L_m	10
D_{via}	0.8	T_{via}	1.25	W_s	4.3
W_t	3.45	L_t	5	L_s	23.3
W_f	3	W_g	1	h_1	3.2
L_{IO1}	6	L_{IO2}	7	h_2	0.5

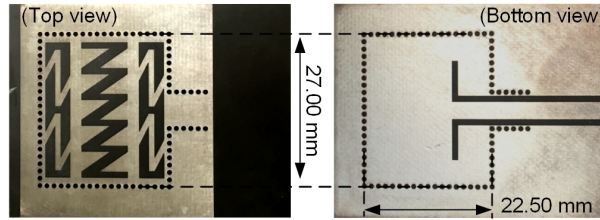


Figure 3.6: Top (left), and bottom (right) views of the fabricated ultra-miniature CBSA.

3.3 Fabrication and Experimental Results

Fig. 3.6 shows the top and bottom views of the fabricated ultra miniature CBSA. First, top and bottom metal layers are etched on the top metalization side of the upper substrate, and bottom metalization side of the lower substrate, respectively. Then, the floating patch is etched on the top metalization side of the bottom substrate, while the bottom metalization side of the upper substrate is completely removed. Finally, the two substrate layers are bonded to each other using the Rogers prepreg material, and the plated cavity via-wall is drilled through all the substrates. The proposed antenna operates at 2.1 GHz, and its size is 27 mm x 22.5 mm, which is equivalent to $0.15\lambda_0 \times 0.18\lambda_0$, where λ_0 is the wavelength in free space at the frequency of operation. As a result, miniaturization factor of 87% is achieved in the proposed CBSA, compared to a conventional SIW CBSA operating at a same frequency.

The input reflection coefficient of the fabricated antenna is measured using an Agilent

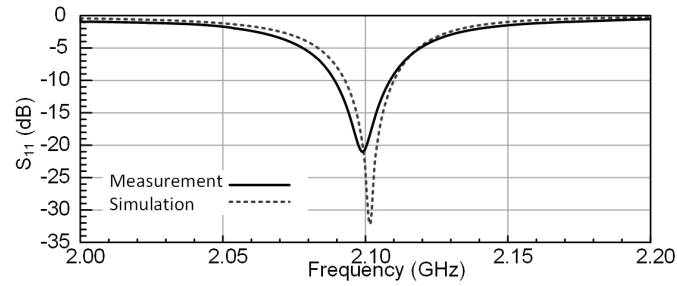


Figure 3.7: Simulated (dashed), and measured (solid) reflection coefficient of the proposed ultra miniature CBSA.

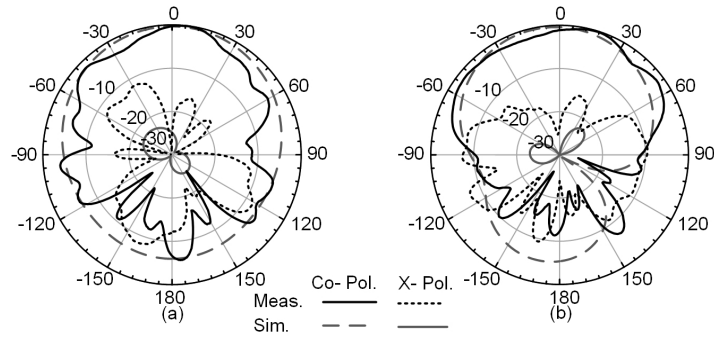


Figure 3.8: Normalized simulated and measured radiation patterns of the proposed CBSA, (a) E-plane co-Pol., and X-Pol., (b) H-plane Co-Pol. , and X-Pol..

N5230A calibrated vector network analyzer (VNA). The simulated (dashed) and measured (solid) S_{11} results of the proposed antenna are shown in Fig. 3.7. The measured return loss is ~ 20 dB at 2.1 GHz. There is a slight frequency shift between the measurement and simulation results, which is probably due to tolerance in the exact dielectric constant of the substrates, and the effect of SMA connectors. The measured BW of the proposed antenna is $\sim 0.95\%$ which is mainly limited due to the high MF of 87%. The BW can be further improved by using higher dielectric thicknesses [48].

Fig. 3.8 shows the simulated and measured normalized co- and cross- polarized radiation patterns of the proposed antenna in both the E- and H- cut planes. The polarization

of the antenna is linear and offers a pattern purity (i.e. difference between the cross- and co- polarized levels) of better than 20 dB at $\theta=0$. The measured maximum gain of the antenna is 3.6 dBi, while its radiation efficiency is $\sim 80\%$. The FTBR of the proposed ultra miniature CBSA is extracted from the measured radiation patterns, and is equal to 5.7 dB. This is smaller than FTBR of a conventional CBSA (~ 8.3 dB) [48], which is mainly due to the significant decrease in the size of the antenna. The miniaturization factor of 87% along with the folded CB-CPW excitation on the bottom metal layer of the antenna are both responsible for decrease in the FTBR.

Table 3.3 compares the measured performance characteristics of the proposed ultra-miniature antenna with the previously-reported works in literature. Size of the antennas are reported relative to the air wavelength at the operating frequency to present a fair size comparison. As can be seen, the proposed antenna has the highest miniaturization factor, while it keeps the high performance characteristics of CBSAs in general.

Table 3.3: Comparison of Related Works in Literature

	Antenna Type	Operating Center Frequency (GHz)	Miniaturization Factor (%)	Gain (dBi)	Radiation Efficiency (%)	Size
[48]	compact CBSA with a conventional bulky cavity	2.5	65	3.5	95	$\sim 0.45\lambda_0 \times 0.15\lambda_0 \times 0.05\lambda_0$
[49]	Conventional SIW CBSA	10	0	5.3	86	$\sim 0.8\lambda_0 \times 0.66\lambda_0 \times 0.01\lambda_0$
[51]	Miniaturized SIW CBSA based on Negative-order resonance	7.75	68	4.31	86	$\sim 0.33\lambda_0 \times 0.3\lambda_0 \times 0.03\lambda_0$
This Work	Ultra-miniature SIW CBSA	2.1	87	3.6	80	$\sim 0.18\lambda_0 \times 0.15\lambda_0 \times 0.02\lambda_0$

4. CIRCULAR ANTENNA ARRAYS FOR MILLIMETER-WAVE APPLICATIONS

4.1 Introduction

Since 1979, almost every ten years a new generation of wireless communication service has been launched; from 1st generation (1G) analog cellular systems to 4G / Long Term Evolution (LTE) services being deployed nowadays all around the globe. However, the 5th generation (5G) is emerging even before the turn of a new decade [52]. This can be mainly due to the tremendous demand for considerably higher data rates, and available channel capacity for areas such as stadiums, downtowns, or anywhere with highly dense population [53]. While, the 5G spectral band is not yet fully allocated, recent advancements show that the 28 GHz band is particularly interesting for mobile standardization [54].

In spite of 5G technology advantages, effective communication at mm-wave suffers from severe signal attenuation/path loss. As a remedy, highly directional antenna arrays are usually deployed to achieve the required signal to noise ratio [55]. The array configurations that are mainly implemented in literature are either linear or rectangular arrays [15, 55, 56]. However, one of the main drawbacks of such arrays is the intrinsic asymmetry in the array configuration, which directly affects the 360° beam steering capability. Moreover, it has been discussed that there is between 3 dB ~ 5 dB gain fluctuations in the main lobe of rectangular array radiation patterns in different azimuthal cuts [14]. Due to severe path loss at mm-wave, such a power loss due to gain fluctuations in different azimuthal angles cannot be neglected. This gain fluctuation also makes the rectangular arrays more sensitive to beam misalignment.

On the other hand, it is theoretically proven in [16], that uniform circular arrays provide multiple advantages compared with uniform linear or rectangular arrays. Circular arrays

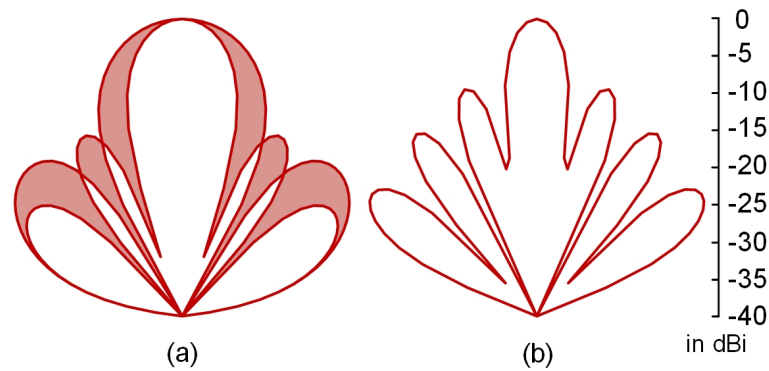


Figure 4.1: (a) uniform rectangular array, pattern variation in different azimuthal angles are highlighted, (b) circular array with excitation phases rotating 360° provides no variation due to its symmetry.

have symmetric configuration, and therefore, more immune to beam misalignment. Moreover, the circular array has ideally no azimuthal gain fluctuation due to its axial symmetry. It is theoretically shown that uniform circular arrays provide narrowest main beam-width, and therefore best spacial resolution. This is mainly due to larger radiation aperture of the circular shape in comparison with the other two. It also has deepest nulls toward angles of interfering signals compared with uniform linear or rectangular arrays. Because of its larger dimensions, the use of uniform circular array has been highly limited in practical implementations. However, this parameter is less of importance at 5G since the antenna dimensions are considerably smaller at mm-wave compared with microwave range.

In order to better show the difference, rectangular and circular antenna arrays with 24 isotropic antenna elements with same spacing of 0.5λ are simulated in MATLAB, and the azimuthal variation in the radiation patterns are compared in Fig. 4.1. These plots are generated by overlaying multiple pattern cuts in different azimuthal angles around the broadside direction to determine the maximum rotational variation of the pattern. As can be seen, the circular array provides azimuthal symmetric radiation pattern and it provides a more efficient usage of the array aperture. Although, the use of circular arrays for

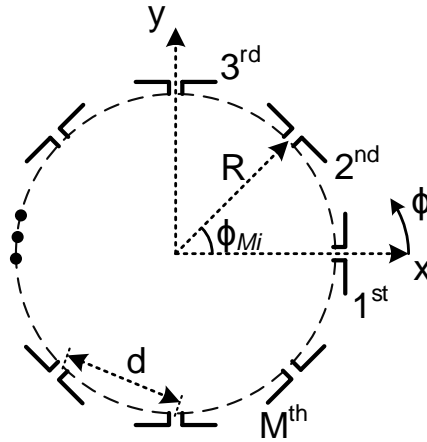


Figure 4.2: Geometry of a uniform circular array with a single ring with a radius of R , and element spacing of d .

5G applications seems promising, the previously-published implementations have been extensively focused on linear or rectangular array configurations, which [15, 55–57] are some examples.

In this section, an eight-element uniform circular array based on substrate integrated waveguide (SIW) technology is designed and implemented for 29 GHz applications. The antenna elements are considered cylindrical cavity backed slot antennas (CBSAs). A one-to-eight radial power divider is presented to feed the eight CBSAs in a circular configuration. The fabrication considerations are discussed, and the fabricated prototype is measured which shows good agreement with simulated results. The antenna array shows measured $\sim XX$ dBi peak realized gain with axial symmetry, and a radiation efficiency of $XX\%$ at 29 GHz. To the best of author’s knowledge, this is the first presentation of a SIW-based radial one-to-eight power divider suitable for 29 GHz band, and implementation of a uniform circular antenna array for 29 GHz band using SIW technology.

4.2 Uniform Circular Array

A uniform circular array with dipole elements is shown in Fig. 4.2. The ring has a radius of R , and consists of M elements which the angular position of the M_i -th element is as below:

$$\phi_{M_i} = \frac{360^\circ \times M_i}{M}, \quad M_i = 1, 2, \dots, M. \quad (4.1)$$

In this case, the array factor can be written as below [2]:

$$AF_{(\theta, \varphi)} = \sum_{n=1}^M A_n e^{j[kR \sin \theta \cos(\phi - \phi_{M_i}) + \phi_n]}, \quad (4.2)$$

where A_n , and ϕ_n are the amplitude and phase excitations of each element, and k represents the wave number. A more generic configuration is to have multiple concentric circular arrays to form a circular planar array. However, a single ring array is targeted for implementation in this section due to physical size considerations. In case of a uniform array, all the amplitude and phase excitations (A_n , and ϕ_n) are identical. Therefore, the two main parameters of the array configuration are the radius, R , and the number of elements, M .

In order to visually show the effect of the radius and number of elements of uniform circular array on the radiation pattern, a MATLAB code is constructed based on the circular array factor (4.2). In this code, the antenna elements are assumed to be ideal half-wavelength dipoles resonating at 28 GHz. Also, the mutual couplings between array antenna elements are neglected. Fig. 4.3 shows the total radiation patterns for 8 and 16 elements arrays with various radii in one azimuthal cut, while the arrays are placed in X-Y plane. Due to the axial symmetry, other azimuthal cuts are not shown. Based on these radiation patterns, having larger number of elements and/or increasing the radius of the

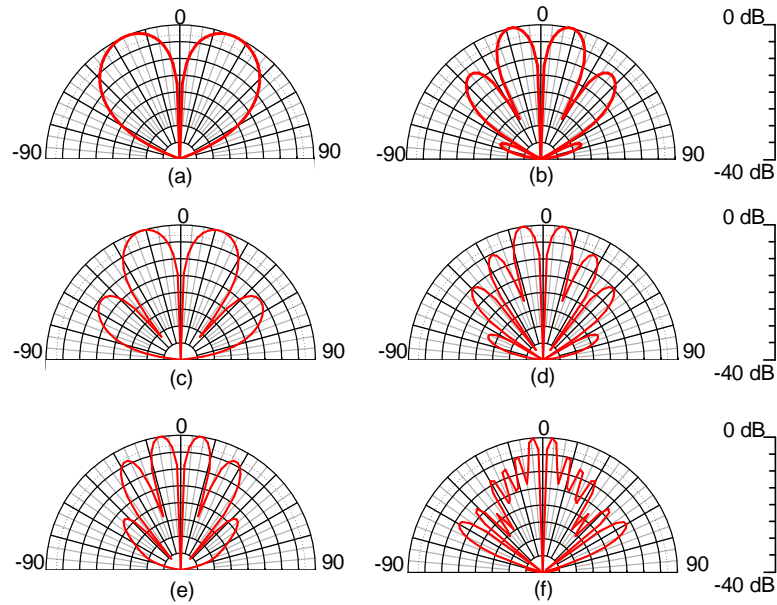


Figure 4.3: Azimuthal total radiation pattern of uniform circular ideal half-wavelength dipole antennas with (a) $n = 8$, $R = 0.5\lambda$, (b) $n = 16$, $R = 0.5\lambda$, (c) $n = 8$, $R = 0.75\lambda$, (d) $n = 16$, $R = 0.75\lambda$, (e) $n = 8$, $R = 1.5\lambda$, and (f) $n = 16$, $R = 1.5\lambda$.

ring will both increase the directivity of the main lobe, while it also causes grating lobes and nulls. It is also mentioned in [2] that for very large radius of the array the directivity approaches the value of M . The higher directivity causes better spacial resolution, while the nulls can be properly located to attenuate the interfering signals as was discussed in [16]. Increasing the radius of the ring also increases the size of the array. As a result, the objective is to achieve the largest possible number of elements in the smallest possible radius. Although, ideally this is simply possible with isotropic elements, actual antennas with practical feeding networks limit the number of elements that can be fitted with correct spacings in one circular ring. Such a study gives the designer an intuition of the required number of elements and an estimation of the desired radius, however, quantitative comparison is not accurate using this model since the antenna is assumed ideal half-wavelength dipole, and also mutual coupling between the elements are not considered.

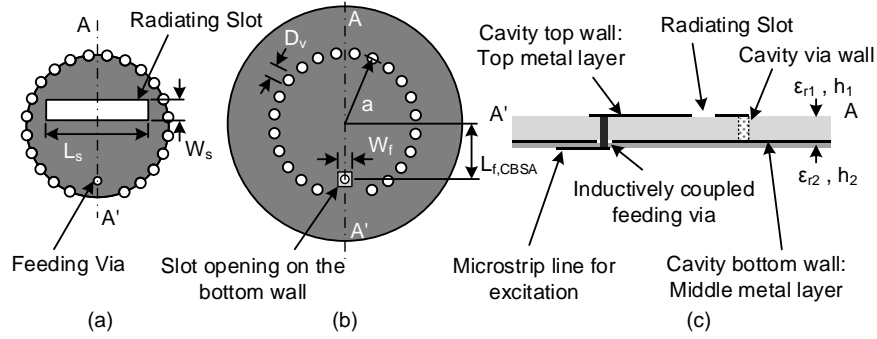


Figure 4.4: Single antenna element configuration: (a) top metal layer view, (b) middle metal layer view, and (c) A-A' cross-sectional view. The dimension values are: $a=2.67$ mm, $D_v=0.4$ mm, $L_s=3.85$ mm, $W_s=0.8$ mm, and $W_f=0.55$ mm.

4.3 Single Antenna Element

As was mentioned earlier in the introduction (Section 4.1), high attenuation/loss at mm-wave makes it challenging to achieve high radiation efficiency in antenna design, while this is a crucial parameter in mm-wave range. The CBSA is a resonance-based relatively high-Q antenna, and has a highly isolated structure which reduces the leakage/radiation loss. Therefore higher radiation efficiencies can be achieved using CBSAs as the array antenna elements compared with more conventional array elements such as dipole, patch, or microstrip antennas. Furthermore, in a realistic scenario, on the user side, the antenna might be accompanied by other system parts such as the LCD, battery, PCB substrate, transceiver modules, etc., all of which are scatterers and will affect the radiation performance. However, the CBSA can be isolated from the other parts of the system to some extent by sharing the ground plane in between, and having the antennas on the back side of the substrate.

Fig. 4.4 (a), and (b) show the top and bottom metal layers of the designed cylindrical CBSA based on SIW technology, respectively, and Fig. 4.4 (c) shows the side-view of the simulated single antenna element in HFSS. The cylindrical SIW cavity resonator's di-

mensions are determined based on the fundamental TM010 mode [41]. Utilizing a Rogers RT/Duroid 5880 substrate with a thicknesses of $h_1 = 0.787$ mm, a is calculated to be 2.67 mm. As a result a fundamental TM010 mode exists around 29 GHz. As was mentioned in Section 2, the length of the radiative slot is roughly $\lambda_g/2$, where λ_g is the guided wavelength along the slot. The length of the slot ($L_s = 3.85$ mm) is coarsely tuned to adjust the center frequency at ~ 29 GHz. On the other hand, the width of the radiating slot (W_s), affects the antenna bandwidth. By increasing the width of the slot, the Q of the cavity resonator drops, and as a result, higher bandwidths can be achieved. In this design, the W_s is chosen to be 0.8 mm to have a bandwidth of 480 MHz over the center frequency of 29.12 GHz. The slot width cannot be excessively increased, since there is no enough space on the cavity top wall.

The antenna is fed based on inductive coupling. The feeding via is disconnected from the cavity's bottom wall using a rectangular slot on the ground metal plane, while it is connected to the top metal wall. This way it is possible to excite the antenna from back side of the ground metal plane, and therefore, it gives the flexibility to have the array's power divider on the back side of the substrate, and isolated from the antenna. The feeding via is connected to an ideal 50Ω microstrip line on the other side of the substrate in the full-wave simulations at this stage. However, as will be discussed in Section 3.5, the ideal microstrip lines are replaced with the power divider output ports for the practical implementation. The 50Ω microstrip feed line is designed based on a Rogers RO4003 substrate with a thickness of $h_2 = 0.2$ mm (See Fig. 4.4 (c)). In order to achieve the required impedance matching, the location of the feeding via inside the CBSA needs to be adjusted correctly. While the feeding via is closer to the cavity side-wall, the input impedance is closer to 50Ω . However, as it gets further away from the cavity side-wall, and closer to the radiating slot, the input impedance drops. Therefore, the $L_{f,CBSA}$ value is chosen 1.845 mm in order to achieve the VSWR of less than 1.5.

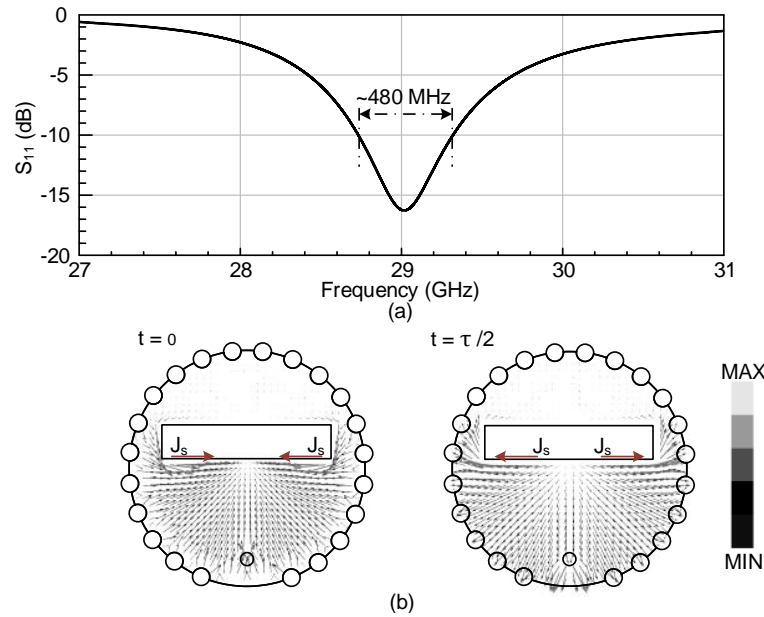


Figure 4.5: (a) Simulated reflection coefficient of the circular CBSA, and (b) simulated surface current distribution on the top metal layer of the antenna at $t = 0, \tau/2$.

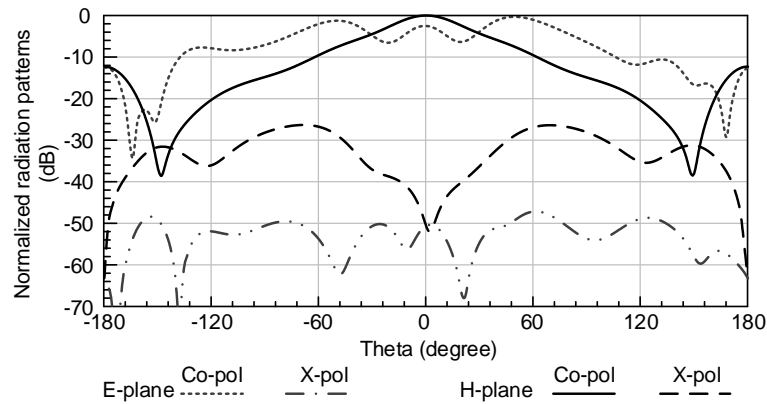


Figure 4.6: Normalized simulated E- and H-planes co- and x-pol. radiation patterns of the single CBSA array element at 29 GHz.

Fig. 4.5 (a) shows the simulated reflection coefficient of the antenna, which supports the 480 MHz bandwidth over 29 GHz. The simulated surface current distribution on the top layer of the antenna is shown in Fig. 4.5 (b) at $t = 0$, and $\tau/2$, where τ is the period

of the current. The surface current is approximately zero at $t = \tau/4$, and $3\tau/4$. The dominant surface current direction shows 180° phase change in a half cycle. Therefore, as was expected, the antenna provides linear polarization. The antenna's normalized E-, and H-plane co-, and cross-polarization radiation patterns are shown in Fig. 4.6 at 29 GHz. The antenna peak gain is 3.18 dBi, and has a front to back ratio (FTBR) of ~ 7 dB. Because of the utilized relatively high-Q resonator-based antenna design, the simulated radiation efficiency of the single antenna is 88%. This would degrade in practice due to the practical losses of the imperfect transitions, and also higher dielectric and conductor losses at mm-wave.

4.4 Circular Power Divider Design

The power divider requires to have axial symmetry to feed the antennas in a circular configuration. Moreover, it has to be low loss since the operating frequency is in mm-wave range. It also needs to have negligible amplitude and phase imbalance, and low mutual coupling between different ports. As a result, cavity-based axially symmetric power divider can be considered as a suitable candidate. Such power dividers have low loss because of high-Q nature of the cavity resonator structure, and low amplitude and phase imbalance due to the symmetric configuration [58,59]. The cavity can be implemented using the SIW technology, and therefore, it is conveniently integrable with the SIW CBSAs on the same board.

Fig. 4.7 (a), and (b) show the top, and bottom views of the designed one-to-eight SIW cavity-based power divider, respectively. The A-A' cross section view of the power divider is also shown in Fig. 4.7 (c). As can be seen, the center radial cavity is fed from the center using a metalized via connected to the middle metal layer, and disconnected from the bottom metal layer. A mini SMP connector is utilized for the transition. The center conductor of the mini SMP is soldered to the center feed via, while the ground is soldered

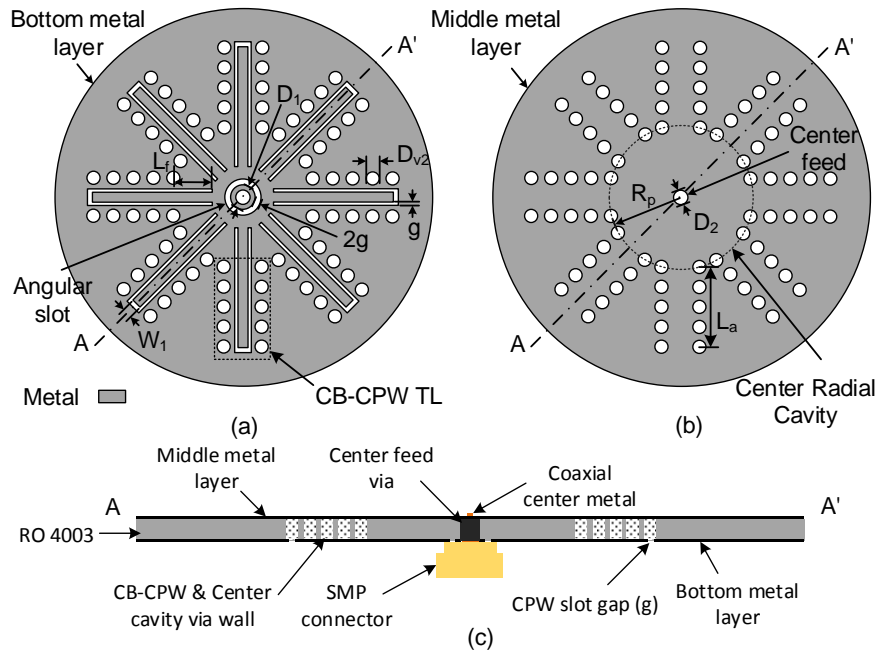


Figure 4.7: (a) Bottom metal layer (power divider bottom view), (b) middle metal layer (power divider top view), and (c) A-A' cross-section views of the designed one-to-eight SIW cavity-based power divider. The dimension values are: $D_1=1$ mm, $D_2=0.6$ mm, $D_{v2}=0.6$ mm, $L_f=1.18$ mm, $L_a=3$ mm, $g=0.1$ mm, $R_p=2.2$ mm, $W_1=0.3$ mm.

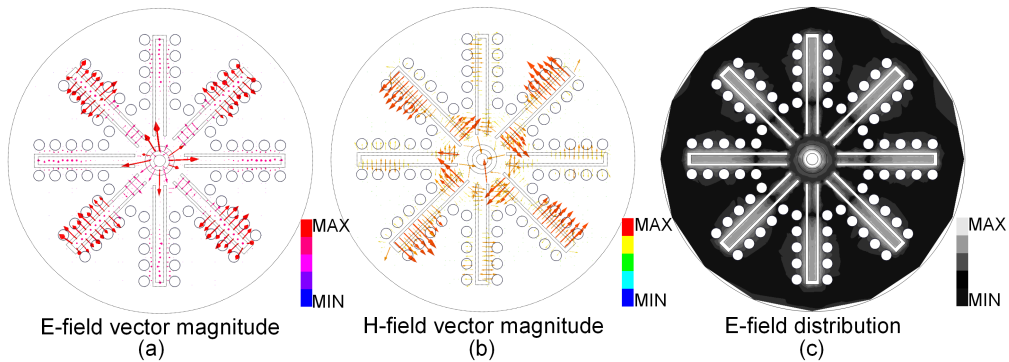


Figure 4.8: (a) E-field, and (b) H-field vector magnitude plots for the power divider. (c) The E-field magnitude distribution on the bottom metal layer of the power divider.

to the bottom metal layer. The size of the center feed via (D_2) is determined based on the size of the available commercial mini SMP connectors. Utilizing a Rogers RO 4003

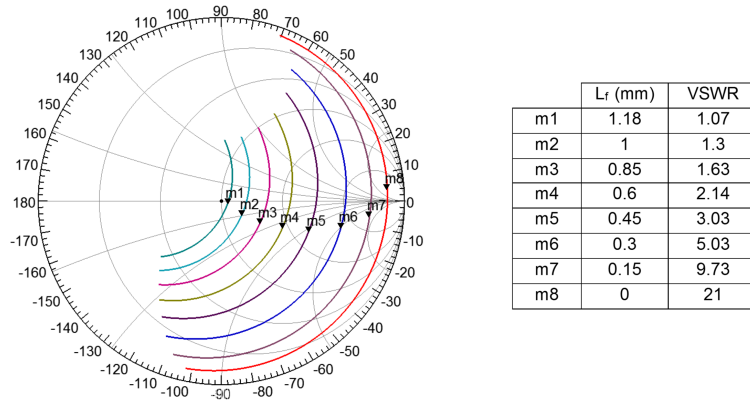


Figure 4.9: The S_{11} of the radial power divider for various L_f values.

substrate with a thicknesses of $h_c = 0.2$ mm, a fundamental mode is excited at 29 GHz with R_p equal to 2.22 mm. Since the cavity is fed from the center, and the center feed via is disconnected from the bottom metal layer using an angular slot, this fundamental mode can be inferred as a quasi-TEM [1]. In order to better study the electromagnetic fields inside the center radial cavity, the E-field, and H-field vector magnitudes are extracted from full wave simulations at 29 GHz at $\tau_2=0$, where τ_2 is the period of the E-field distribution, and shown in Fig. 4.8 (a), and (b), respectively. As can be seen, the E-field vector is radially directed, while the H-field is rotating around. As a result, the excited fundamental mode inside the cavity using the center via feed structure is the quasi-TEM.

The eight outputs need to support the quasi-TEM mode, and as a result, conductor-backed coplanar waveguide (CB-CPW) lines are coupled to the cavity. The propagation in CB-CPW lines is considered as quasi-TEM, since half the propagation medium is inside the substrate, and the other half is in air [1]. The magnitude of E-field distribution is shown in Fig. 4.8 (c) at 29 GHz at $\tau_2=0$. As can be seen, the eight CB-CPW lines act as power divider outputs and the E-field distribution on the whole bottom metal layer has angular symmetry. The gap width between the signal route and the ground plane ($g = 0.1$ mm) is chosen to achieve 50Ω CPW lines on the RO4003 substrate. However, the input

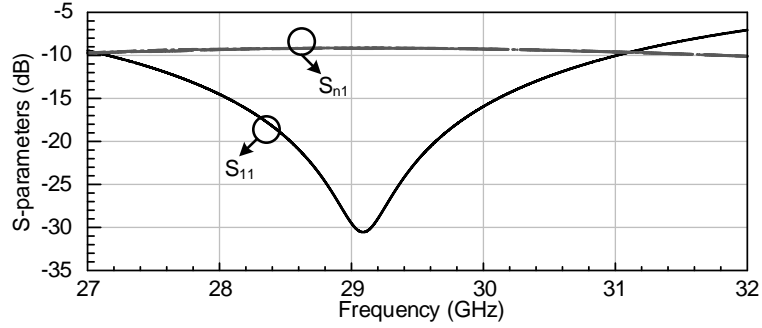


Figure 4.10: Simulated reflection coefficient of the designed one-to-eight power divider.

impedance can be tuned by adjusting the length of the CPW line that enters the cavity (L_f). The relationship between the input impedance matching and L_f value is studied and shown in Fig. 4.9, where the S_{11} result of the power divider is shown for various L_f values. In this plot, the markers show the VSWR value at roughly 29 GHz for each L_f value on the smith chart. As can be seen, the VSWR is less than 1.1 for L_f of 1.18 mm. However, as the L_f value decreases, and the end of the CPW lines become closer to the cavity side-wall, the input impedance increases, and becomes closer to the open-circuit point on the smith chart. All the final dimensions are mentioned in the caption of Fig. 4.7.

The CB-CPW output lines have two benefits. First, due to the vias around the signal route, a relatively high isolation and low loss can be achieved. As a result, the mutual coupling between adjacent output ports can be minimized, and this reduces the mutual coupling between the antennas in the array design. Second, the CB-CPW output line can have any length outside the center cavity (L_a), and therefore it gives the flexibility to adjust the radius of the circular array to the desired value. Fig. 4.10 shows the simulated reflection coefficient of the input port, and also the transmission coefficients from the input port at the center of the cavity to each of the output ports (S_{n1} , $n=2, \dots, 9$). As can be seen, the amplitude imbalance is negligible which is due to the symmetry of the structure. Moreover, the S_{11} suggests a bandwidth of ~ 2.9 GHz over 29 GHz.

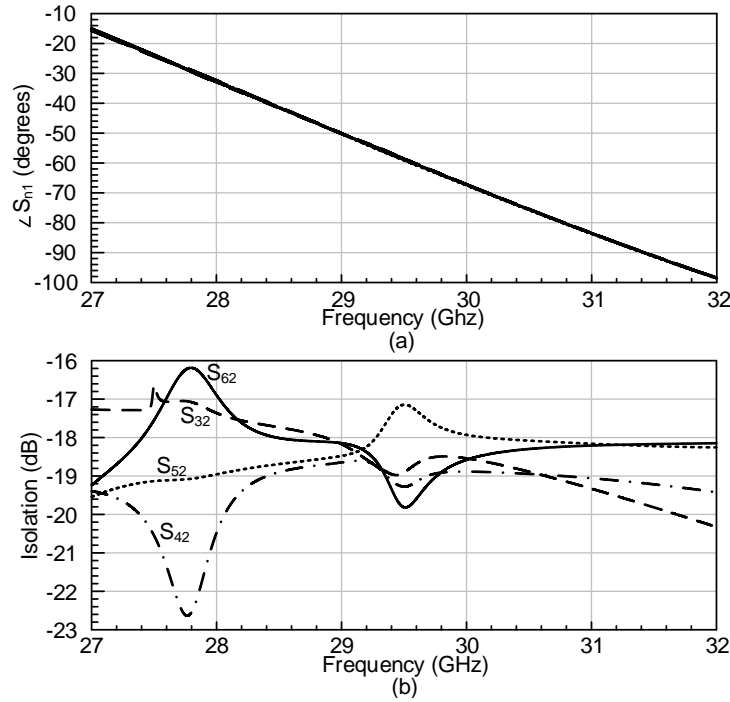


Figure 4.11: (a) Phase response between the input port and each of the output ports, and (b) the isolation between the power divider's output ports.

Fig. 4.11 (a) shows the simulated phase responses of S_{n1} . Similar to the amplitude, the phase responses are almost identical and the phase variations are negligible. Fig. 4.11 (b) shows the isolation between the ports S_{32} , S_{42} , S_{52} , and S_{62} . However, S_{72} , S_{82} , and S_{92} are not shown since they are identical to S_{32} , S_{42} , and S_{52} , respectively, due to the axial symmetry. As can be seen, an isolation of better than 18 dB at 29 GHz is achieved for the worst case scenario between two adjacent ports (in this case S_{32}). This power divider is utilized to design an 8-element circular antenna array as will be discussed in Section 3.5.

4.5 Eight-element Circular Antenna Array

Fig. 4.12 (a) shows the top, and A-A' cross-sectional views of the designed eight-element circular antenna array. Also, the 3D extended view of the presented antenna is shown in Fig. 4.12 (b) to better clarify the multi-layer structure. Eight CBSAs are placed

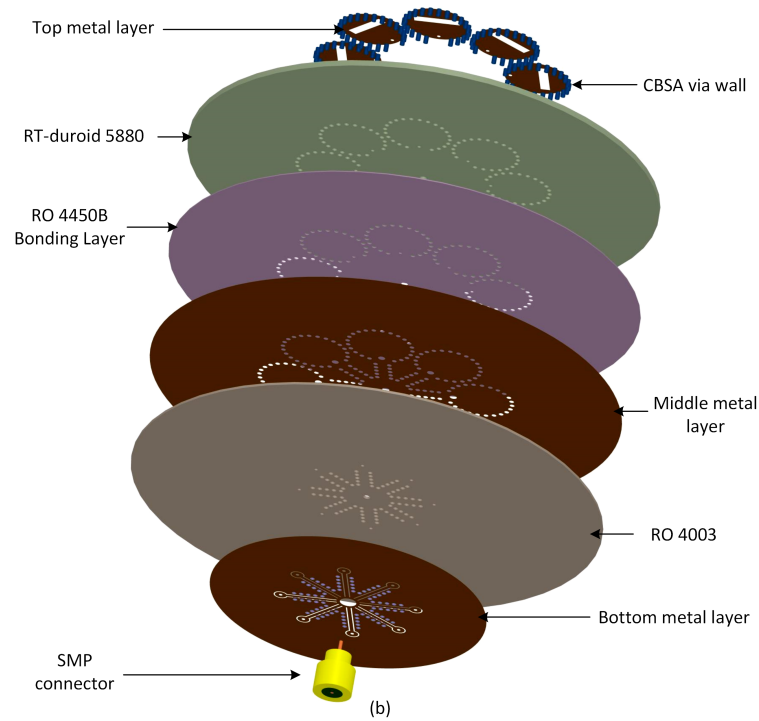
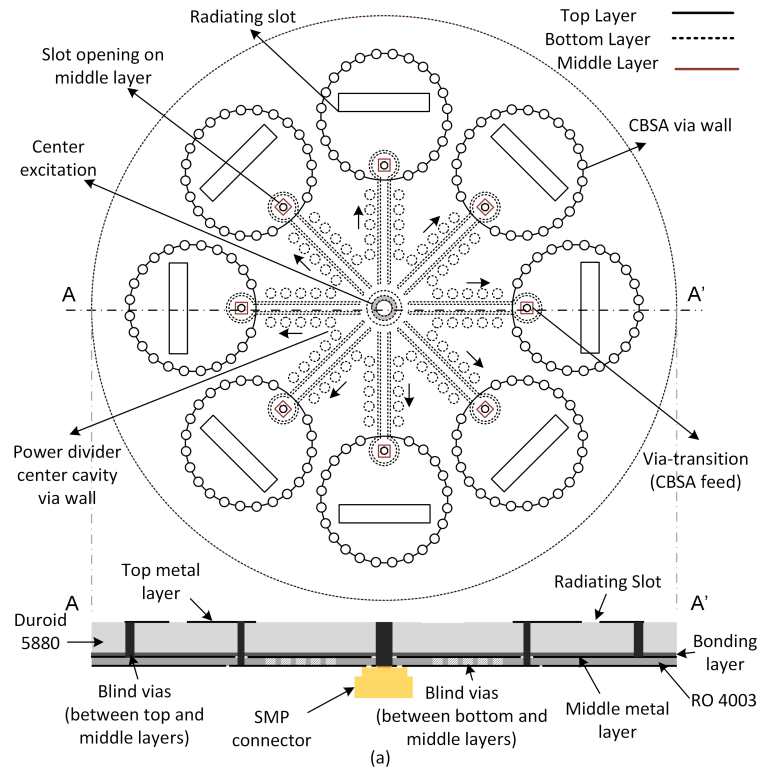


Figure 4.12: (a) Multi-layer and cross-sectional A-A' views of the complete eight-element circular CBSA array, and (b) 3D extended view of the complete eight-element antenna array.

in a circular configuration with 45° angle between the adjacent ones. The CBSAs are implemented based on the Rogers RT-duroid 5880 with a thickness of 0.508 mm. The CBSAs via walls are all blind vias that connect the top to the middle metal layer. The antennas are fed using through vias, connecting the outputs of the power divider on the bottom metal layer to the top metal layer of the CBSAs. The middle metal layer acts as a shared ground, and a square-slot opening is etched around the through vias that feed the antennas to disconnect them from the shared ground. The power divider is implemented based on a Rogers RO 4003 with a thickness of 0.2 mm. The center cavity via wall, and also the CB-CPW vias are all considered blind vias connecting the bottom to the middle metal layer. The center cavity power divider is fed using a through via connecting the bottom to the middle metal layer, and disconnected on the top, and its diameter (D_2 in Fig. 4.7) is determined based on the available commercial SMP connector size ($D_{SMP} = 0.3$ mm). The two dielectric layers are assumed to be bonded to each other using a Rogers RO 4450B prepreg material. The effect of the SMP, and the prepreg material are all considered in full-wave simulations in HFSS.

The radius of the array is determined to be minimum possible to fit eight CBSAs in one circle. In this case, the radius, $R_p + L_a$ (shown in Fig. 4.7) is 5.6 mm, which is roughly 0.5λ . Achieving such a small radius became feasible due to using a radial cavity-based power divider in a multi-layer configuration. As was discussed in Section 3.2, having a small radius with enough number of elements results in lower number of grating lobes. Moreover, since the operating frequency is in the mm-wave range, having a more compact feeding structure with smaller lengths of transmission lines results in lower dielectric, conductor, and leakage losses, and therefore a higher radiation efficiency can be achieved which is crucial at mm-wave range.

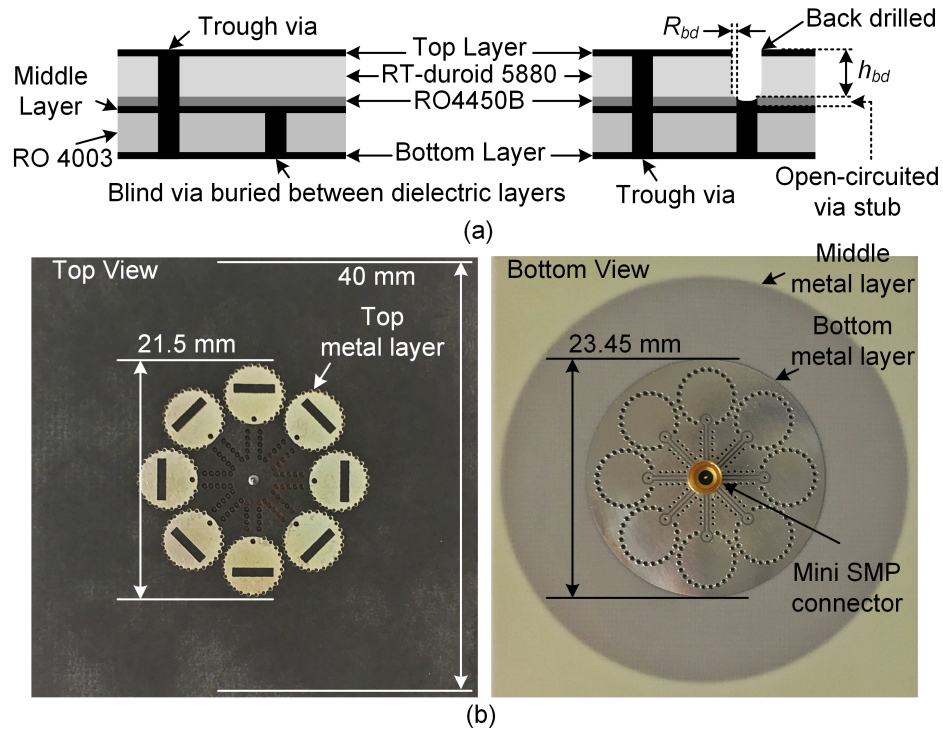


Figure 4.13: (a) Blind via implementation conceptual photos, and (b) top and bottom views of the fabricated eight-element circular antenna array prototype (This picture will be replaced with the actual fabricated prototype photo).

4.6 Implementation & Experimental Results

As was discussed in Section 4.5, the proposed multi-layer structure has both blind and through vias. There are blind vias from the bottom to the middle metal layer for the power divider, and also, from the top to the middle metal layer for the CBSAs. Since two different dielectric layers need to be bonded to each other using a Prepreg bonding material, having blind vias in both the dielectric layers makes the fabrication more challenging and costly. There are primarily two approaches available to implement the blind vias. Fig. 4.13 (a) conceptually shows the two methods. On the left, the via is drilled in the first dielectric layer, and then metalized for connection. Afterwards, the second dielectric layer is bonded to the first one, and therefore, the blind via is buried inside the final multi-layer

structure. This method has been implemented before with Rogers materials more commonly, which [43] is an example. On the right, however, the back-drilling technique is shown. In this case, first, the two dielectric layers are bonded to each other using the Prepreg material. Afterwards, the via is thoroughly drilled and metalized all the way from the top to the bottom layers. Finally, in order to make a blind via, and remove the rest of the via metalization, a slightly larger drill is utilized for back-drilling with a specific desired depth (h_{bd}). The back-drilling technique is less expensive and make the fabrication and bonding process more straightforward. Ideally, it is possible to remove the entire unused metalized portion of the via using back-drilling, however, in practice the depth (h_{bd}) has a tolerance, and a part of the via remains metalized. At high frequencies, the metalized via opening might act as an open circuited stub, and therefore affects the performance. However, In this design, the tolerance is 0.07 mm, which is negligible compared with the targeted wavelength.

Fig. 4.13 (b) shows the top and bottom views of the fabricated prototype. First, the top and bottom metal layers are etched on the top side of the Rogers 5880 substrate, and the bottom side of the RO 4003 substrate, respectively. Afterwards, the bottom metal layer of the Rogers 5880 is completely removed, and the top-side metal layer of the RO 4003 is etched to form the middle metal layer. Then, The two substrates are bonded to each other using Rogers 4450B Prepreg material. Finally, all the vias are first drilled and metalized as plated through vias, and then the blind vias are achieved using the described back-drilling technique. The overall size of the eight-element antenna array is $40 \text{ mm} \times 40 \text{ mm}$, which is $3.71 \lambda_0 \times 3.71 \lambda_0$, and λ_0 is the wavelength in free space at the frequency of operation. The structure is fed using a mini SMP connector with its core conductor diameter value equal to 0.3 mm, which supports operation up to 40 GHz.

The input reflection coefficient of the fabricated antenna array prototype is measured using an Agilent N5230A calibrated Vector Network Analyzer (VNA). Fig. 4.14 shows the

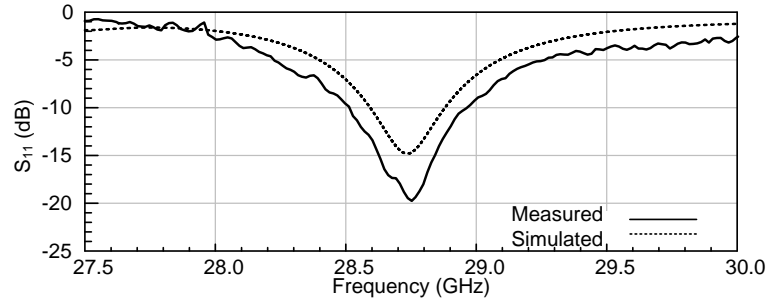


Figure 4.14: Measured (solid), and simulated (dashed) reflection coefficient of the eighth-element circular antenna array.

simulated (dashed) and measured (solid) S_{11} results, which good agreement is achieved. The return loss is ~ 15 dB at 28.7 GHz, with a 10-dB BW of ~ 500 MHz. Modeling the conductor, and dielectric losses at mm-wave in full-wave simulations is challenging since these values for commercial dielectric materials are usually reported by the manufacturers at the microwave range. As a result of the higher practical losses of the dielectric materials at mm-wave range, and also the transitions' imperfections such as the SMP to the cavity transition, the quality factor of the both power divider cavity, and the CBSAs drop, and therefore, the measured bandwidth of the antenna array is slightly higher than the simulated one.

Fig. 4.15 shows the simulated and measured normalized co- and cross-polarized radiation patterns of the proposed antenna array in various axial plane cuts. As was expected, the radiation patterns are almost identical in the direction of the main beam at different azimuthal cuts, which is due to the symmetry of the structure. The polarization of the antenna array is linear, and the pattern purity (i.e., difference between the cross- and co-polarized levels in the direction of the main beam) of better than 30 dB is achieved. The measured front to back ratio (FTBR) of the proposed antenna array, extracted from the measured radiation patterns, is better than ~ 12 dB.

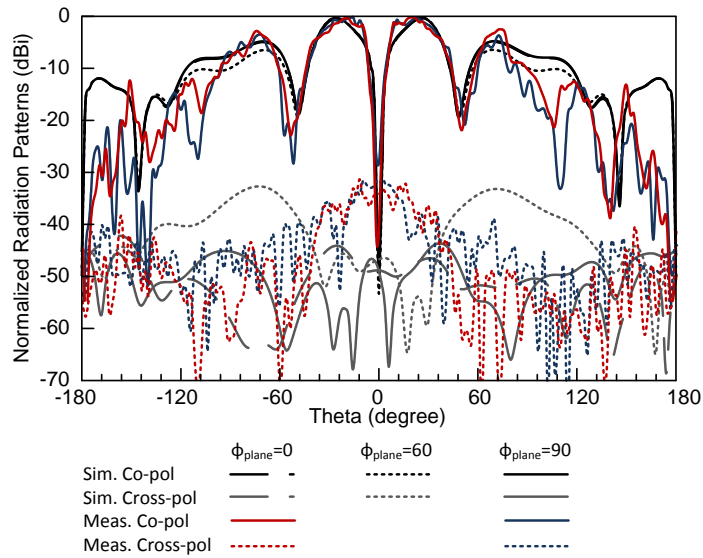


Figure 4.15: (a) Measured (solid), and (b) simulated (dashed) normalized co- and cross-polarized radiation patterns of the eight-element circular antenna array in various axial plane cuts.

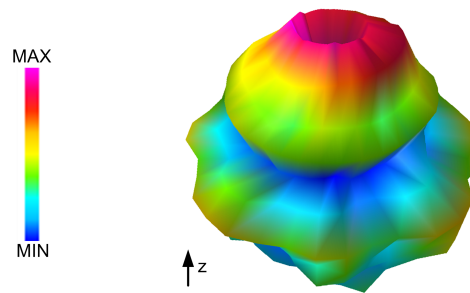


Figure 4.16: Measured normalized total 3D radiation pattern of the eight-element circular antenna array with 10° resolution.

Fig. 4.16 shows the measured normalized total 3-dimensional (3D) radiation pattern of the proposed antenna array. This measured plot is captured with 10° resolution, while the 2D radiation pattern plots in Fig. 4.15 are captured based on measurement with 2° resolution. As can be seen, the radiation pattern has radial symmetry which is beneficial for hand-held devices with 5G applications. The measured realized gain and the radiation

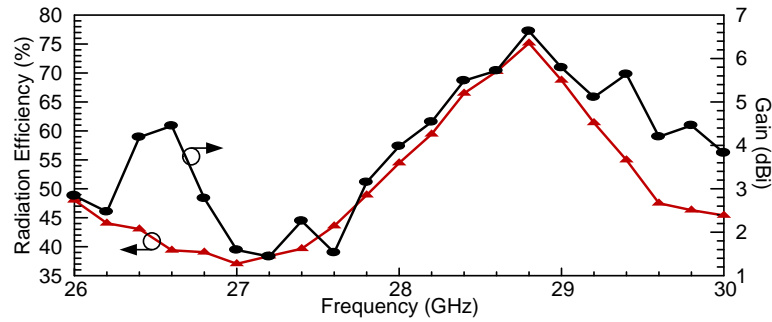


Figure 4.17: Measured gain and radiation efficiency of the proposed eight-element circular antenna array.

efficiency of the array antenna is depicted in Fig. 4.17 from 26 to 30 GHz with 200 MHz resolution. The measured maximum realized gain of 6.61 dBi is achieved at 28.8 GHz. At this frequency, measured maximum radiation efficiency of $\sim 75\%$ is achieved which is lower than the simulated radiation efficiency of $\sim 88\%$. This is due to the higher dielectric and conductor losses at mm-wave range, and also the imperfections in the transitions, both of which were also responsible for having a slightly higher bandwidth. However, since both the power divider and the antennas are resonance-based relatively high-Q structures, the radiation efficiency is comparably higher than the reported state of the art antenna arrays at 28 GHz range, i.e. [15, 57, 60].

5. COMPACT MICROWAVE DIELECTRIC SPECTROSCOPY SYSTEMS

5.1 Introduction

Microwave interferometry has been utilized over the past decade for a broad area of applications from noise measurement system [61], and spatial displacement measurement [62], to single-cell viability detection [23], and material characterization [63], [64]. Optical interferometry [65], THz sensing [66], and Fourier transform Infrared spectroscopy (FTIR) [67,68] have been proven to be highly accurate, but costly and complex, in characterizing the frequency spectral features of materials in the range of 300 GHz to few THz. The choice of a particular method depends on the application, setup-complexity, cost, and the expected frequency range for material characterization [17]. For instance, the frequency bands of dielectric dispersion for different bio-materials are discussed in [69]. Each bio-material is responsive at a specific frequency range, from few Hz to few GHz, and therefore, a single system with limited bandwidth is unable to characterize the dispersive behavior of all various materials. Characterizing the frequency spectral behavior of materials for frequency range below 100 GHz is the main domain of radio frequency (RF)-microwave sensors and spectroscopy systems [70, 71]. Microwave dielectric spectroscopy can result in a low-cost, and integrated system for lab-on-board applications [72]. One application of this method is material mixture characterization considering that the dispersive properties of mixtures of materials highly depend on their molecular-level interactions, and charge distributions that happen at microwave frequencies [73].

More recently, there has been a growing interest in microwave interferometry-based

©2017 IEEE. Part of this chapter is reprinted, with permission from IEEE, "A Metamaterial-Inspired Wideband Microwave Interferometry Sensor for Dielectric Spectroscopy of Liquid Chemicals," IEEE Transactions on Microwave Theory and Techniques, Jan. 2017.

©2016 IEEE. Part of this chapter is reprinted, with permission from IEEE, "A metamaterial-inspired miniaturized wide-band microwave interferometry sensor for liquid chemical detection," IEEE International Microwave Symposium (IMS), Aug. 2016.

dielectric spectroscopy systems due to their non-invasive, label-free, and rapid sensing capabilities [17,74]. While interferometry systems are proven to provide high resolution and accuracy, their use for broadband dielectric spectroscopy is hindered due to their narrow-band nature. One remedy is to use the interferometry-based dielectric spectroscopy system in a tunable measurement setup [75]. However, this approach requires various bulky, and expensive discrete modules such as vector network analyzers (VNAs). Due to the required complex measurement setup, the use of current interferometry-based dielectric spectroscopy systems is costly and impractical for lab-on-a-board applications.

On the other hand, the sensing part of a microwave material characterization system can be constructed using either a single resonator [74,76,77], or a transmission-line (TL) [75,78]. While the former provides a better sensitivity in a highly limited frequency band-width, the latter is suitable for broadband sensing with reduced sensitivity. Since mixtures of materials might have same dielectric constant at a specific frequency, narrow-band resonator-based methods result in ambiguity in detection of binary or multi-phase mixtures. Metamaterial-inspired TLs with their unique electromagnetic properties are capable of providing considerably higher sensitivities compared to traditional TLs [63]. A metamaterial-inspired interferometry sensor with improved sensitivity is presented in [79], which is also suitable for lab-on-a-board applications. Two composite right/left-handed (CRLH) TLs are employed in a differential architecture. The material-under-test (MUT) causes phase variation which ultimately can be detected by measuring the output power at the frequency of operation. However, since the two CRLH TLs have 180° phase difference at solely one frequency, this approach also provides narrow-bandwidth sensing. Moreover, only the real part of the dielectric constant (ϵ') is detectable using this method, and the loss information (ϵ'') of the MUT remains unknown. Also, since there are no fluidic structures, solely solid materials are characterized in [79].

While tackling the trade-off between the sensitivity and bandwidth to achieve broad-

band dielectric spectroscopy is challenging, another critical parameter of such systems is the uncertainty or error in reading. Microwave material characterization using an open-ended coaxial line is well-established over the past decade [20]. The method is based on measuring the reflection coefficient of an open-ended coaxial line exposed to the MUT. The error in this case, as the difference between the calculated and measured reflection coefficient values, is reported as 2-5% for pure methanol characterization. Modified open-ended coaxial line approaches are also reported in literature [24,80]. However, the reported uncertainty is 2-5%, and 20-30% for ϵ' , and ϵ'' measurements, respectively, while in all these works the VNA is still required as part of the measurement setup. Material characterization based on impedance variation measurement is also one of the conventional methods in this area [81]. A microwave non-contact permittivity (ϵ') and thickness sensor is proposed in [82], which is also based on measuring the impedance variations caused by solid MUTs. A single compound complementary split ring resonator (CSRR), operating at three different frequencies, is utilized as the sensing element. In this case, the reported uncertainty is 5.05%, and 4.32%, for ϵ' , and thickness measurements, respectively.

A metamaterial-inspired miniature wide-band interferometry sensor with improved sensitivity was first introduced by the authors in [25], and was used toward the detection of microfluidic-level chemicals based on ϵ' measurement. In the proposed method, two fluidically-loaded CRLH TLs are employed in a Zero-IF architecture. In this chapter, a more in-depth study on the distributed sensor section is presented in Section 5.2. Also, the system-level design is modified to measure both ϵ' , and ϵ'' by switching the RF and LO paths, and discussed in Section 5.3. Moreover, a new fabrication procedure is presented in Section 5.4.1, to increase the sensitivity for dissipation factor measurement. Distinct nonlinear dispersion characteristic of the artificial TL along with the wideband operation of the whole system, make complex dielectric spectroscopy with improved sensitivity in 4.2-8 GHz frequency band feasible. The overall area of the fabricated board is $6 \times 10 \text{ cm}^2$.

The experimental results are discussed in Section 5.4.2, which show mean squared error (MSE) of $\sim 1.1\%$, and $\sim 1.6\%$ for ϵ'_r , and ϵ''_r measurements of pure liquid chemicals, respectively, compared to the material's Debye-based relaxation models [83,84]. Moreover, Section 5.4.3 discusses the implemented binary mixture characterization with an accuracy of 1% at 5, and 7 GHz based on ϵ'_r measurements.

5.2 Sensor Design

5.2.1 CRLH TLs for Microwave Sensors

Microwave dielectric spectroscopy is feasible using TL-based sensors [63]. The liquid MUT is usually placed on top of the sensing TL using fluidic structures. The unknown material loads the exposed TL, and alters its performance characteristics. For conventional right-handed (RH) TLs, i.e., coplanar waveguide (CPW) TL [75], the MUT loads the equivalent parallel capacitor to the ground, and alters the insertion loss and the phase response of the TL. The variation in the insertion loss has the information of the imaginary part of the MUT's dielectric constant (ϵ''), while the phase change is related to the real part (ϵ'). In this case, the sensitivity is directly related to the rate of phase change compared to the rate of capacitance change. The dispersion relation for conventional RH TLs is as follows:

$$\beta d = \omega \sqrt{L \times C_{v,MUT}} \quad (5.1)$$

where ω , d , and L represent the angular frequency, the length of the TL, and the equivalent series inductor, respectively, while $C_{v,MUT}$ stands for the equivalent shunt capacitance of the TL varying for different MUTs. The sensitivity of such sensors is highly limited as the sensing element is a shunt capacitor to the ground, and the phase response is linear with respect to the frequency. Considering the fact that broad-band material characterization can be achieved using TL-based sensors, there is a trade-off between the sensitivity and

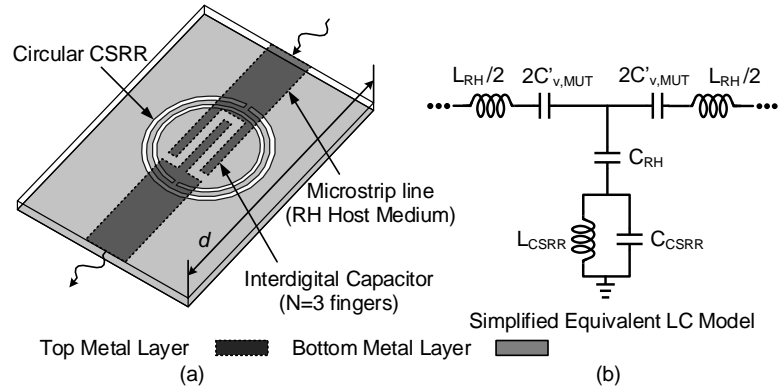


Figure 5.1: (a) CRLH TL unit-cell using microstrip line as the host RH medium, (b) Simplified equivalent LC model of one unit-cell.

the bandwidth.

On the other hand, wave propagation is possible in either double positive ($\epsilon > 0$, $\mu > 0$), or double negative ($\epsilon < 0$, $\mu < 0$) mediums, while single negative material ($\epsilon < 0$, $\mu > 0$, and $\epsilon > 0$, $\mu < 0$) prohibits wave transmission. Conventional transmission lines are categorized as double positive mediums, also called right-handed mediums, while CRLH TLs provide both the double positive and negative mediums at different frequency bands. If properly designed, the LH and RH frequency bands occur seamlessly, which in that case, balanced condition is achieved. For the sensing application, because of the distinct electromagnetic characteristics of CRLH TLs, that are not achievable using conventional TLs, a compromise between the operational bandwidth and the sensitivity can be achieved.

The CRLH TL can be constructed using metamaterial-inspired elements in an RH TL as the host medium. It is discussed in [9], split ring resonators (SRRs), and interdigital capacitors can be considered as effective magnetic dipoles, while metalized vias, and complementary split ring resonators (CSRRs) are effective electric dipoles. Combination of effective electric and magnetic dipoles results in an effective double negative, or LH, medium. Fig. 5.1 (a) shows one unit-cell of a planar CRLH TL, based on using a

microstrip line as the host medium. Modifying the ground plane by etching CSRRs as artificial electric dipoles, a 1-D medium with effective $\epsilon < 0$ is achieved. Effective medium with $\mu < 0$ is constructed using interdigital capacitor (IDC) (as an artificial magnetic dipole) on the top-plane microstrip line [85]. Because of the simultaneous $\epsilon < 0$, and $\mu < 0$ of this medium, wave propagation in both the LH and RH frequency bands can be achieved. Fig. 5.1 (b) shows the equivalent circuit model of the CRLH TL shown in Fig. 5.1 (a). In this figure, L_{RH} , and C_{RH} are the equivalent RH series inductor and shunt capacitor of the microstrip line, and their values can be extracted from the conventional TL model calculator. The parallel L_{CSRR} and C_{CSRR} represent the CSRR etched on the ground metal plane. Their equivalent values can be extracted using the model presented in [85]. The equivalent series capacitor introduced by the IDC is shown as $C'_{v,MUT}$, and its value can be extracted from the cut-off frequency of the structure when there are no CSRRs etched on the ground metal plane. This cut-off frequency is due to the resonance formed by the series inductance L_{RH} , and the series capacitor $C'_{v,MUT}$.

In this case, the equivalent series capacitance introduced by the IDC can be utilized as the sensing component, and therefore, the exposed capacitance is in series with the signal path, and higher sensitivity can be achieved. Moreover, the phase response of the CRLH TL is related to the value of this capacitance. The dispersion relation of the simplified LC model shown in Fig. 5.1 (b) is as follows [85]:

$$\cos(\beta d) = 1 + \left(\frac{L_{RH}\omega - \frac{1}{C'_{v,MUT}\omega}}{2 \left(\frac{L_{CSRR}\omega}{1 - L_{CSRR} C_{CSRR} \omega^2} - \frac{1}{C_{RH}\omega} \right)} \right). \quad (5.2)$$

As can be seen, the phase response has a nonlinear relation with respect to both the sensing capacitor ($C'_{v,MUT}$), and the frequency. In order to better show this nonlinear relation, the dispersion relation versus sensing capacitor is plotted for various frequencies in Fig. 5.2. Assuming that the initial value of $C'_{v,MUT}$ is 0.7 pF, for small capacitance

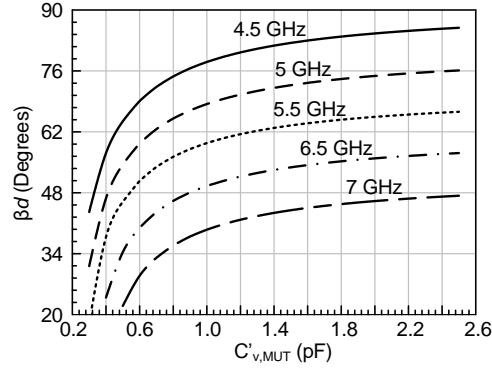


Figure 5.2: Dispersion relation with respect to the series capacitor ($C'_{v,MUT}$) at various frequencies (the parameter values are: $L_{RH} = 2.5$ nH, $C_{RH} = 1$ pF, $L_{CSRR} = 1.85$ nH, $C_{CSRR} = 1$ pF).

variations, the phase changes significantly at all the frequencies. However, for large variations of $C'_{v,MUT}$, the phase slope drops, and the phase response becomes less sensitive to this parameter. As a result, the CRLH TL-based sensor provides a higher sensitivity for detecting and characterization of MUTs with low dielectric constants (which cause small variations in $C'_{v,MUT}$ value), while it shows less sensitivity to MUTs with high dielectric constants (which result in large variations in $C'_{v,MUT}$ value). Moreover, it is noteworthy that the sensitivity of the sensor decreases at higher frequencies. This is mainly due to the operation region of the CRLH TL. At lower frequencies, where the TL is operating at the LH region, the effect of the series capacitor $C'_{v,MUT}$ is dominant. However, at higher frequencies, where the TL is in the RH region, the value of the impedance introduced by the series capacitor ($1/(C'_{v,MUT}\omega)$) drops, and the dominant parameter becomes the RH elements, the series inductor (L_{RH}), and the shunt capacitor (C_{RH}). As can be seen, the dispersion relation is still nonlinear in the RH region, and better sensitivity compared to conventional RH TLs can be achieved.

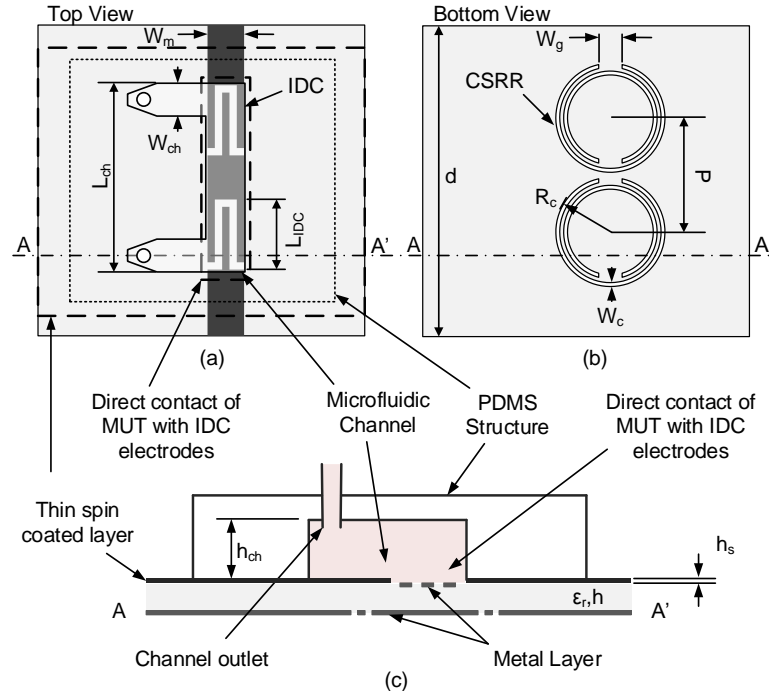


Figure 5.3: (a) Top, (b) bottom, and (c) A-A' cross-section views of the proposed CRLH TL-based fluidic sensor. The parameter values are: $W_m = 2.35$ mm, $W_{ch} = 2.5$ mm, $L_{ch} = 13.4$ mm, $h_{ch} = 3.5$ mm, $L_{IDC} = 5.5$ mm, $R_c = 3.5$ mm, $W_c = 0.25$ mm, $W_g = 2$ mm, $P = 7.35$ mm.

5.2.2 Sensing Element

5.2.2.1 Design Procedure

The top, bottom, and A-A' cross-section views of the designed sensor are shown in Fig. 5.3. The substrate used for this design is Rogers RT/Duroid 5880 ($\epsilon_r=2.2$, $\tan\delta=0.0009$, Rogers Corp., Brooklyn, CT, USA), with a thickness of $h = 0.787$ mm. The planar CRLH TL is constructed using a $50\text{-}\Omega$ microstrip line as the host medium. The IDC and the CSRR dimensions are adjusted to achieve the balanced condition, where there is no frequency band-gap between the LH and RH regions. As a result, due to the continuous transition from the LH to the RH region, the operational bandwidth is maximum for one unit-cell.

The sensitivity of metamaterial-inspired sensors is linearly proportional to the number

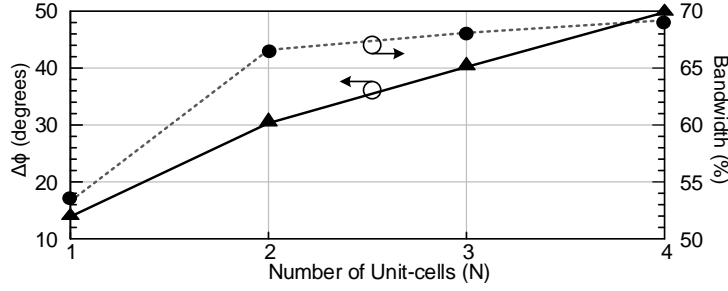


Figure 5.4: Sensitivity, and bandwidth of the proposed sensor with respect to the number of unit-cells at $f = 4$ GHz.

of unit-cells, and the relation can be written as follows,

$$\Delta\phi \sim N \cdot d \cdot \frac{\partial\beta}{\partial C'_{v,MUT}} \cdot \Delta C'_{v,MUT} \quad (5.3)$$

where, d , and N represent the length, and number of unit-cells, respectively. This equation suggests that a sensor with higher number of unit-cells provides a larger phase shift for a constant capacitance change. To further investigate this phenomenon, the capacitance (IDC) value is changed by modifying L_{IDC} from 5.5 mm to 3.5 mm, and the phase of the TL is extracted at each case. The resulting phase difference of the TL ($\Delta\phi$) due to this constant capacitance change (caused by ΔL_{IDC}) is calculated and shown in Fig. 5.4 for various number of unit-cells (N) at 4 GHz. As can be seen, the sensitivity of the proposed sensor to this constant capacitance variation increases linearly as the number of unit-cells increases. Moreover, the operational bandwidth versus N is plotted considering $L_{IDC} = 5.5$ mm, which shows slightly larger operational bandwidths are achievable as N increases. Therefore, two unit-cells are placed in series with a period of P , in order to increase the sensitivity, and the bandwidth. However, further increasing the number of unit-cells requires a larger volume of the MUT, and also increases the overall size of the sensor considerably.

A Polydimethylsiloxane (PDMS) structure with a fluidic-channel and in/out-lets is utilized to expose the sensing IDC to the MUT. The material is placed where the E-field concentration is maximum. The width, and length of the channel are set to cover both IDCs of the two unit-cells. A thin ($30 \mu\text{m}$) layer of pdms is spin coated and used to bond the pdms structure to the board [86, 87]. In order to measure the additional loss of the TL caused by the MUT, the liquid should touch the sensing electrodes directly. Otherwise, the losses of the spin-coated layer, and the PDMS structure are dominant, and the sensor's sensitivity is highly limited for characterizing the ϵ'' of the MUT. Therefore, unlike the sensor proposed in [25], a mask layer is used on top of the IDC electrodes during the spin-coating process, and as a result, the MUT can be directly placed on top of the IDC electrodes (see Fig. 5.3(c)). On the other hand, the resistive nature of the MUT is highly dependent on the sample volume [72]. Increasing the sample volume results in higher insertion losses for the TL. However, this dependency saturates for large enough volumes, and the insertion loss of the TL becomes independent of this parameter. Therefore, h_{ch} is set to 3.5 mm to provide enough sample volume on top of the sensor. The fabrication process of this fluidic structure is thoroughly discussed in Section 5.4.1.

5.2.2.2 Full-wave Simulations

In order to better study the interaction of the external electromagnetic field with the MUT, the E-field distribution on top metal layer at 4 GHz is extracted from High Frequency Structure Simulator (HFSS), and shown in Fig. 5.5(a) when the channel is filled with air. As can be seen, the E-field is mainly concentrated on top of the sensing IDCs. The B-B' side-view of the E-field distribution is shown in Fig. 5.5 (b) to better demonstrate the E-field penetration for when the channel is filled with air and ethanol. The liquid material disturbs this E-field due to its specific dielectric properties, which ultimately can be detected based on measuring the TL performance characteristics. The field perturbation

is shown in Fig. 5.5(c), where the E-field strength in the z -direction and at top of the IDC electrodes is plotted along the x -direction (B-B' line) at $f = 4$ GHz. The plotted curves are all at $\tau = 0$, where τ is the period of the E-field. It is observed that for each MUT, the TL has a unique E-field strength along the x -direction. Moreover, due to the additional loss of the MUTs, the E-field strength is lower for all the materials compared to the air at the position of the two IDCs. It is noteworthy that when the channel is filled with air, the maximum of E-field strength occurs at the position of the second IDC at $\tau = 0$. However, due to the additional phase shift caused by the MUTs, the maximum of the E-field strength is shifted back to the position of the first IDC.

The real part of the permittivity is a measure of how much energy is stored in the material as it is exposed to the external electric field. Therefore, the phase response of the sensing TL has the ϵ' information of the MUT. In order to better interpret this effect, the dispersion curve is plotted in Fig. 5.6 (a) for both the proposed CRLH TL, and conventional microstrip line-based sensors [75], when the channel is filled with various MUTs. Debye-based relaxation models of MUTs are imported into HFSS in order to take into account the frequency dependence of the dielectric constants in full-wave simulations [83, 84]. For both TLs, the phase response is shifted for each MUT as a result of different dielectric constant. However, the value of this phase variation is related to the sensitivity of the sensor. As shown in Fig. 5.6 (a), the CRLH TL sensor provides a significantly higher phase variation compared to the microstrip line sensor for a same material. This is evidence that the sensitivity of such structures are considerably higher than conventional TL-based sensors. Moreover, due to the continuous transition from the left- to the right-hand region (balanced condition), wide operational bandwidth of 4 - 8 GHz is achieved.

Fig. 5.6(b) shows the simulated phase of both the proposed CRLH TL, and the conventional microstrip line sensors at 5 GHz for different MUTs with respect to their dielectric

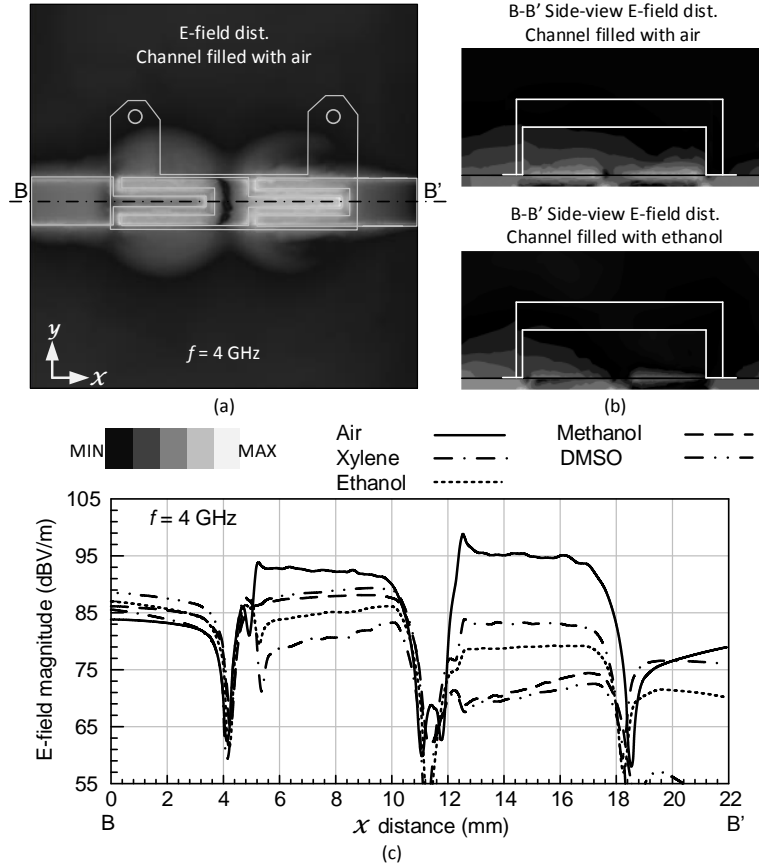


Figure 5.5: (a) Simulated E-field distribution of the proposed sensor when the channel is filled with air, (b) simulated e-field penetration into the channel (B-B' side-view) at 4 GHz when the channel is filled with air, and ethanol, (c) E-field strength along the x -direction (the B-B' line), extracting from full-wave simulations in HFSS at $\tau = 0$, where τ is the period of the E-field.

constant. The simulated data points are curve fitted to achieve a behavioral model for each sensor. As can be seen, the phase of microstrip line changes linearly (line: L_m) as loaded with MUTs with various dielectric constants. On the other hand, the CRLH TL-based sensor provides non-linear behavior, specially for MUTs with lower ϵ' values. The slope of the behavioral fitted curves defines the sensitivity of each sensor according to (5.3). In order to achieve a quantitative comparison between the two sensors' sensitivities, the non-linear behavior of the CRLH TL is piecewise linearly approximated, (lines: L_1 , L_2 , and

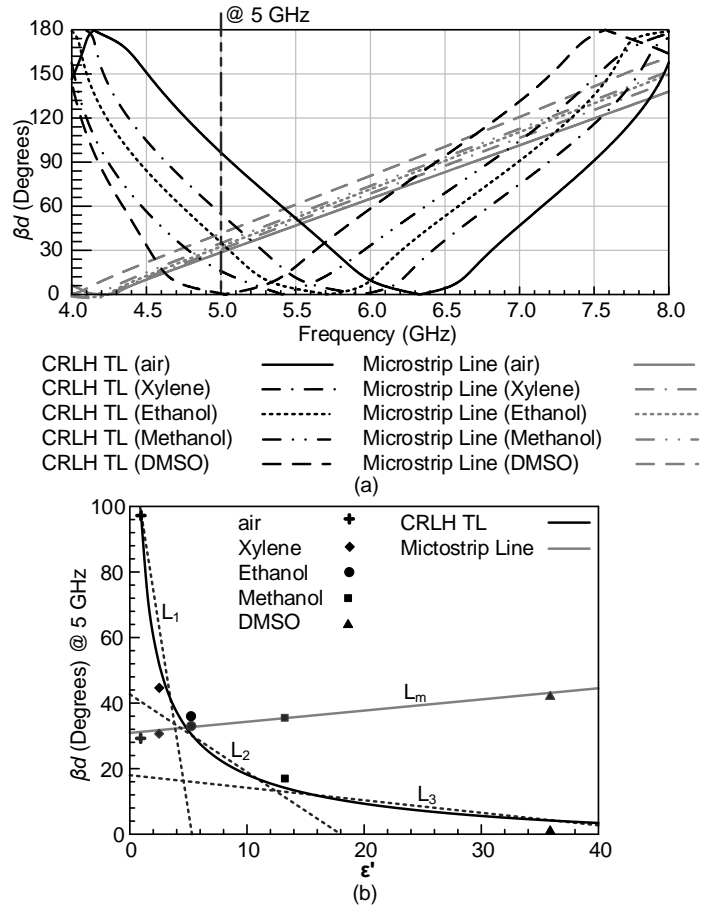


Figure 5.6: (a) Simulated dispersion curve of the proposed CRLH TL-based sensor for various MUTs, compared to Microstrip line sensor, (b) sensitivity comparison between the proposed CRLH-TL sensor, and the conventional microstrip line sensor using piecewise linear approximation, at $f = 5$ GHz.

L_3). Comparing these three lines with L_m , the proposed sensor's sensitivity is 82, 8.6, and 1.4 times the microstrip line sensitivity for $1 < \epsilon'_r < 7$, $7 < \epsilon'_r < 15$, and $\epsilon'_r > 15$, respectively. This improvement in the sensitivity, specially at low dielectric constants, makes the proposed sensor a good candidate for mixture detection applications such as binary mixtures sensing with very close dielectric constants (see Section 5.4.3).

On the other hand, the imaginary part of the dielectric constant describes the lossy behavior of the MUT, and is a measure of dissipation factor. As a result, the ϵ'' information

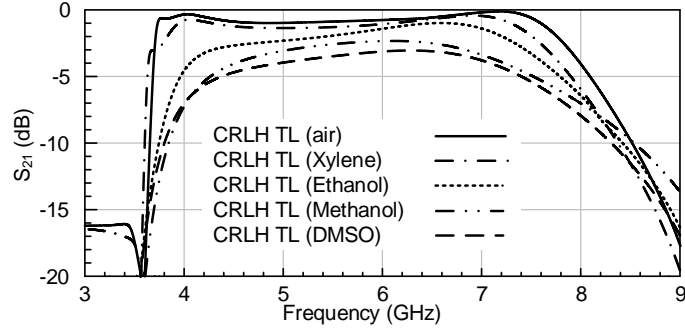


Figure 5.7: Simulated insertion loss of the proposed sensor for various MUTs.

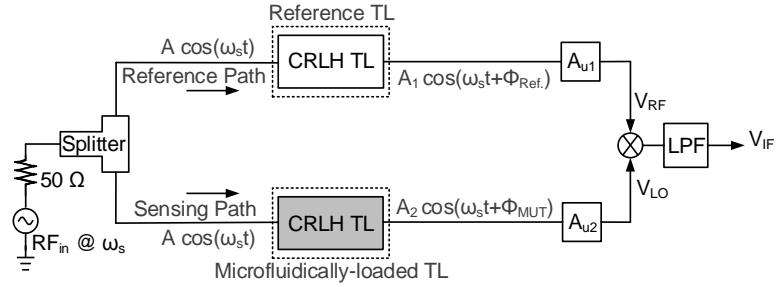


Figure 5.8: Block diagram of the interferometry-based system I design.

can be extracted from the insertion loss of the TL. Fig. 5.7 shows the simulated S_{21} of the proposed sensor for various MUTs. In this design, the liquid is in direct contact with the IDC electrodes, and the conductor, dielectric, and PDMS losses are all constant regardless of the material in fluidic channel. Therefore, the difference between the insertion losses is mainly due to the dissipation factor of the MUT. The presented CRLH TL-based sensor is a suitable choice for wideband microwave interferometric material characterization, due to its compact profile, wide operational bandwidth, and the improved sensitivity.

5.3 Interferometry System Design

5.3.1 System I

Fig. 5.8 shows the block diagram of the interferometric sensor first proposed in [25]. The circuit is excited with a single tone at ω_s . A power splitter is utilized to symmetrically divide the input signal into the upper (reference), and lower (sensing) paths. Two identical CRLH TL-based sensors are placed in both the traveling-wave paths. The fluidic channel in the upper path is empty (filled with air as the reference MUT), while the fluidic channel in lower path is filled with liquid MUT to construct the sensing element. It is shown in Fig. 5.6 that the phase response of the CRLH TL is altered due to the loading effect of each MUT. Due to this effect, the two symmetrically-divided signals in the two paths experience different phase responses as they travel through the two TLs, which results in a phase difference between the two. The interference occurs using a Zero-IF phase-detector architecture. The signals in the upper (reference), and lower (sensing) paths are connected to the RF, and LO inputs of the mixer, respectively. As the input signal is initially divided symmetrically, the amplitude of both the RF, and LO signals are approximately identical. The LO path requires a relatively large input signal amplitude to ensure abrupt switching and maximum conversion gain (or minimum conversion loss in case of a passive mixer). However, same amplitude for the RF input signal of the mixer could pass the P_{1dB} compression, and worsen the sensing capability. As a result, in order to accurately adjust the input signal amplitudes of both the RF and LO paths, two digitally-tunable attenuators are used before the mixer's RF and LO inputs.

As the LO amplitude is large enough to provide a high slew rate, and abrupt switching, the effect of the additional loss of the TL, caused by the liquid material, on the conversion gain of the mixer is negligible. Therefore, the IF DC-voltage at the output of the system mainly depends on the RF amplitude (A_1) and the phase deviation between the two paths

($\Delta\varphi = \varphi_{MUT} - \varphi_{Ref.}$). Higher-order modes are suppressed using a lowpass filter (LPF) at the output, and ultimately, a desktop multimeter is utilized for DC-voltage measurement.

The mismatches between the two paths cause offset DC-voltage at the output. Moreover, the output DC-voltage value has the information of A_1 . In order to eliminate the amplitude's (A_1) information from the output DC-voltage, and also remove the effect of any possible mismatch between the reference and sensing paths, the output IF voltage is normalized to the IF voltage of the system when both fluidic channels are filled with air as the reference MUT. As a result, the phase deviation at each frequency (ω_s) is calculated as follows:

$$\Delta\phi = \phi_{MUT} - \phi_{Ref.} = \text{Cos}^{-1} \left(\frac{V_{IF2}}{V_{IF1}} \right). \quad (5.4)$$

where, V_{IF1} is the output IF DC-voltage when both fluidic channels are filled with the reference MUT (air), and V_{IF2} represents the output IF DC-voltage when the sensing TL is loaded with the liquid MUT. By measuring this phase difference, the ϵ' of the MUT's dielectric constant can be extracted [25]. However, the information of the ϵ'' is lost, as the MUT is placed in the LO path, and the LO amplitude level is considered high enough to provide maximum conversion gain. Normalizing V_{IF2} to V_{IF1} , not only cancels out the amplitude difference effect, but also removes any other mismatch between the two paths that causes DC offset at the output. Therefore, high accuracy in measurement is achieved.

5.3.2 System II

In order to retrieve the ϵ'' information of the MUT using System I configuration, an additional step during the measurement procedure is required. In this step, the fluidic channel in the RF path is filled with the MUT, and the fluidic channel in the LO path is considered empty (filled with air). The output DC-voltage is named as V_{IF3} , and is mainly a function of the phase difference, and the amplitude of the RF path. The latter

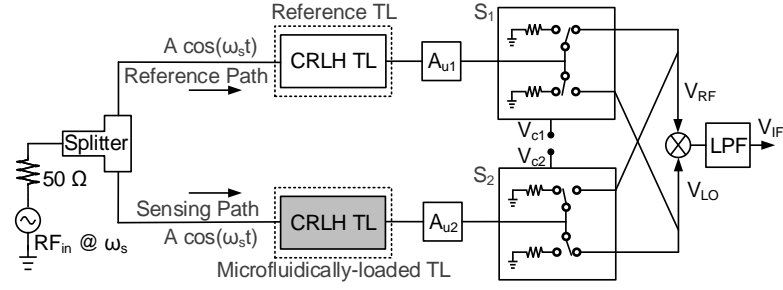


Figure 5.9: Block diagram of the interferometry-based system II design.

has the ϵ'' information as the additional insertion loss caused by the MUT changes the RF amplitude level. Similarly, in order to remove the effect of the phase difference ($\Delta\varphi$), and the mismatches between the two paths, V_{IF3} needs to be normalized to V_{IF2} , and the additional insertion loss due to each MUT is relative to this voltage ratio:

$$\frac{\alpha_{MUT}}{\alpha_{air}} \propto \frac{V_{IF2}}{V_{IF3}}, \quad (5.5)$$

where α_{MUT} , and α_{air} represent the insertion losses of the CRLH TL when loaded with MUT, and air, respectively. Also, the effect of the attenuators are neglected as their values are known. This method has a straight-forward procedure, however, it lacks enough reliability, as the MUT needs to be removed from one channel, and placed in another one. This displacement of the MUT between the two channels is undesirable for most applications, and might result in further measurement errors.

5.3.2.1 Design Procedure

Fig. 5.9 shows the proposed System II configuration, in which two voltage-controlled switches are employed in order to switch the LO and RF ports of the mixer rather than displacing the MUT between the two paths. In this case, first V_{IF1} is measured as both channels are empty (filled with the reference MUT). Afterwards, the sensing path is ex-

posed to the MUT. The sensing, and reference paths are connected to LO, and RF ports of the mixer, respectively, and V_{IF2} is measured. Also, the other output ports of S_1 and S_2 are matched to 50Ω . Finally, S_1 and S_2 are switched, and this time the reference, and sensing paths are connected to LO, and RF inputs of the mixer, respectively. Similarly, the other two output ports of the two switches are matched to 50Ω , and V_{IF3} is achieved as the output DC-voltage.

Similar to System I, assuming that the MUT is placed in the LO path, the LO amplitude needs to be large enough to ensure hard switching, even in case of additional loss due to the MUT. According to the data-sheet of the mixer used in this design (see Section 5.4.1), the LO power of $> +9$ dBm is required for hard switching. Therefore, the input power is chosen 18 dBm to ensure that after 3 dB drop over the Wilkinson power divider, 5 dB additional loss of the TL due to the MUT for the worst case scenario (see Fig. 5.7), and 1 dB insertion loss for the SPDT switch (see Section 5.4.1), still the input signal at the LO port of the mixer is greater than +9 dBm. On the other hand, the channel in the RF path is filled with air, and the RF power is adjusted using the attenuator (A_{u1}) to be less than the P_{1dB} compression point of the mixer (10 dBm for the employed mixer in this design), and kept the same during the measurement of all the MUTs. The amplitude mismatch and any other mismatches between the two paths cause DC offset at the output similar to System I. However, by normalizing the measured value, V_{IF2} , to this DC offset voltage, V_{IF1} , the mismatch effect is canceled out, and high accuracy can be achieved.

By switching the outputs of the SPDT switches, the MUT is placed in the RF path this time, and the additional loss of the TL, caused by MUT, reduces the RF input power, and therefore, the conversion gain of the mixer drops. In this case, the LO power is again large enough to ensure hard switching. The phase difference between the two paths remains the same, since the two paths are still identical except that one fluidic channel is filled with air, and the other is filled with MUT. In this case, the output DC voltage, V_{IF3} , is related to

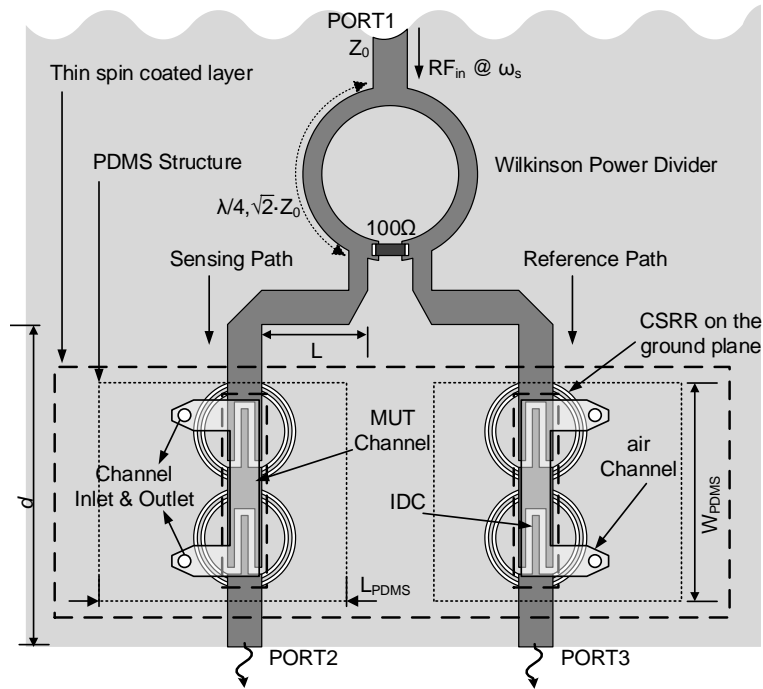


Figure 5.10: Top view of the Wilkinson power divider, and the two reference, and sensing paths.

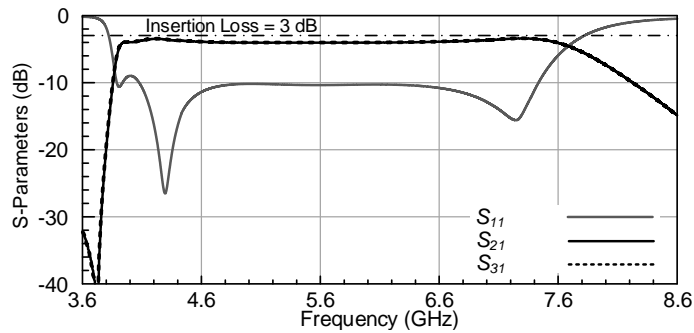


Figure 5.11: Simulated S-parameters of the power divider, and the two reference, and sensing paths, when both the channels are filled with air.

both the amplitude and phase differences between the two paths. Using (5.5), and dividing V_{IF3} to V_{IF2} , the part of the output related to the phase difference is canceled out, and the result is only due to the amplitude difference between the two paths.

Fig. 5.10 shows the power splitter, and the two traveling-wave paths constructed using a distributed Wilkinson power divider, and two proposed CRLH TL-based sensors. The Wilkinson power divider provides equal power division in a broad BW from 1 - 10 GHz. Moreover, its two outputs are 50Ω microstrip lines, and there is no need for a matching network between the splitter and the two CRLH TLs. Fig. 5.11 shows the simulated S-parameters of the structure shown in Fig. 5.10, considering PORT1 as the input port, and PORT2, and 3 as the two output ports. Assuming both channels are filled with air, the closer S_{21} , and S_{31} values are, the less mismatches exist between the reference, and sensing paths. As can be seen, the simulated S_{21} , and S_{31} are very close (somehow identical), and the mismatches between the two paths are minimum. The proposed System II configuration is more reliable, and provides complex dielectric-constant characterization of MUT.

5.3.2.2 *Non-idealities*

5.3.2.2.1 *Leakage* Ideally, the two signals in reference and sensing paths have no interaction before the interference occurs. However, in practice, there is always a leakage from one path to the other, which can distort the two signals, and result in measurement errors. Therefore, the effect of this leakage needs to be minimized during the design procedure. In the proposed System II configuration; (1) there is a leakage from one CRLH TL to the other through the substrate. Also, there is an undesired mutual coupling between the two CRLH TLs as well, (2) the switches S_1 and S_2 are not ideal, and there is a leakage from one state of the switch to the other, and (3), the RF-LO leakage of the mixer needs to be taken into account. The two latter cases, (2), and (3), are less of importance as their effect can be minimized by choosing off-the-shelf components with high isolation levels (see Section 5.4). According to the data sheets, the isolation between the two states of the employed switch is $>42\text{dB}$, and the mixer provides $>40 \text{ dB}$ LO-RF isolation in this design.

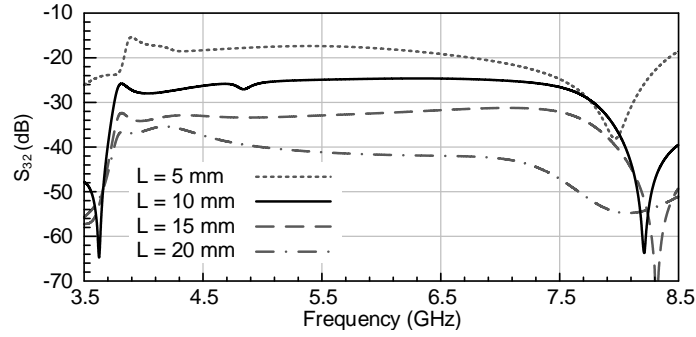


Figure 5.12: Simulated S_{32} of the structure shown in Fig. 5.10, when both the channels are filled with air.

On the other hand, the former, (1), is minimized in the design process. The main parameter that affects the amount of leakage between the two TLs is the distance (L) between them. In order to better study the effect of this parameter, simulated S_{32} of the structure shown in Fig. 5.10 is plotted in Fig. 5.12. By increasing the distance, the amount of leakage between the two paths reduces. However, very large values of L increases the overall size of the sensor. Due to this trade-off, L is chosen 10 mm to provide better than 25 dB of isolation between the two CRLH TLs and achieve a reasonably small structure.

5.3.2.2.2 Temperature Variation The dielectric properties of materials in the microwave region are dependent on temperature. This is shown for ethanol in Fig. 5.13, where its ϵ' , and ϵ'' are plotted at various temperatures using Debye- Γ relaxation model [83]. The measurement setup of the proposed method is assumed to be at room temperature ($T = 25^\circ C$). However, as the MUT is exposed to an alternating electromagnetic field on top of the IDC electrodes, its temperature slightly increases due to the molecular dipole rotation within the dielectric material. Therefore, the dielectric constant of the MUT deviates from its value at $T = 25^\circ C$. As this temperature increase is related to the loss of the material, the error caused by this effect is more important in ϵ'' measurement. For instance, according to Fig. 5.13, for $1^\circ C$ change in the temperature, the ϵ' , and ϵ'' of ethanol deviate

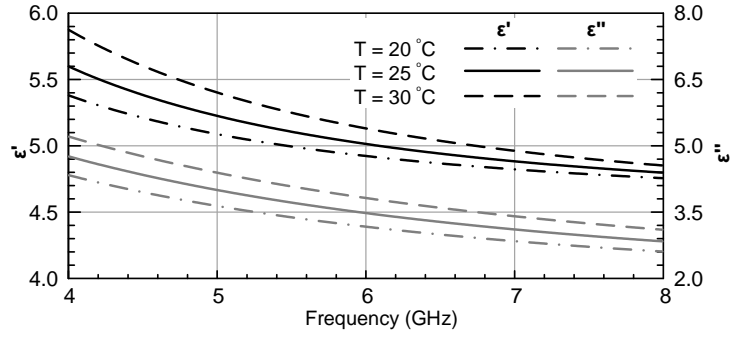


Figure 5.13: Ethanol's dielectric properties at various temperatures (ϵ' , and ϵ'' are plotted using Debye– Γ relaxation model [83]).

by roughly 0.2%, and 1.2%, respectively. In order to study the effect of this error on the sensing performance of the proposed method, the temperature of the channel is measured under test condition and at the steady-state for maximum input power level of 18 dBm, and the results are discussed in Section 5.4.

5.3.2.2.3 Impedance Mismatch Since the effect of the MUT on the sensing CRLH TL can be considered as capacitive loading, the matching of the TL varies based on the dielectric properties of the MUT. In case of significant mismatch, the reflected wave can distort the main signal, and therefore, the DC-voltage readout at the output is unreliable, and the significant error makes material characterization highly inaccurate. Therefore, either the TL's mismatch for a broad range of dielectric constants needs to be negligible, or a matching network (or an isolator) is required between the TL, and the attenuators. In order to better show the effect of various MUTs with broad range of dielectric constants on the proposed CRLH TL sensor, the return loss of PORT3 in Fig. 5.10 is shown in Fig. 5.14. As can be seen, although the right- and left-handed resonance frequencies vary for each MUT, the S_{33} remains below -10 dB over the desired frequency bandwidth, meaning that there is no need for a matching network or an isolator between the attenuators, and the TLs. This is beneficial since it reduces the complexity of the design, and also results

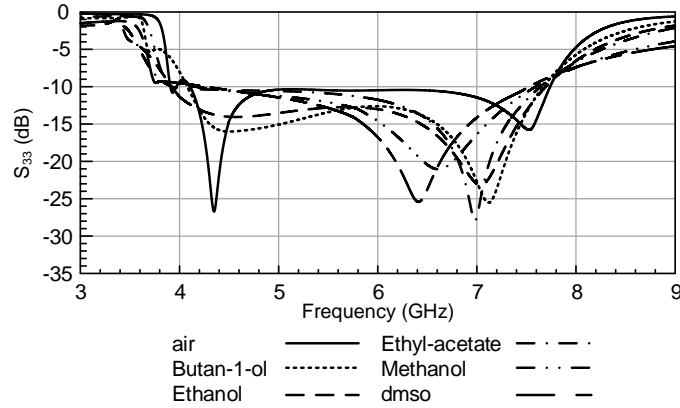


Figure 5.14: The return loss (S_{33}) of the sensing CRLH TL shown in Fig. 5.10.

in a more compact test board.

5.3.2.2.4 Fabrication Tolerances As discussed in Section 5.3, normalizing V_{IF2} to V_{IF1} , and V_{IF3} to V_{IF2} , not only cancels out the amplitude difference (between the RF and LO paths) effect, but also removes any other mismatch between the two paths effect that causes DC offset at the output. Therefore, the proposed method remains accurate even in case of fabrication tolerances, and mismatches between the two paths. In order to take into account all the experimental issues, and practical considerations, the measured s-parameters of all the ICs, provided by the manufacturer, are used in system-level simulations in Advanced Design System (ADS), while the Wilkinson power divider, and the transmission lines s-parameters are extracted from HFSS. The printed circuit board (PCB) fabrication tolerance in this design is $\pm 1 \text{ mil}$ ($\sim 25 \mu\text{m}$), while the fluidic channel's tolerance is $< \pm 50 \mu\text{m}$ [87]. The effect of these tolerances on the sensor's performance is negligible. The S-parameters of the ICs are also imported into HFSS, and therefore, a full-wave model for the ICs are achieved based on the measured results provided by the manufacturer. The final board, including the passives, fluidics, and the electronics is full-wave simulated in HFSS as well.

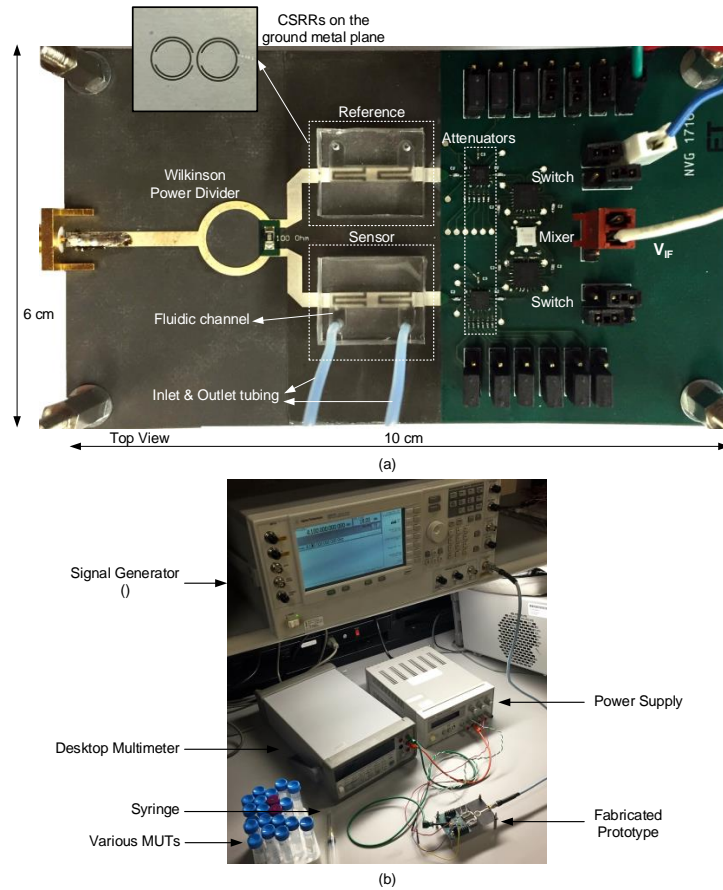


Figure 5.15: (a) Top view of the fabricated interferometry-based sensor, (b) the complete experimental setup including the instrumentations.

5.4 Implementation and Experimental Results

5.4.1 Fabrication

The proposed miniature interferometry sensor is fabricated and shown in Fig. 5.15 (a). The complete setup including the instrumentations is shown in 5.15 (b). The procedure, presented in [25], is modified to make the IDC electrodes be in direct contact with the MUT. Fig. 5.16 shows the step-by-step fabrication procedure. First, the top and bottom metal layers are etched based on common PCB technology (Step 1). Afterwards, the fluidic section is fabricated based on 3D printing and standard soft lithography techniques

[86]. Reusable 3D molds are designed in SolidWorks, and printed layer by layer using a high-resolution 3D printer called EnvisionTec Perfactory Micro (Step 2). The molds are washed with isopropyl alcohol and dried in oven at 65°C for 24 hours to remove any chemicals before the actual use. A liquid solution of PDMS is prepared by mixing Sylgard 184 (from Dow Corning) in a 10:1 resin to curing agent weight ratio, and de-gassed to remove any bubbles. The PDMS solution is poured in molds and heat cured in oven at 65°C for at least 2 hours (Step 3). Once the PDMS cures, it becomes solid and is peeled from the molds. At this step, the fabricated PDMS structures contain the required fluidic channels on their bottom sides, and the in-, out-lets are achieved by punching holes through the PDMS. (Step 4).

Since the PDMS can bond to itself, a thin intermediate layer of PDMS is used to attach the fabricated PDMS structures with fluidic channels to the circuit board. The thin deposited PDMS layer should not cover the sensing electrodes in order to make the direct contact between the sensor and MUT feasible. Therefore, a piece of Scotch tape is fixed on top of IDC electrodes to act as a temporary sacrificial layer which can be later removed (Step 5). The tape is carefully patterned and cut using a blade. The excess tape is removed such that the attached tape only covers the sensing electrodes (Step 6). Similarly, the sacrificial layer is also used to cover the electronics part of the circuit board. Then, a thin film of PDMS (30 μm) is deposited on the board using a spin-coater, spinning at 2600 RPM for 30 seconds, and heat cured at 65°C for 2 hours (Step 7). After PDMS thin-film becomes solid, another very thin layer (2-3 μm) of liquid PDMS is spin-coated at 6000 RPM for 10 minutes, to act as an adhesive layer between the circuit board and channel structures. Afterwards, the sacrificial layer is peeled off, while the rest of the board is covered by the PDMS adhesive layer for bonding (Step 8).

The circuit board containing the liquid PDMS adhesive layer is brought into contact with the two solid PDMS structures that are aligned such that channels completely cover

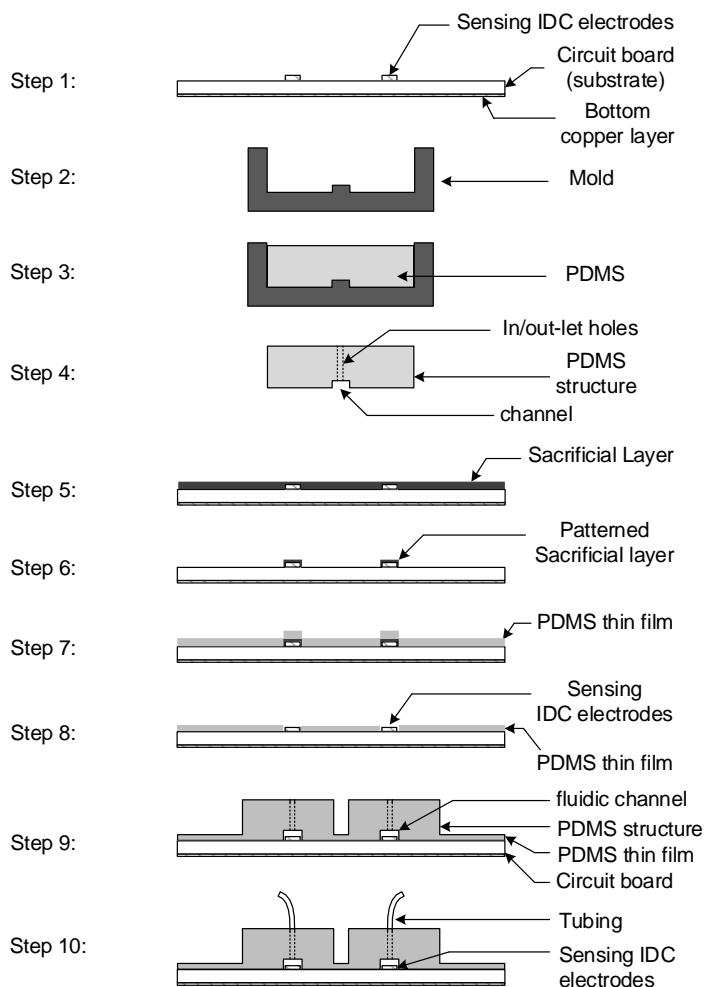


Figure 5.16: Step-by-step process showing side view for fabrication of the interferometry-based sensor using 3D printed mold and soft lithography.

the sensing electrodes (Step 9). After alignment, the circuit board is placed on a hot plate. While pressing both the PDMS structures against the circuit board, the hot plate is heated to 130°C to quickly solidify the adhesive PDMS layer. As a result, the PDMS channel structures and the thin spin-coated layer are bonded to each other, and attached to the circuit board. The tubing is connected to the inlet and outlet of channels (Step 10). Finally, the sacrificial layer is removed from the electronics part of the circuit board, and all the electrical connections are made to achieve an integrated device with fluidic and electron-

ics on the same board. Two 6-bit digitally-tunable attenuators (HMC425LP3), two non-reflective switches (HMC232ALP4E), and a double balanced mixer (HMC1048LC3B) from Analog Devices (Analog Devices, Inc., Chelmsford, MA, USA) are utilized to implement the presented interferometry-based dielectric spectroscopy system.

5.4.2 Calibration, Measurement, and Post-Processing

The DC voltages, V_{IF1} , V_{IF2} , and V_{IF3} , are measured for eight materials (air, xylene, butan-1-ol, propan-1-ol, ethanol, ethyl acetate, ethanediol, methanol, and dmsol), using a multimeter in the operational bandwidth of 4 - 8 GHz with a resolution of 100 MHz. The measurement is repeated four times for all the eight materials, and the measured data is averaged. Fig. 5.17 (a) shows the simulated (lines), and average measured (symbols) phase difference ($\Delta\phi$) for various MUTs. In order to better show the deviation in each measurement trial, the error bars of three shots of Fig. 5.17 (a) are captured, zoomed-in, and shown in Fig. 5.17 (b), (c), and (d). Moreover, the sensor shows larger phase shifts ($>12^\circ$) for each MUT compared to the measurement results reported in [25]. This is mainly due to the fact that, unlike [25], the MUT is in direct contact with the sensing electrodes, and as a result, the sensitivity of the proposed sensor is improved. On the other hand, Fig. 5.17 (e) shows the simulated (lines), and averaged measured (symbols) IL fraction (V_{IF2}/V_{IF3}) for the eight MUTs. Similarly, the error bars achieved from four measurement trials are captured for three shots of Fig. 5.17 (e), and shown in Fig. 5.17 (f), (g), and (h). As shown in these plots, good agreement between the simulated and measured results are achieved.

In order to verify that the measured data are at roughly same temperature of the theoretical models used in simulations, and study the effect of the temperature variation on the sensing error, the temperature of the channel is measured in the steady-state using a Fluke Ti-45 Infrared camera, while the power level of the input-signal is set to maximum ($P_{in} =$

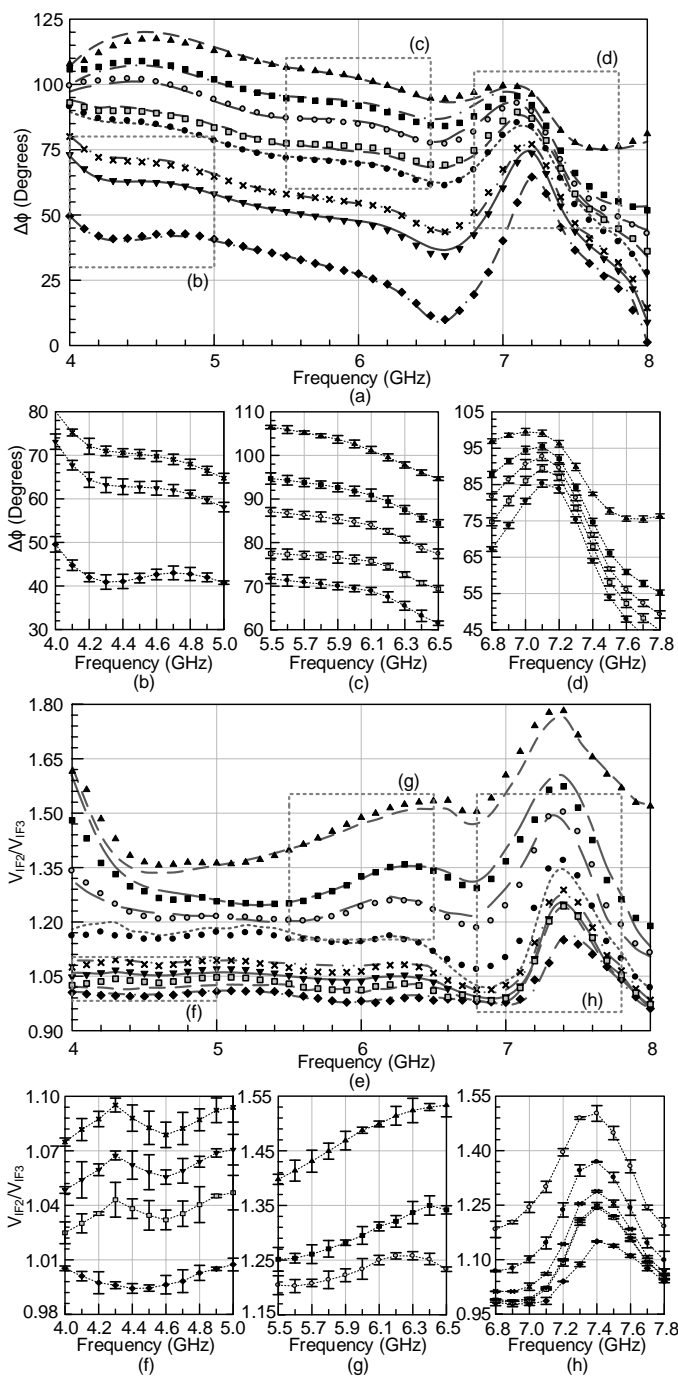


Figure 5.17: (a) Simulated (lines), and measured (symbols) $\Delta\phi$ values for xylene (first from bottom), butan-1-ol, propan-1-ol, ethanol, ethyl acetate, ethanediol, methanol, and dmsol (first from top), (b), (c), (d) zoomed measured $\Delta\phi$ values including the error bars resulting from four rounds of measurements, (e) Simulated (lines), and measured (symbols) V_{IF2}/V_{IF3} values for xylene (first from bottom), ethyl acetate, butan-1-ol, propan-1-ol, ethanol, ethanediol, methanol, and dmsol (first from top). (f), (g), (h) zoomed measured V_{IF2}/V_{IF3} values including the error bars resulting from four rounds of measurements.

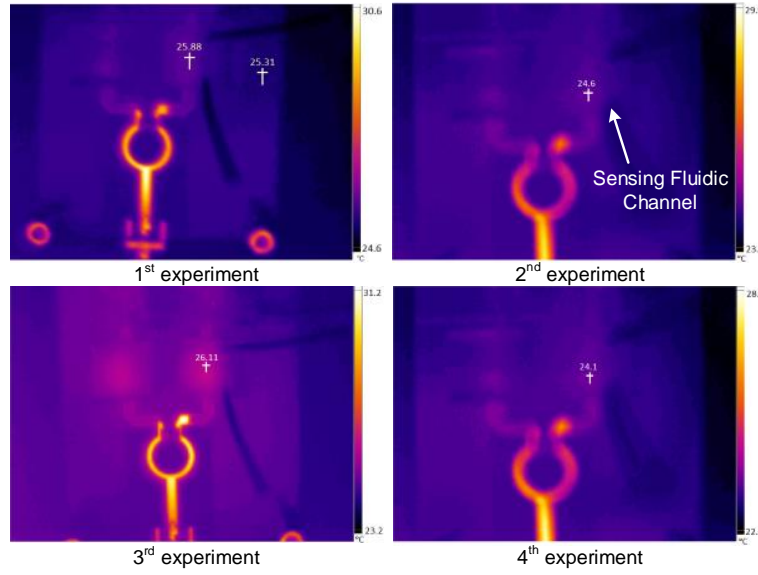


Figure 5.18: Measured steady-state temperature of the proposed sensor (at 4.5 GHz) during four rounds of measurements, while the sensing channel is filled with ethanol. The excitation port of the sensor is placed on the bottom side of these pictures.

18 dBm). The error bars shown in Fig. 5.17 also include the effect of temperature variation during each round of measurement. The temperature measurement is done for all the four experiments, and therefore, the slight temperature variation, that is partly responsible for the error bars in Fig. 5.17, is quantified. Fig. 5.18 shows the measured steady-state temperature of the proposed sensor at 4.5 GHz for the four measurement trials, when the channel is filled with ethanol. In this case, the temperature at the position of the sensing channel is 25.88°C, 24.6°C, 26.11°C, and 24.1°C, for the four experiments, respectively. Considering all the available measured data points, the average temperature change in the channel for different MUTs is roughly 0.56°C compared to the room temperature.

In order to relate the measured $\Delta\phi$, and V_{IF2}/V_{IF3} to ϵ'_r , and ϵ''_r of the MUT, respectively, a calibration is required at each measurement frequency [19, 25]. This is necessary because the CRLH TL has a nonlinear relation with respect to the frequency, and also the conversion gain of the mixer (or conversion loss in case of a passive mixer) is frequency-

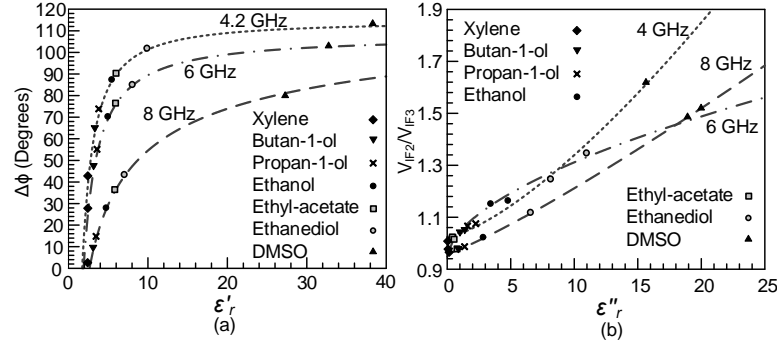


Figure 5.19: Measured (a) $\Delta\phi$ and (b) amplitude fraction for the calibration materials as functions of ϵ'_r , and ϵ''_r , respectively, with the power fitted curves (dashed lines).

dependent, and therefore, the values of $\Delta\phi$, and V_{IF2}/V_{IF3} vary at each frequency even if the MUT has a constant dielectric response at all frequencies.

First, $\Delta\phi$, and V_{IF2}/V_{IF3} are measured (for four times, and averaged) for xylene, butan-1-ol, propan-1-ol, ethyl acetate, ethanol, ethanediol, and dmsol, while their dielectric constants (both ϵ'_r , and ϵ''_r) are assumed to be known in the operational frequency band. These liquids are chosen as calibration materials as they cover a broad range of dielectric constants. Since the sensitivity of the proposed sensor is roughly 80 times a conventional TL for MUTs with $\epsilon'_r < 15$, it is important to have enough number of calibration materials with their ϵ'_r in this range. Otherwise, extra error due to inaccurate calibration causes higher uncertainty in sensing. Afterwards, the average measured $\Delta\phi$, and V_{IF2}/V_{IF3} values are curve-fitted to ϵ'_r , and ϵ''_r , respectively, at each frequency using power functions of order two. This is shown in Fig. 5.19, where both the measured data of calibration materials (symbols), and fitted curves (dashed lines) are shown for 4, 6, and 8 GHz. The behavioral equations for $\Delta\phi$, and V_{IF2}/V_{IF3} are given by

$$\Delta\phi = a_1 \times \epsilon_r^{a_2} + a_3, \quad (5.6)$$

$$V_{IF2}/V_{IF3} = b_1 \times \epsilon_r^{b_2} + b_3, \quad (5.7)$$

where a_i , and b_i , $1 \leq i \leq 3$ are the frequency-dependent fit parameters ($a_1 = -225.8829$, -213.0669 , -200.5506 , $a_2 = -1.2303$, -1.0642 , -0.3708 , $a_3 = 114.6339$, 107.8364 , 139.9488 , $b_1 = 0.01288$, 0.098 , 0.0178 , $b_2 = 1.389$, 0.5699 , 1.1515 , and $b_3 = 1.024$, 0.9476 , 0.9595 , at 4, 6, and 8 GHz, respectively). As can be seen, the fitted curves are functions of both the dielectric constant of the MUT, and the frequency. In order to better show the overall behavioral model of the presented sensor, 3D fitted curves of $\Delta\phi$, and V_{IF2}/V_{IF3} are plotted versus frequency and dielectric constant, and shown in Fig. 5.20. It is noteworthy that $\Delta\phi$ fitted curves show higher sensitivity specially for materials with lower ϵ_r' values, and the non-linearity behavior is similar to what was expected from both theory shown in Fig. 5.2, and simulation shown in Fig. 5.6 (b). On the other hand, as the additional loss of the MUT increases the IL of the TL, the 3D fitted curve of V_{IF2}/V_{IF3} shows same trend.

Finally, both ϵ_r' , and ϵ_r'' of an unknown MUT are extracted by measuring its $\Delta\phi$, and V_{IF2}/V_{IF3} , and using equations 5.6, and 5.7, respectively, at each frequency. Fig. 5.21 shows the theoretical (solid line), and measured (symbols) dielectric responses of methanol. Comparing the extracted values with a 100 MHz resolution with the theoretical values at $T = 25^\circ\text{C}$ from 4.2 - 8 GHz, the MSE of the proposed system is $\sim 1.1\%$, and $\sim 1.6\%$ for ϵ_r' , and ϵ_r'' of methanol, respectively. Part of this error comes from the temperature variation in the fluidic channel compared to the theoretical model at room temperature. The measured average temperature variation of 0.56°C mostly affects the loss factor of the MUT, and therefore causes error in ϵ_r'' measurement. However, as discussed in Section III, this error is negligible for ϵ_r' measurement. Moreover, another part of this error is mainly due to the accuracy of the curve-fitting process. Having more known materials for calibration procedure increases the accuracy of the curve-fitting, and therefore, a better behavioral model for the sensor can be achieved.

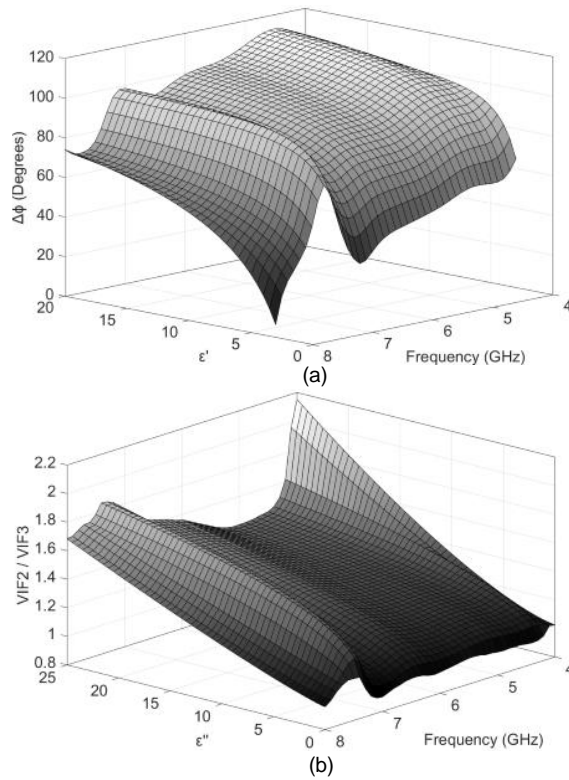


Figure 5.20: 3D plots of the fitted curves, (a) $\Delta\phi$ and (b) amplitude fraction versus the frequency and ϵ' , and ϵ'' , respectively.

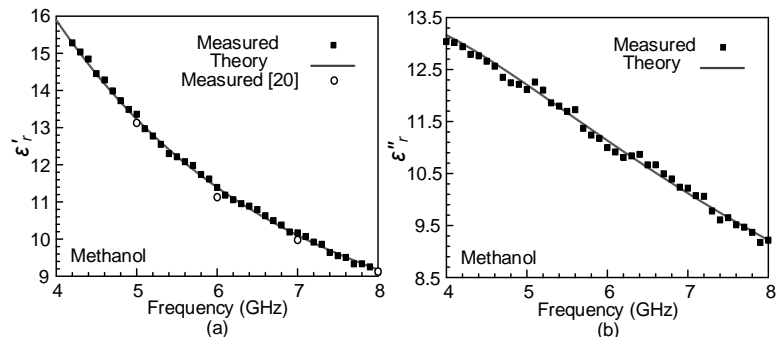


Figure 5.21: Measured permittivities versus frequency for methanol. The results are compared to theoretical values, and also measured data points from [20].

Furthermore, the theoretical models presented in [83, 84] are extrapolated from measured data points at various temperatures. The measurement results reported in these two references also have their own errors in reading, which eventually affects the accuracy of the presented theoretical models. As a result, part of the error reported in this work is due to the theoretical models, but not the actual measured data points. In order to have a better comparison, the measured methanol's ϵ' data points in [20] are also shown in Fig. 5.21 at 5, 6, 7, and 8 GHz. The method used in [20] is based on coaxial-line reflection coefficient measurement, and the error for methanol, given as the magnitude of the difference between the measured and calculated reflection coefficients, is reported as 2-4% at 10 GHz. As can be seen, the measured results achieved using the presented interferometry sensor are in good agreement with the previously published measured results for the same material.

5.4.3 Binary Mixture Characterization

The proposed interferometry-based dielectric spectroscopy system is utilized to characterize binary mixture of liquids. There are several formulations to model the effective dielectric constant of a binary mixture [88]. However, the Maxwell Garnett model is usually used due to its simple appearance combined with its broad applicability [72]. In this case, mixing two liquids with dielectric constants of ϵ'_1 , and ϵ'_2 , and mixing ratios of $1 - k$, and k , respectively, while $0 \leq k \leq 1$, results in an effective dielectric constant given by [88],

$$\epsilon_{eff} = \epsilon'_1 + 3 k \epsilon'_1 \cdot \frac{\epsilon'_2 - \epsilon'_1}{\epsilon'_2 + 2 \epsilon'_1 - k (\epsilon'_2 - \epsilon'_1)}. \quad (5.8)$$

The procedure starts with preparing the binary mixture by mixing proportional volumes of two liquids using micropipette. Afterwards, the DC voltages V_{IF1} , and V_{IF2} are measured for each fractional volume of the mixture as a separate MUT. Extracting $\Delta\phi$, and using (5.6) at each frequency (the behavioral model shown in Fig. 5.20), the effective

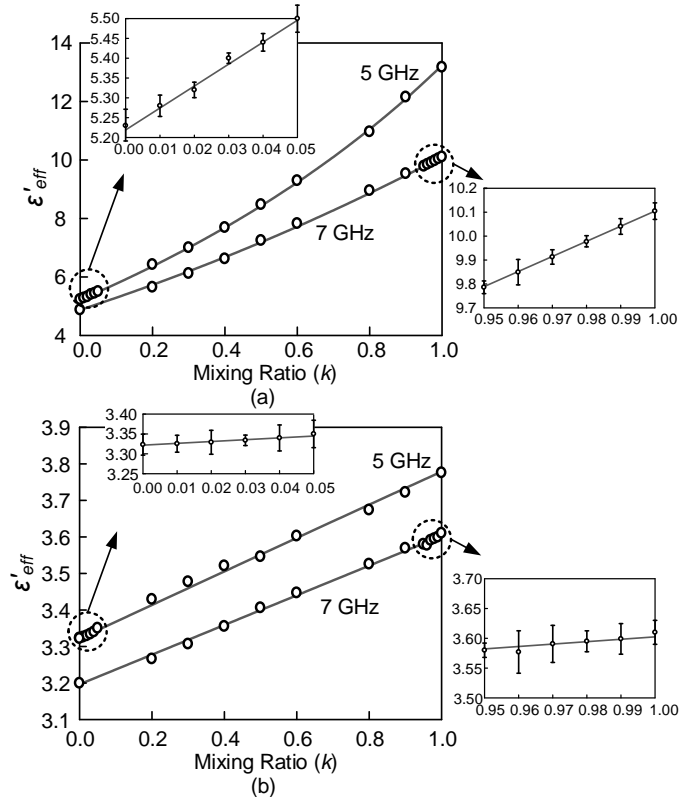


Figure 5.22: Measured and theoretical permittivities versus the mixing ratio (k) for binary mixtures of (a) ethanol/methanol, and (b) butan-1-ol/propan-1-ol at 5 and 7 GHz with zoomed views for $0 \leq k \leq 0.05$ at 5 GHz and $0.95 \leq k \leq 1$ at 7 GHz.

dielectric constant of each mixture with different fractional volume is detected. Fig. 5.22 (a) shows the measured ϵ_{eff} of ethanol/methanol mixture versus the mixing ratios at 5, and 7 GHz, respectively, compared to the Maxwell Garnett mixture model. The measured data in this figure is the average of four rounds of measurements. Moreover, zoomed portion of ϵ_{eff} is also shown for mixing ratios of $0 \leq k \leq 0.05$, and $0.95 \leq k \leq 1$ at 5, and 7 GHz, respectively, including the error bars resulted from four measurement trials. The binary mixtures are characterized based on ϵ_{eff} measurement with a MSE of less than 1%, and fractional volume (k) accuracy of 1%.

Although, ethanol/methanol mixture characterization is widely implemented [72, 75],

detecting binary mixtures of materials that have very close dielectric constants, especially at $\epsilon_r' \leq 10$, is challenging. Such application requires high sensitivity (or resolution), and accuracy over a broad bandwidth for the dielectric spectroscopy system. In order to better show the sensitivity improvement, achieved due to use of CRLH TL as the sensing element in the proposed work, the binary mixture of butan-1-ol/propan-1-ol is characterized, and compared to the Maxwell Garnett mixture model in Fig. 5.22 (b). Similarly, the measured data points are averaged after four rounds of measurements, and the error bars are shown for zoomed portion of ϵ_{eff} in the range of $0 \leq k \leq 0.05$, and $0.95 \leq k \leq 1$ at 5, and 7 GHz, respectively. As can be seen, such mixture characterization requires the sensing system to accurately detect dielectric constants between 3.2 to 3.8 for various mixing ratios at different frequencies. In this case, the binary mixture is characterized with MSE of 1% comparing the average measured values with the Maxwell Garnett model.

5.4.4 Discussion

Related priorly-reported RF/microwave interferometry-based sensors, open-ended coaxial lines, and impedance spectrometers in literature are compared with the presented sensor in Table 5.1. The proposed method covers a wide bandwidth of 4.2-8 GHz, compared to [75], which requires bulky and expensive discrete tunable modules such as VNA, or [79], which operates at a single frequency of 2.3 GHz. Moreover, solely characterizing ϵ' of solid materials is achieved in [79, 82], while the presented sensor provides complex dielectric spectroscopy of liquid chemicals due to the proposed fluidic structure. As can be seen, the proposed method also provides improvement in accuracy in reading compared to [20, 24, 80, 82].

Table 5.1: Comparison of Related Works in Literature

	Sensor Type	Operating Frequency Range	Detection Capability	Measurement Technique	Error
[20]	Open-ended coaxial line	1-18 GHz	ϵ' , ϵ'' of liquids	VNA	2-4% for reflection coefficient measurement at 10 GHz (methanol)
[23]	CPW TL (interferometry configuration)	5.1 GHz	Viability detection of single cells	VNA	NA
[24]	Artificial coaxial TL filled with MUT as the dielectric material	1-50 GHz	ϵ' , ϵ'' of liquids	VNA	2-5% for ϵ' , 20-30% for ϵ'' (Simulated, NR for measured)
[75]	Microstrip & CPW TLs (interferometry configuration)	2 - 10 GHz *	ϵ' , ϵ'' of liquids	VNA	NR
[79]	8 unit-cells CRLH TL (interferometry configuration)	2.3 GHz	ϵ' of solids	Portable Power meter	NR
[80]	Open-ended coaxial line and a thin metamaterial substrate	10.8 GHz	ϵ' , ϵ'' of liquids	VNA	5% for ϵ' , NR for ϵ''
[82]	Single compound CSRR	1.4, 2.6, 4.4 GHz	ϵ' and thickness of solids	VNA	Avg. error of 5.05% for ϵ' , 4.32% for thickness
This Work	2 unit-cells CRLH TL (interferometry configuration)	4.2 - 8 GHz	ϵ' , ϵ'' of liquids	Multimeter	$MSE_{\epsilon'} \sim 1.1\%$, $MSE_{\epsilon''} \sim 1.6\%$ (methanol)

* The presented system in [75] is intrinsically narrowband, however, wideband setup is achieved using tunable bulky modules.

6. COMPACT CONTACT-LESS ULTRA WIDE BAND DIELECTRIC SPECTROSCOPY SENSOR

6.1 Introduction

Contact-less material characterization has multiple advantages compared with the contact-based counterpart specially when the MUT sample is in liquid form. First, having contact between a liquid and the sensing unit can make the sensor hardly re-usable. In this case, the sensing unit needs to be replaced after each measurement trial, which makes the contact-based approaches more expensive. On the other hand, in case of contact-less sensing, only the container carrying the MUT needs to be replaced, which is significantly more cost effective. Another advantage of having the MUT in a container, and performing the material characterization in contact-less fashion is that the user requires minimum special expertise to perform the experiment as the sensing unit remains the same in all measurement trials, and only the container and the MUT need to be changed. Moreover, in some cases, the material could be hazardous, i.e. acidic liquids, or it might leak to some other parts of the sensor circuitry, and therefore it damages the entire system electronics. As a result, contact-less sensing has attracted attention over the recent years.

Free-space techniques are commonly used for contact-less measurement of dielectric properties of materials [21, 27, 28, 89]. These techniques are mainly based on using two antennas placed in the far-field and faced to each other with the MUT in the middle. Horn antennas are most commonly utilized for this purpose [21]. In [89], two microstrip quasi-horn antennas are utilized for UWB sub-surface sensing suitable for ground penetrating

©2017 IEEE. Part of this chapter is reprinted, with permission from IEEE, "A UWB Near-field Contactless Sensor for Solid and Liquid Material Characterization," IEEE International Symposium on Antennas and Propagation (APS-URSI), Jun. 2017.

©2017 IEEE. Part of this chapter is reprinted, with permission from IEEE, "A 3-10 GHz Contact-less Complex Dielectric Spectroscopy System," IEEE International Microwave Symposium (IMS), Jul. 2017.

radar applications. The far-field techniques can also be implemented with a single antenna, and based on measuring the reflection back from the MUT [90]. In all these contact-less sensing approaches performed at microwave range, the antennas' dimensions, the required volume of the sample MUT, and the overall setup sizes are significantly large. Therefore, such systems are unable to characterize liquid materials with small volumes within few mm^3 range. In order to achieve a more compact contact-less setup size, with relatively lower volume of the MUT, free-space techniques are applied at millimeter-wave (mm-wave) range [27, 28]. Despite their smaller setup size, such systems are unable to characterize the materials at microwave frequencies, and as was mentioned before, many materials, i.e. biomaterials [69], are solely responsive at microwave range. As a result, a miniaturized UWB contact-less sensor performing at microwave range seems demanding.

A microwave ultra-wide-band (UWB) contactless sensor is proposed in this chapter, which is based on utilizing two printed Vivaldi antennas coupled in their radiative near-field. The MUT in middle perturbs the electromagnetic fields around the two coupled antennas, which ultimately is detected based on two-port phase measurement using a vector network analyzer (VNA). An in-depth study on the compact near-field contact-less sensing unit is also provided, and the application of the proposed sensor for liquid chemical detection, and solid dielectric slab thickness sensing are investigated.

6.2 Contact-less Sensor

In order to achieve contact-less broad-band microwave sensing with a compact setup size, and relatively low volume of the sample, near-field sensing is proposed as a solution. Fig. 6.1 (a) shows the conceptual setup of the proposed near-field solution. Two antennas are coupled in their near-field region while the MUT is placed in between. The setup is surrounded with absorbing materials (ECCOSORB AN) to provide an anechoic environment [90]. The near-field region of each antenna has two sub-regions; reactive,

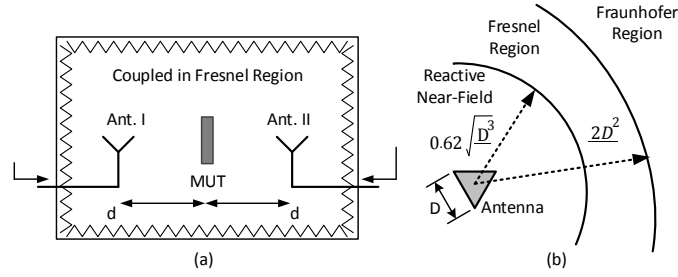


Figure 6.1: (a) The proposed conceptual contact-less sensor setup, (b) field regions of the antenna.

and radiative (Fresnel) regions. The former is in the immediate vicinity of the antenna, where the reactive fields predominate. In this case, the electric and magnetic fields are not necessarily in phase to each other, and the angular field distribution is highly dependent on the distance and direction away from the antenna. However, in the latter case the radiating fields predominate, and electric and magnetic fields are in phase. The angular field distribution in the Fresnel region still is highly dependent upon the distance from the antenna. In the proposed setup shown in Fig. 6.1(a), the distance between the two antennas (d) needs to be adjusted accurately, so that the two antennas are coupled to each other in their Fresnel regions, and therefore, have minimum effect on each other's return loss characteristics. As a result, the overall size of the setup depends on the targeted frequency range, antenna size, and its Fresnel region distance, which determines the value for d . Due to the complex electromagnetic field distribution in the Fresnel region full-wave simulations are required to finalize the overall dimensions of the setup adequately. The Fresnel region is commonly defined as follows [2]:

$$0.62 \sqrt{\frac{D^3}{\lambda}} < R < \frac{2D^2}{\lambda}, \quad (6.1)$$

where, D is the largest dimension of the antenna, and λ is the operating wavelength. The separation of regions is also shown in Fig. 6.1(b). Each MUT perturbs the near-field

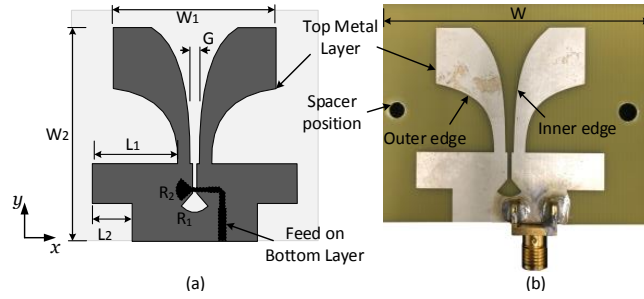


Figure 6.2: (a) Printed UWB antenna used for contact-less sensing, and (b) the top view of the fabricated antenna prototype. The parameter values are: $W = 41$ mm, $W_1 = 32.5$ mm, $W_2 = 42.7$ mm, $L_1 = 17.1$ mm, $L_2 = 8$ mm, $R_1 = 3.5$ mm, $R_2 = 2.85$ mm.

electromagnetic fields around the two coupled antennas based on its specific dielectric properties, which will be translated into phase and amplitude variations of S_{21} , and could be used for material detection and characterization.

The antenna type for the setup shown in Fig. 6.1(a) requires to satisfy two main criteria. First, the system design is based on covering the complete 3-10 GHz UWB frequency range. Therefore, impedance matching within this band is needed for the sensing antennas. Second, the antenna element needs to be non-dispersive in order to be able to detect the dispersive properties of solely the MUT. Otherwise, any dispersion caused from the sensor itself results in error in reading, and makes post processing and calibration even more cumbersome. As a result, the sensing antenna has to provide UWB operation with relatively constant group-delay over the entire band. In this setting, the Vivaldi antenna is one of the best candidates due to its broad bandwidth, low cross-polarization, and constant group delay. Fig. 6.2(a) shows the utilized printed UWB Vivaldi antenna first proposed in [91]. The antenna excitation, on the back side of the substrate, is a stepped microstrip line in order to cover the UWB frequency range. Both the inner and outer edges of the top metal patches are tapered to achieve the optimized group delay and impedance matching performance as discussed in [91].

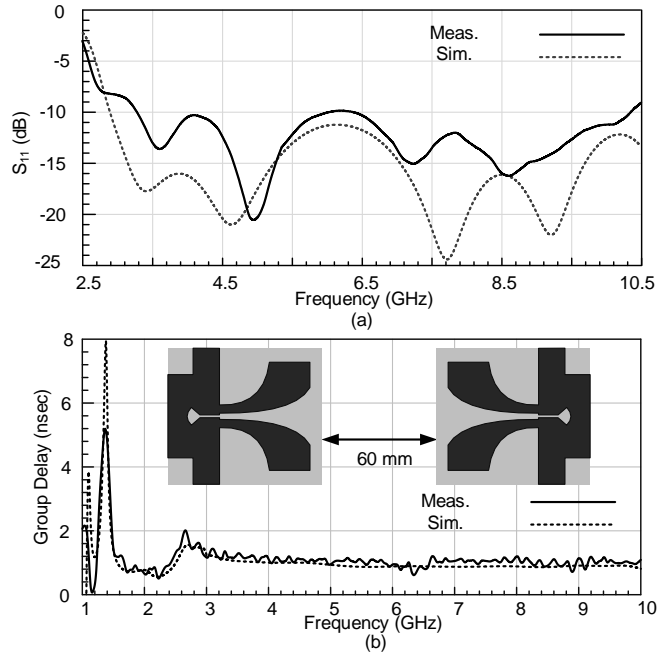


Figure 6.3: (a) Simulated and measured return loss characteristics of the utilized UWB Vivaldi antenna, and (b) simulated and measured group delay of the setup when the distance between the two antennas is $2d = 60$ mm.

The antenna is fabricated on FR-4 substrate with a dielectric constant of 4.4, and a thickness of 0.8 mm. Fig. 6.2(b) shows the fabricated prototype using common single-layer printed circuit board (PCB) technology. Fig. 6.3(a) shows the simulated and measured return losses of the designed Vivaldi antenna, which covers the interested bandwidth of 3-10 GHz. In order to extract the group delay of the utilized Vivaldi antenna in the proposed setup, first the distance between the two antennas (d) needs to be determined according to (6.1). The largest dimension of the utilized antenna is $D = 51.4$ mm, and the wavelength of the interested frequency range covers 3-10 cm. According to (6.1), and performing fine tuning simulations using Ansys High Frequency Structure Simulator (HFSS), the distance between the two antennas is chosen, $2d = 60$ mm, in order to couple the two antennas in their Fresnel regions while the mutual coupling and the MUT have negligible effects on the return loss characteristics of the two antennas. In this setting, the simulated

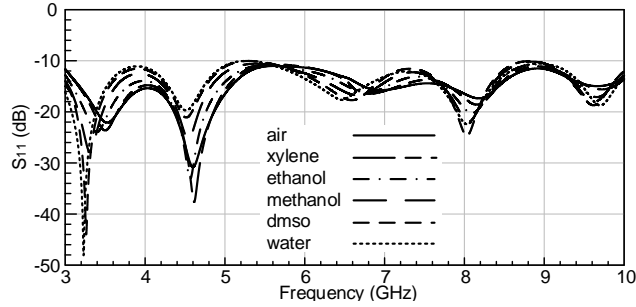


Figure 6.4: Simulated S_{11} of the setup when different MUTs are placed in between, and the distance between the two antennas is $2d = 60$ mm.

and measured group delay is extracted and shown in Fig. 6.3(b). The slight differences between the simulation and measurement is due to the tolerances between the SMA connector model in HFSS, and the actual SMA connector used in measurement. In order to better show that the two near-field coupled antennas remain matched to 50Ω regardless of the MUT in between, the simulated S_{11} response is plotted in Fig. 6.4 when different MUTs are placed in middle. Debye-based relaxation models of MUTs are imported into HFSS in order to take into account the frequency dependence of the dielectric constants in full-wave simulations [26]. As can be seen, the antenna element shows return losses better than 10 dB over the entire bandwidth for all the materials with a broad range of dielectric constants ($2.45 < \epsilon' < 75$ for xylene at 10 GHz as the minimum and water at 3 GHz as the maximum, and $0.045 < \epsilon'' < 30$ for xylene at 3 GHz as the minimum and water at 10 GHz as the maximum).

Another important factor in the proposed contact-less setup is the container used to place the liquid MUT in between the two antennas. Since the proposed setup is based on sensing in the Fresnel region in a controlled environment, the shape, dimensions, and the material of the container also require to be designed and set for all the measurement trials. At the same time, the container needs to be low-cost in order to make inexpensive repeating of the measurement for various MUTs feasible. The required volume of the sample can

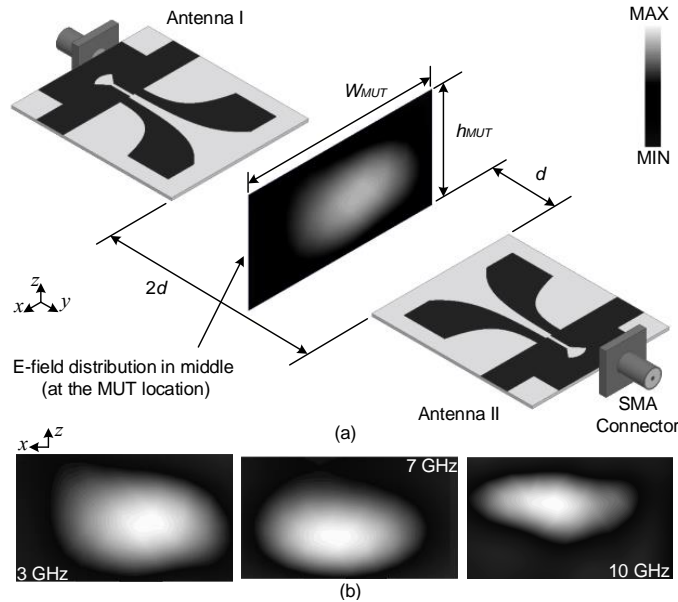


Figure 6.5: (a) The two near-field coupled antennas faced each other, and the E-field distribution is shown in middle and at the position of MUT at $f = 3$ GHz, and (b) the E-field distribution in a plane in between the two antennas where the MUT is located at different frequencies. The design values are: $W_{MUT} = h_{MUT} = 51$ mm, and $d = 30$ mm.

be optimized to improve the accuracy of the sensor, if the shape and dimensions of the container are custom designed. In order to better show the importance of the container shape, and dimensions, the E-field distribution is plotted in between the two antennas, and where the MUT is placed, and shown in Fig. 6.5 at different frequencies. As can be seen, the container requires to cover the area where the E-field distribution is concentrated. Otherwise, considerable amount of energy will be diffracted from the edges of the MUT and container, which reduces the accuracy of the sensor specially for MUTs with large dielectric constants, such as dmsO ($\epsilon' = 46.4$ at 3 GHz).

Fig. 6.6 shows the cuvette used in the proposed work. This cuvette is made of Quartz glass with a dielectric constant of 3.78 and a loss tangent of below 0.0004, which is roughly independent of the frequency over the desired UWB range. The width and height of the cuvette are chosen to cover the main concentration of the E-field distribution in the middle

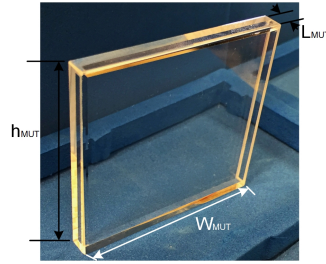


Figure 6.6: The cuvette used to place the liquid MUT in between the two antennas is made of Quartz glass with a volume of ~ 5 ml.

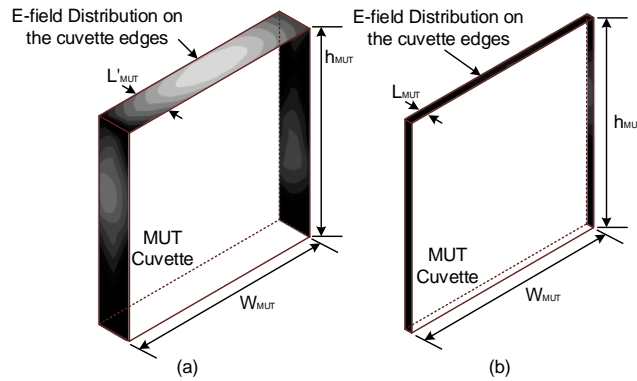


Figure 6.7: The E-field distribution on the edges of the MUT cuvette at 3 GHz, when (a) $L'_{MUT} = 8.5$ mm $> \lambda/10$ at 10 GHz, and (b) $L_{MUT} = 2$ mm $< \lambda/10$ at 10 GHz.

plane, as was shown in Fig. 6.5(b) at different frequencies. As a result, W_{MUT} , and h_{MUT} are both chosen 51 mm. On the other hand, the length of the cuvette, L_{MUT} , needs to be lower than $\lambda/10$ at the upper limit (10 GHz) in order to avoid multiple reflection, and electromagnetic bouncing inside the MUT. A lower length for the cuvette also reduces the required volume of the MUT. Moreover, an L_{MUT} , smaller than $\lambda/10$ at 10 GHz results in negligible diffraction from the edges of the MUT, while having a larger L_{MUT} can result in significant electromagnetic diffraction from the edges. This is better shown in Fig. 6.7, where the E-field distribution is plotted on the edges of the cuvette at 3 GHz for two different values of L_{MUT} . As can be seen, when the length is as large as 8.5 mm,

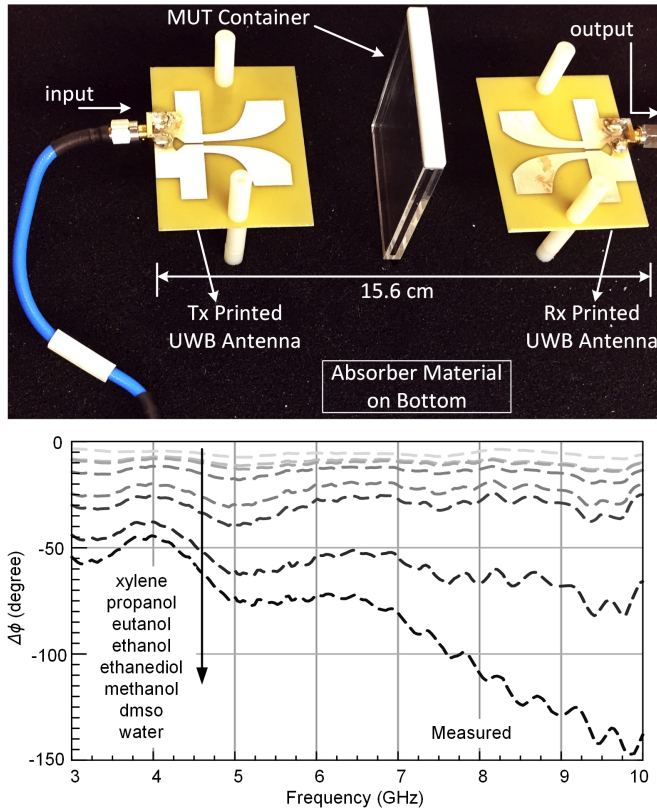


Figure 6.8: (a) The proposed contactless setup for liquid chemical sensing, and (b) simulated and measured unwrapped phase difference of the system for various liquid MUTs compared to air as the reference material.

which is $\sim 0.28\lambda$ at 10 GHz, there are E-field maximums on each edge of the cuvette, while reducing the length to 2 mm ($\sim 0.06\lambda$ at 10 GHz) would result in negligible E-field concentration on the edges. As a result, the length of the cuvette, L_{MUT} , is chosen to be $2 \text{ mm} < \lambda/10$ at 10 GHz, in order to (1) reduce the required volume of the sample liquid MUT, (2) avoid Electromagnetic bouncing and multiple reflection issues, and (3) significantly reduce the diffraction from the edges of the cuvette. In this case, the required volume is only $\sim 5 \text{ ml}$.

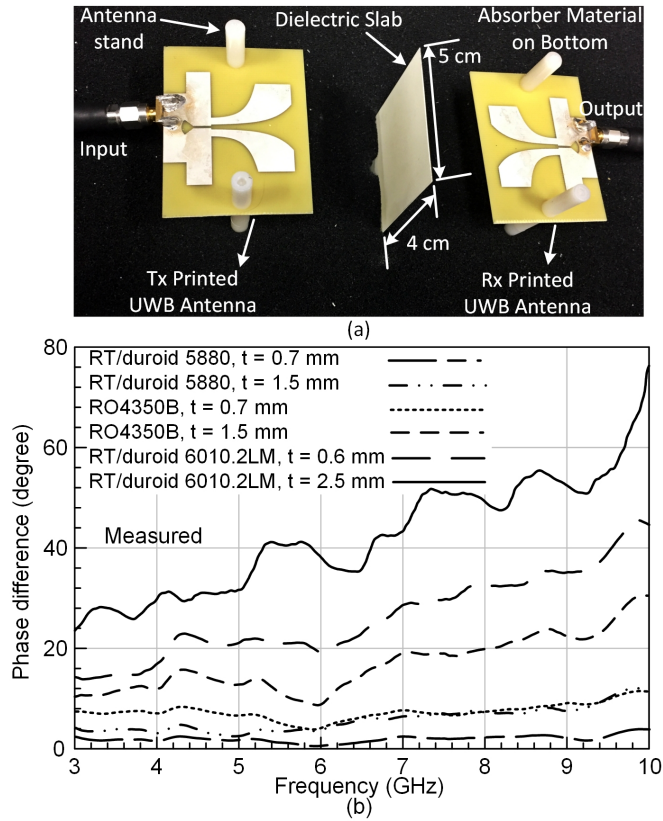


Figure 6.9: (a) The proposed contactless setup for thickness sensing of solid dielectric slabs , and (b) measured unwrapped phase difference of the system for solid dielectric materials with different thicknesses.

6.3 Implemented Setup and Experimental Results

Liquid and solid material sensing is carried out using the proposed sensor setup. Fig. 6.8 (a) shows the two fabricated antennas faced to each other with the liquid MUT in middle. The overall size of the setup is $15.6 \times 6.1 \text{ cm}^2$. The MUT container is a standard tube pipet, made of polypropylene, with a diameter of 17 mm. First, an empty pipet is placed between the two antennas, and the phase of S_{21} is measured as the reference condition using Agilent N5230A VNA. Afterwards, the container is filled with various MUTs, and the phase responses are measured for each material. The results are calibrated

by subtracting the phase responses of each MUT from the phase response of the system when the pipet is empty. Therefore, the additional effect of the container is removed from the results. Fig. 6.8 (b) shows the measured phase differences for xylene, propanol, butanol, ethanol, ethanediol, methanol, dmsol, and distilled water. As can be seen, the sensor is able to successfully differentiate among various liquid MUTs. Dielectric constant (ϵ') can be also extracted for an unknown liquid chemical using the behavioral fitting-curve approach discussed in section 5.4.2 [26]. Fig. 6.9 (a) shows the proposed setup for thickness sensing of thin dielectric slabs. The distance between the two antennas is the same as for liquid sensing, while the dielectric slab is placed in between. The area of the dielectric slab needs to be large enough ($\sim 4 \times 5 \text{ cm}^2$) to reduce the diffraction effect from the edges of the slab considering the E-field distribution shown in Fig. 6.5. Fig. 6.9 (b) shows the measured phase differences of the system for various Rogers dielectric materials with different thicknesses. As can be seen, the proposed sensor can be utilized for different applications, where solid or liquid sensing is required.

7. SUMMARY & CONCLUSIONS

7.1 Conclusions

Various miniaturization techniques are introduced in this thesis to achieve more compact passive components in different applications. Metamaterial-inspired miniaturization technique is applied to cavity-based SIW resonators, filters, and antennas in Sections II, and III. The idea is based on exciting the first negative-order resonance mode of the cavity using ramp-shaped interdigital capacitors, and then push that frequency to lower values by loading the cavity with a floating metal patch. The proposed method introduced a miniaturization factor of $\sim 90\%$ for the first time, to the best of author's knowledge.

Compact circular antenna arrays for mm-wave applications is discussed and implemented in Section IV. SIW cavity-based antennas are integrated with the radial SIW cavity-based power divider in a multi-layer 3D configuration to construct the axially symmetric antenna array. Due to utilizing high-Q cavity-based power divider, and antenna structures in a relatively compact fashion, a high radiation efficiency is achieved for 5G applications.

Moreover, a dielectric spectroscopy system is proposed in Section V, in which a metamaterial-inspired transmission line is utilized as the sensing element in a direct down-conversion interferometry architecture. Due to the use of the artificial transmission line, a compact contact-based sensor with improved sensitivity in a relatively wide bandwidth is achieved. A hybrid integration of passive components, active circuitry, and fluidic unit is also presented, and implemented.

Finally, a contact-less UWB sensor is proposed in chapter VI, which is based on having two printed Vivaldi antennas coupled in their radiative near-field region and locating the MUT in between. Due to the designed near-field sensor, the required volume of the sample is minimized, and a compact setup size is achieved. The experimental results proved

the promising application of the proposed near-field method in liquid or solid material characterization.

7.2 Future Works

The works presented in this dissertation were focused on two main categories; (1) miniaturization of SIW cavity-based resonators, filters, and antennas, and (2) developing compact contact-based and contact-less dielectric spectroscopy sensors and systems. In this section, the potential extension of the proposed miniaturization methods to other applications are briefly discussed.

7.2.1 Miniaturized SIW Cavity-based Passive Components

One advantage of the miniaturization method presented in chapter II, is its applicability to different SIW cavity resonator-based passive components. In chapter II, an ultra-miniature two-pole bandpass filter, and two trisection bandpass filters were designed, implemented and tested. Same resonators might be utilized to construct higher order filters. A higher-order of the poles and zeros in the bandpass response of the filter is required in many applications to achieve specific filtering characteristics such as the rolling off, bandwidth and insertion loss requirements. Moreover, the miniaturization method applied to SIW cavity-based resonators can be employed to construct bandstop filters. Such areas require more investigation on the physical coupling of the proposed various resonators in order to achieve a combination suitable for the required filtering specifications.

Moreover, since the ultra-miniature trisection filters, proposed in chapter II, have transmission zeros in different sides of the passband, a SIW cavity-based highly-compact diplexer component can be designed based on a combination of the two proposed trisection filters. High isolation, and rolling off between the two passbands, and the operational bandwidth are some primary parameters in such diplexer designs, which require more study on combining the two trisection filters together, and investigation on their effects on

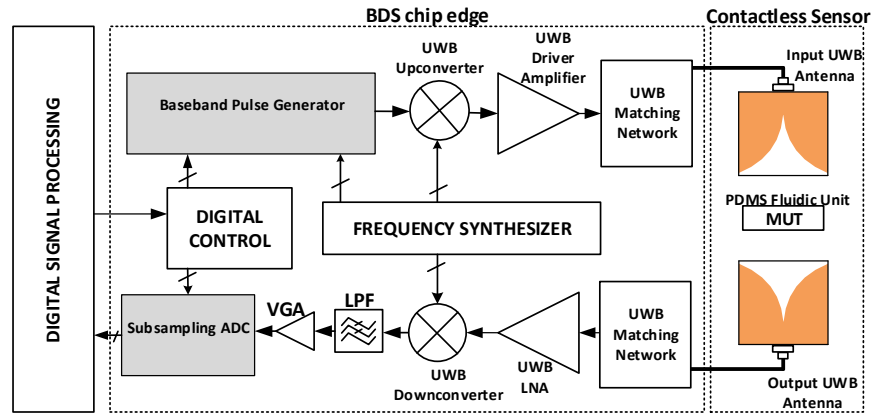


Figure 7.1: The conceptual system-level block diagram of the compact contact-less BDS system.

each other's performance.

7.2.2 Contact-less Dielectric Spectroscopy Systems

A compact contact-less sensor is introduced in chapter VI, where its performance is tested based on measuring the phase and amplitude variations of the transmission coefficient for different materials. While, the sensing section is miniaturized based on proposing near-field material characterization, the measurement setup still is bulky since a VNA is required to measure the transmission coefficient. However, the proposed UWB contact-less sensor can be ultimately used in a hybrid self-sustained UWB broadband dielectric spectroscopy (BDS) system as conceptually shown in Fig. 7.1. The system includes a BDS chip, the proposed contact-less sensor, and a digital signal processing (DSP) unit. The fully-integrated BDS chip includes the UWB transmitter (baseband pulse generator, up-converter, driver amplifier, and matching network), UWB receiver (matching network, LNA, down-converter and sub-sampling ADC), frequency synthesizer and the control unit/pulse shaper. All the CMOS blocks have to have very small variations in their group delays to prevent any phase distortion, and therefore, accurate material characterization

can be achieved with the VNA removed from the setup. Such a complete compact and self-sustained dielectric spectroscopy system requires extensive effort and research for different parts such as, system budget analysis, block-level CMOS design, hybrid integration of different units with passive, and active parts, etc.

REFERENCES

- [1] D. Pozar, *Microwave Engineering, 4th Edition*. Wiley Global Education, 2011.
- [2] C. A. Balanis, *Antenna Theory: Analysis and Design*. John Wiley Sons, second ed., 1997.
- [3] J. Hirokawa and M. Ando, "Single-layer feed waveguide consisting of posts for plane wave excitation in parallel plates," *IEEE Transactions on Antennas and Propagation*, vol. 46, pp. 625–630, May 1998.
- [4] H. Uchimura, T. Takenoshita, and M. Fujii, "Development of a "laminated waveguide"," *IEEE Transactions on Microwave Theory and Techniques*, vol. 46, pp. 2438–2443, Dec 1998.
- [5] D. Deslandes and K. Wu, "Single-substrate integration technique of planar circuits and waveguide filters," *IEEE Transactions on Microwave Theory and Techniques*, vol. 51, pp. 593–596, Feb 2003.
- [6] X. P. Chen and K. Wu, "Substrate integrated waveguide filters: Design techniques and structure innovations," *IEEE Microwave Magazine*, vol. 15, pp. 121–133, Sept 2014.
- [7] K. Entesari, A. P. Saghati, V. Sekar, and M. Armendariz, "Tunable SIW structures: Antennas, vcos, and filters," *IEEE Microwave Magazine*, vol. 16, pp. 34–54, June 2015.
- [8] Y. L. Zhang, W. Hong, K. Wu, J. X. Chen, and H. J. Tang, "Novel substrate integrated waveguide cavity filter with defected ground structure," *IEEE Transactions on Microwave Theory and Techniques*, vol. 53, pp. 1280–1287, Apr. 2005.

- [9] Y. Dong and T. Itoh, "Promising future of metamaterials," *IEEE Microwave Magazine*, vol. 13, pp. 39–56, March 2012.
- [10] V. Sekar and K. Entesari, "A novel compact dual-band half-mode substrate integrated waveguide bandpass filter," in *IEEE MTT-S International Microwave Symposium Digest*, pp. 1–4, Jun. 2011.
- [11] A. Pourghorban Saghati, A. Pourghorban Saghati, and K. Entesari, "An ultra-miniature quarter-mode SIW bandpass filter operating at first negative order resonance," in *IEEE MTT-S International Microwave Symposium Digest*, pp. 1–3, May. 2015.
- [12] A. Pourghorban Saghati, A. Pourghorban Saghati, and K. Entesari, "Ultra-miniature SIW cavity resonators and filters," *IEEE Transactions on Microwave Theory and Techniques*, vol. 63, pp. 4329–4340, Dec 2015.
- [13] A. P. Saghati, A. P. Saghati, and K. Entesari, "An ultra-miniature SIW cavity-backed slot antenna," *IEEE Antennas and Wireless Propagation Letters*, vol. 16, pp. 313–316, 2017.
- [14] J. Zhang, X. Ge, Q. Li, M. Guizani, and Y. Zhang, "5G millimeter-wave antenna array: Design and challenges," *IEEE Wireless Communications*, October 2016.
- [15] S. J. Park, D. H. Shin, and S. O. Park, "Low side-lobe substrate-integrated-waveguide antenna array using broadband unequal feeding network for millimeter-wave handset device," *IEEE Transactions on Antennas and Propagation*, vol. 64, pp. 923–932, March 2016.
- [16] P. Ioannides and C. A. Balanis, "Uniform circular and rectangular arrays for adaptive beamforming applications," *IEEE Antennas and Propagation Letters*, vol. 4, pp. 351–354, 2005.

- [17] A. S. Friedrich Kremer, *Broadband Dielectric Spectroscopy*. Springer-Verlag Berlin Heidelberg, 2003.
- [18] K. Entesari, A. A. Helmy, and M. Moslehi-Bajestan, “Integrated systems for biomedical applications: Silicon-based rfmicrowave dielectric spectroscopy and sensing,” *IEEE Microwave Magazine*, vol. 18, pp. 57–72, July 2017.
- [19] M. M. Bajestan, A. A. Helmy, H. Hedayati, and K. Entesari, “A 0.62–10 GHz complex dielectric spectroscopy system in 0.18 μ m cmos,” *IEEE Transactions on Microwave Theory and Techniques*, vol. 62, pp. 3522–3537, Dec 2014.
- [20] D. Misra, M. Chhabra, B. R. Epstein, M. Microtznik, and K. R. Foster, “Noninvasive electrical characterization of materials at microwave frequencies using an open-ended coaxial line: test of an improved calibration technique,” *IEEE Transactions on Microwave Theory and Techniques*, vol. 38, pp. 8–14, Jan 1990.
- [21] D. K. Ghodgaonkar, V. V. Varadan, and V. K. Varadan, “A free-space method for measurement of dielectric constants and loss tangents at microwave frequencies,” *IEEE Transactions on Instrumentation and Measurement*, vol. 38, pp. 789–793, Jun 1989.
- [22] D. K. Ghodgaonkar, V. V. Varadan, and V. K. Varadan, “Free-space measurement of complex permittivity and complex permeability of magnetic materials at microwave frequencies,” *IEEE Transactions on Instrumentation and Measurement*, vol. 39, pp. 387–394, Apr 1990.
- [23] Y. Yang, H. Zhang, J. Zhu, G. Wang, T.-R. Tzeng, X. Xuan, K. Huang, and P. Wang, “Distinguishing the viability of a single yeast cell with an ultra-sensitive radio frequency sensor,” *Lab Chip*, vol. 10, pp. 553–555, 2010.

- [24] O. H. Karabey, F. Goelden, A. Gaebler, and R. Jakoby, "Precise broadband microwave material characterization of liquids," in *European Microwave Conference (EuMC)*, pp. 1591–1594, Sept 2010.
- [25] A. Pourghorban Saghati, J. Singh Batra, J. Kameoka, and K. Entesari, "A metamaterial-inspired miniaturized wide-band microwave interferometry sensor for liquid chemical detection," in *IEEE MTT-S International Microwave Symposium Digest*, pp. 1–3, May. 2016.
- [26] A. P. Saghati, J. S. Batra, J. Kameoka, and K. Entesari, "A metamaterial-inspired wideband microwave interferometry sensor for dielectric spectroscopy of liquid chemicals," *IEEE Transactions on Microwave Theory and Techniques*, vol. 65, pp. 2558–2571, July 2017.
- [27] I. Vakili, L. Ohlsson, L. E. Wernersson, and M. Gustafsson, "Time-domain system for millimeter-wave material characterization," *IEEE Transactions on Microwave Theory and Techniques*, vol. 63, pp. 2915–2922, Sept 2015.
- [28] Z. Akhter and M. J. Akhtar, "Free-space time domain position insensitive technique for simultaneous measurement of complex permittivity and thickness of lossy dielectric samples," *IEEE Transactions on Instrumentation and Measurement*, vol. 65, pp. 2394–2405, Oct 2016.
- [29] A. P. Saghati and K. Entesari, "A uwb near-field contactless sensor for solid and liquid material characterization," in *2017 IEEE International Symposium on Antennas and Propagation (APSURSI)*, pp. 1–3, June 2017.
- [30] K. Entesari, A. Pourghorban Saghati, V. Sekar, and M. Armendariz, "Tunable SIW structures: Antennas, vcos, and filters," *IEEE Microwave Magazine*, vol. 16, pp. 34–54, Jun. 2015.

- [31] J. Martinez, S. Sirci, M. Taroncher, and V. Boria, "Compact CPW-fed combline filter in substrate integrated waveguide technology," *IEEE Microwave Wireless Components Letters*, vol. 22, pp. 7–9, Jan. 2012.
- [32] Y. D. Dong, T. Yang, and T. Itoh, "Substrate integrated waveguide loaded by complementary split-ring resonators and its applications to miniaturized waveguide filters," *IEEE Transactions on Microwave Theory and Techniques*, vol. 57, pp. 2211–2223, Sep. 2009.
- [33] Y. Dong and T. Itoh, "Substrate integrated waveguide negative order resonances and their applications," *IET Microwave, Antennas, and Propagation*, vol. 4, pp. 1081–1091, Aug. 2010.
- [34] Z. Zhang, N. Yang, and K. Wu, "5-GHz bandpass filter demonstration using quarter-mode substrate integrated waveguide cavity for wireless systems," in *Proc. IEEE Radio Wireless Symposium*, pp. 95–98, Jan. 2009.
- [35] C. Jin and Z. Shen, "Compact triple-mode filter based on quarter-mode substrate integrated waveguide," *IEEE Transactions on Microwave Theory and Techniques*, vol. 62, pp. 37–45, Jan. 2014.
- [36] A. Pourghorban Saghati, M. Mirsalehi, and M. Neshati, "A HMSIW circularly polarized leaky-wave antenna with backward, broadside, and forward radiation," *IEEE Antennas and Wireless Propagation Letters*, vol. 13, pp. 451–454, 2014.
- [37] L. Szydowski, A. Jedrzejewski, and M. Mrozowski, "A trisection filter design with negative slope of frequency-dependent crosscoupling implemented in substrate integrated waveguide (SIW)," *IEEE Microwave and Wireless Components Letters*, vol. 23, pp. 456–458, Sep. 2013.

- [38] J. Martinez, S. Sirci, and V. Boria, "Compact SIW filter with asymmetric frequency response for c-band wireless applications," in *Proceeding International Wireless Symposium*, pp. 1–4, Apr. 2013.
- [39] P.-J. Zhang and M.-Q. Li, "Cascaded trisection substrate-integrated waveguide filter with high selectivity," *Electronics Letter*, vol. 50, no. 23, pp. 1717–1719, 2014.
- [40] S. Sirci, J. Martinez, J. Vague, and V. Boria, "Substrate integrated waveguide diplexer based on circular triplet combline filters," *Microwave and IEEE Wireless Components Letters*, vol. 25, pp. 430–432, July 2015.
- [41] E. Arnieri and G. Amendola, "Analysis of substrate integrated waveguide structures based on the parallel-plate waveguide green's function," *IEEE Transactions on Microwave Theory and Techniques*, vol. 56, pp. 1615–1623, Jul. 2008.
- [42] J. Hobdell, "Optimization of interdigital capacitors," *IEEE Transactions on Microwave Theory and Techniques*, vol. 27, pp. 788–791, Sep. 1979.
- [43] A. Saghati and K. Entesari, "A reconfigurable SIW cavity-backed slot antenna with one octave tuning range," *IEEE Transactions on Antennas and Propagation*, vol. 61, pp. 3937–3945, Aug. 2013.
- [44] H. J. Tang, W. Hong, J.-X. Chen, G. Q. Luo, and K. Wu, "Development of millimeter-wave planar diplexers based on complementary characters of dual-mode substrate integrated waveguide filters with circular and elliptic cavities," *IEEE Transactions on Microwave Theory and Techniques*, vol. 55, pp. 776–782, Apr. 2007.
- [45] J.-S. G. Hong and M. J. Lancaster, *Microstrip Filters for RF/Microwave Applications*. John Wiley & Sons, 2004.
- [46] C.-C. Yang and C.-Y. Chang, "Microstrip cascade trisection filter," *IEEE Microwave Guided-Wave Letters*, vol. 9, pp. 271–273, Jul. 1999.

- [47] X.-P. Chen and K. Wu, "Substrate integrated waveguide cross-coupled filter with negative coupling structure," *IEEE Transactions on Microwave Theory and Techniques*, vol. 56, pp. 142–149, Jan. 2008.
- [48] W. Hong, N. Behdad, and K. Sarabandi, "Size reduction of cavity-backed slot antennas," *IEEE Transactions on Antennas and Propagation*, vol. 54, pp. 1461–1466, May 2006.
- [49] G. Q. Luo, Z. F. Hu, L. X. Dong, and L. L. Sun, "Planar slot antenna backed by substrate integrated waveguide cavity," *IEEE Antennas and Wireless Propagation Letters*, vol. 7, pp. 236–239, 2008.
- [50] J. Bohorquez, H. Pedraza, I. Pinzon, J. Castiblanco, N. Pena, and H. Guarnizo, "Planar substrate integrated waveguide cavity-backed antenna," *IEEE Antennas and Wireless Propagation Letters*, vol. 8, pp. 1139–1142, 2009.
- [51] Y. Dong and T. Itoh, "Miniaturized substrate integrated waveguide slot antennas based on negative order resonance," *IEEE Transactions on Antennas and Propagation*, vol. 58, pp. 3856–3864, Dec 2010.
- [52] S. Onoe, "Evolution of 5G mobile technology toward 2020 and beyond," *IEEE International Solid-State Circuits Conference (ISSCC)*, 2016.
- [53] F. Aryanfar, J. Pi, H. Zhou, T. Henige, G. Xu, S. Abu-Surra, D. Psychoudakis, and F. Khan, "Millimeter-wave base station for mobile broadband communication," *IEEE MTT-S International Microwave Symposium*, 2015.
- [54] S. Shakib, H. C. Park, J. Dunworth, V. Aparin, and K. Entesari, "A highly efficient and linear power amplifier for 28-ghz 5g phased array radios in 28-nm cmos," *IEEE Journal of Solid-State Circuits*, vol. 51, no. 12, pp. 3020–3036, 2016.

- [55] H. Zhou and F. Aryanfar, "Millimeter-wave open ended SIW antenna with wide beam coverage," *IEEE International Symposium on Antennas and Propagation USNC/URSI National Radio Science Meeting*, 2013.
- [56] A. T. Alreshaid, O. Hammi, M. S. Sharawi, and K. Sarabandi, "A millimeter wave switched beam planar antenna array," *IEEE International Symposium on Antennas and Propagation USNC/URSI National Radio Science Meeting*, July 2015.
- [57] M. Khalily, R. Tafazolli, T. A. Rahman, and M. R. Kamarudin, "Design of phased arrays of series-fed patch antennas with reduced number of the controllers for 28-GHz mm-wave applications," *IEEE Antennas and Wireless Propagation Letters*, vol. 15, pp. 1305–1308, 2016.
- [58] D. I. L. de Villiers, P. W. van der Walt, and P. Meyer, "Design of a ten-way conical transmission line power combiner," *IEEE Transactions on Microwave Theory and Techniques*, vol. 55, pp. 302–308, Feb 2007.
- [59] K. Song, Y. Fan, and Y. Zhang, "Eight-way substrate integrated waveguide power divider with low insertion loss," *IEEE Transactions on Microwave Theory and Techniques*, vol. 56, pp. 1473–1477, June 2008.
- [60] O. M. Haraz, A. Elboushi, S. A. Alshebeili, and A. R. Sebak, "Dense dielectric patch array antenna with improved radiation characteristics using ebg ground structure and dielectric superstrate for future 5G cellular networks," *IEEE Access*, vol. 2, pp. 909–913, 2014.
- [61] E. N. Ivanov, M. E. Tobar, and R. A. Woode, "Microwave interferometry: application to precision measurements and noise reduction techniques," *IEEE Transactions on Ultrasonics, Ferroelectrics, and Frequency Control*, vol. 45, pp. 1526–1536, Nov 1998.

- [62] S. Kim and C. Nguyen, "A displacement measurement technique using millimeter-wave interferometry," *IEEE Transactions on Microwave Theory and Techniques*, vol. 51, pp. 1724–1728, June 2003.
- [63] M. Schueler, C. Mandel, M. Puentes, and R. Jakoby, "Metamaterial inspired microwave sensors," *IEEE Microwave Magazine*, vol. 13, pp. 57–68, March 2012.
- [64] M. T. Jilani, M. Z. ur Rehman, A. M. Khan, M. T. Khan, and S. M. Ali, "A brief review of measuring techniques for characterization of dielectric materials," *International Journal of information and electrical engineering*, vol. 1, no. 1, pp. 1–5, 2013.
- [65] G. Gauglitz, A. Brecht, G. Kraus, and W. Mahm, "Chemical and biochemical sensors based on interferometry at thin (multi-) layers," *Sensors and Actuators B: Chemical*, vol. 11, no. 1, pp. 21 – 27, 1993.
- [66] B. Reinhard, K. M. Schmitt, V. Wollrab, J. Neu, R. Beigang, and M. Rahm, "Metamaterial near-field sensor for deep-subwavelength thickness measurements and sensitive refractometry in the terahertz frequency range," *Applied Physics Letters*, vol. 100, no. 22, 2012.
- [67] J. Sztipanovits and G. Karsai, "Knowledge-based techniques in instrumentation," *IEEE Engineering in Medicine and Biology Magazine*, vol. 7, pp. 13–17, June 1988.
- [68] Y. K. Jones, Z. Li, M. M. Johnson, F. Josse, and J. M. Hossenlopp, "Atr-ftir spectroscopic analysis of sorption of aqueous analytes into polymer coatings used with guided sh-saw sensors," *IEEE Sensors Journal*, vol. 5, pp. 1175–1184, Dec 2005.
- [69] Y. Feldman, I. Ermolina, and Y. Hayashi, "Time domain dielectric spectroscopy study of biological systems," *IEEE Transactions on Dielectrics and Electrical Insulation*, vol. 10, pp. 728–753, Oct 2003.

- [70] R. Zoughi, *Microwave Non-Destructive Testing and Evaluation Principles*. Springer Netherlands, 2000.
- [71] C. Nguyen and S. Kim, *Theory, analysis, and design of RF interferometric sensors*. Springer New York, 2012.
- [72] A. A. Helmy, S. Kabiri, M. M. Bajestan, and K. Entesari, “Complex permittivity detection of organic chemicals and mixtures using a 0.5–3-ghz miniaturized spectroscopy system,” *IEEE Transactions on Microwave Theory and Techniques*, vol. 61, pp. 4646–4659, Dec 2013.
- [73] Agilent, *Basics of Measuring the Dielectric Properties of Materials*, pp. 1–32. Agilent Technologies, Inc., 2005.
- [74] G. A. Ferrier, S. F. Romanuik, D. J. Thomson, G. E. Bridges, and M. R. Freeman, “A microwave interferometric system for simultaneous actuation and detection of single biological cells,” *Lab Chip*, vol. 9, pp. 3406–3412, 2009.
- [75] Y. Cui and P. Wang, “The design and operation of ultra-sensitive and tunable radio-frequency interferometers,” *IEEE Transactions on Microwave Theory and Techniques*, vol. 62, pp. 3172–3182, Dec 2014.
- [76] N. T. Cherpak, A. A. Barannik, Y. V. Prokopenko, T. A. Smirnova, and Y. F. Filipov, *A New Technique of Dielectric Characterization of Liquids*. Springer Netherlands, 2005.
- [77] P. A. Bernard and J. M. Gautray, “Measurement of dielectric constant using a microstrip ring resonator,” *IEEE Transactions on Microwave Theory and Techniques*, vol. 39, pp. 592–595, Mar 1991.
- [78] A. Cataldo, E. D. Benedetto, and G. Cannazza, *Quantitative and Qualitative Characterization of Liquid Materials*, pp. 51–83. Berlin, Heidelberg: Springer Berlin

Heidelberg, 2011.

- [79] C. Damm, M. Schussler, M. Puentes, H. Maune, M. Maasch, and R. Jakoby, “Artificial transmission lines for high sensitive microwave sensors,” in *IEEE Sensors*, pp. 755–758, Oct 2009.
- [80] V. K. Ivanov, A. Silin, and O. M. Stadnyk, “Measurement of complex permittivity of liquids using open-ended coaxial-line and metamaterial substrate,” *Telecommunications and Radio Engineering*, vol. 71, no. 12, pp. 1125–1140, 2012.
- [81] J. R. Macdonald, “Impedance spectroscopy,” *Annals of Biomedical Engineering*, vol. 20, no. 3, pp. 289–305, 1992.
- [82] C.-L. Yang, “Non-contact measurement of permittivity and thickness using planar resonators,” in *2015 IEEE MTT-S International Microwave Symposium*, pp. 1–3, May 2015.
- [83] A. P. Gregory and R. N. Clarke, “Tables of the complex permittivity of dielectric reference liquids at frequencies up to 5 ghz,” *NPL Report MAT 23*, 2012.
- [84] A. A. M. F. Buckley, “Tables of dielectric dispersion data for pure liquids and dilute solutions,” *U.S. Dept. of Commerce, National Bureau of Standards*, 1958.
- [85] J. Baena, J. Bonache, F. Martin, R. Sillero, F. Falcone, T. Lopetegi, M. Laso, J. Garcia-Garcia, I. Gil, M. Portillo, and M. Sorolla, “Equivalent-circuit models for split-ring resonators and complementary split-ring resonators coupled to planar transmission lines,” *IEEE Transactions on Microwave Theory and Techniques*, vol. 53, pp. 1451–1461, April 2005.
- [86] A. Pourghorban Saghati, J. Batra, J. Kameoka, and K. Entesari, “A miniaturized microfluidically reconfigurable coplanar waveguide bandpass filter with maximum

- power handling of 10 watts,” *IEEE Transactions on Microwave Theory and Techniques*, vol. 63, pp. 2515–2525, Aug 2015.
- [87] K. Entesari and A. P. Saghati, “Fluidics in microwave components,” *IEEE Microwave Magazine*, vol. 17, pp. 50–75, June 2016.
- [88] A. Sihvola, “Mixing rules with complex dielectric coefficients,” *Subsurface Sensing Technologies and Applications*, vol. 1, no. 4, pp. 393–415, 2000.
- [89] J. Han and C. Nguyen, “Development of a tunable multiband uwb radar sensor and its applications to subsurface sensing,” *IEEE Sensors Journal*, vol. 7, pp. 51–58, Jan 2007.
- [90] M. Zhao, J. D. Shea, S. C. Hagness, and D. W. van der Weide, “Calibrated free-space microwave measurements with an ultrawideband reflectometer-antenna system,” *IEEE Microwave and Wireless Components Letters*, vol. 16, pp. 675–677, Dec 2006.
- [91] J. Wu, Z. Zhao, Z. Nie, and Q. H. Liu, “A printed UWB vivaldi antenna using stepped connection structure between slotline and tapered patches,” *IEEE Antennas and Wireless Propagation Letters*, vol. 13, pp. 698–701, 2014.